Structure and Dynamics of Conducting Poly(aniline) based Compounds

Maciej Sniechowski

AGH University of Science and Technology

Faculty of Physics and
Applied Computer Science

UNIVERSITE JOSEPH FOURIER
SCIENCES. TECHNOLOGIE. MEDECINE. GRENOBLE - ALPES

spectro
Laboratoire de Spectrométrie Physique

Thesis by

Maciej Śniechowski

In partial fulfillment of the requirements
for the degree of
Philosophy Doctor in Physics

Structure and dynamics of conducting polyaniline based compounds

Thesis supervisors:

Prof. Wojciech Łużny

Prof. David Djurado

2005

Acknowledgements

First of all, I would like to thank my supervisors; David Djurado, and Wojciech Łużny for their support and guidance.

Adam Proń, Patrice Rannou, Krzysztof Bieńkowski for their help in understanding of polymers chemistry

Mark Johnson, Miguel Gonzales, Mark Bée, Marie Plazanet gave me much valuable help when I first joined "Computing Laboratory" at ILL and computer simulation was a new game for me.

Teresa and Jean-Claude Charbonnel, Alicja Corre and all the people who made my stay in Grenoble truly enjoyable.

Finally I would like to thank members of my family for their support of so many years, and especially my Dear Madzia for her companion and patience.

Preface

More than twenty years of research and development on conducting polymers have made these organic systems good candidates for being used in many technological applications as organic field effect transistors, luminescent diodes, solar cells and synthetic metals [1]. In this context, it is crucial to understand in depth the processes involved in electronic transport either for the highly doped conducting state or for the undoped semi-conducting state of these systems. Generally speaking, all the models found in the literature for tentatively explaining the electronic transport in π conjugated polymers evoke the creation of excited electronic states (solitons, polarons and bipolarons mainly), the existence and diffusivity of which are intimately linked to the lattice [2][3][4]. Accordingly, the degree of disorder (static and dynamic) encountered in the corresponding macromolecular lattice is believed to strongly affect these properties. Thus, in recent years, molecular structure and dynamics in so called plast-doped poly(aniline) systems have been studied in order to gain insight into the correlations between static / dynamic disorder and electrical properties. These studies have definitively revealed the systematic correspondence between dynamical and electrical transitions, establishing the particularity for these systems in a given temperature range to couple some lattice flexibility with a metal-like electrical conductivity [5][6]. A further theoretical explanation of the electrical properties of polyaniline requires systematic studies of structure and dynamics, which is the subject of this thesis.

The objectives

The main goals of this thesis were:

- systematic X-ray diffraction and small angle scattering studies and computer modeling of supra-molecular structure attended to statistical disorder in the system
- Quasi elastic studies (QENS) of dynamic properties of the system
- Simulations of the molecular dynamics (MD), computation of neutron scattering functions, comparison with experimental results, and proposed analytical models.

List of contents

A. Introduction

A.1 Generalities on conducting polymers

Scientific and technological interests of electronic conducting polymers are no more to be demonstrated. The importance of this field of research has been clearly recognized by the attribution of the chemistry Nobel Prize in 2000 to professors A.J. Heeger, A.G. MacDiarmid and H. Shirakawa [7]. The ability of conjugated polymers to carry delocalized electronic charges is used in many applications in which metallic, semi-conducting or electrically tunable medium is involved [8]. From here, it is easy to imagine that we are dealing with a field in which the scientific interdisciplinarity is privileged especially in between chemists and physicists but also more recently with electronics and optics engineering and biologists. Conducting polymers offer a unique combination of properties that make them attractive alternatives for conventional materials currently used in electronic devices like transistors, light emitting diodes (LED), photovoltaic cells, biochemical sensors, gas and liquid separation membranes, corrosion protection of metals, electrostatic discharge protection, electromagnetic interference shielding, and many others potential applications. The conductivity of these polymers can be tuned by chemical manipulation of the polymer backbone, by the nature of the dopant, by degree of doping, and blending with conventional polymers. In addition they offer light weight, processibility, and flexibility. Recent developments in materials sciences and molecular engineering give an excellent possibility for coupling unique electronic properties of conducting polymers with good mechanical properties, stability and low production costs commonly attributed to conventional polymers.

A.2 Structural study of conducting polymers

Due to the complexity of polymeric structures in general, for the complete description of the system it is necessary to study it at several length scales i.e: the chain configuration, the chain conformation, the supra-molecular structure and the morphology. In this chapter mainly the studies of the supra-molecular level which extends to several hundreds of Angstroms are reviewed. The supra-molecular structure of polymers is strongly determined by the shape and the intrachain structure (configuration and conformation) of the molecules. High symmetry 3D periodic packing is very rare due to the extreme shape anisotropy of macromolecules. The dimension of polymer macromolecules is much bigger along chain direction than in the two others. This anisotropy and the chain flexibility favor entropic factors that may prevent the most energetically favorable structure from ever being stabilized. The packing with parallel orientation of linear polymeric chains into a crystal lattice usually leads to low symmetry mono- or tri-clinic periodic unit cell, where each polymer chain belongs to several unit cells. The possibility of regular packing of linear chains into the crystal lattice may be easily affected by irregularity in primary chemical configuration of monomers in polymer chains. The polymers with side groups may also crystallize but the imperfection in side group arrangement deflect strongly this process. The other important features that prevent the crystallization are the topological defects as branching and cross-linking that contribute to decrease the global mobility of polymer chains. The stiffness of the polymer chains plays also a crucial role for determining its crystalline structure. The aspects described above determine that polymers in majority are only partially crystalline with the crystallinity varying in a wide range. The crystallites are small with typical coherence lengths between tenths and hundreds of Angstroms. A realistic description of supra-molecular structure requires a model which takes into account both crystalline and amorphous components. There are two main models of supra-molecular structure that are traditionally assumed: “fibrillar” or “lamellar” Fig(A.2.1). In the “fibrillar” model we assume that each polymer chain may enter and exit (belongs to) several ordered regions forming crystallites with other chains and away of crystallites the other parts of the same chain belongs to disordered amorphous parts. This model is often valid for the polymers with rigid chains containing double bonds and aromatic rings. The lamellar model dedicated for polymers with flexible linear chains assume formation of layered structures consisting of many times folded chains separated by amorphous regions. In practice the edges between ordered and amorphous regions are not always clearly sharply delimited.

The partially ordered meso-phase which extends in range where ordered phase change smoothly into disordered may be defined [9].

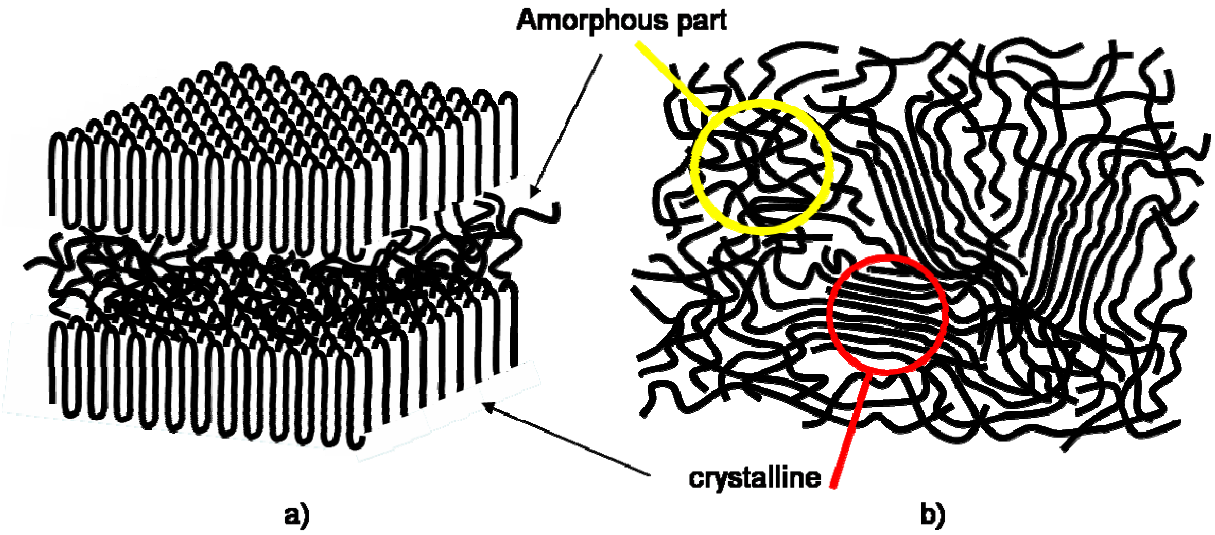

Fig. A.2.1 Schematic view of a) lamellar structure b) fibrillar structure.

Conducting polymers

Conducting polymers have some similarities to conventional polymers, but the extensive main-chain π-conjugation, which radically increases the chain stiffness, strongly determines its physical properties [10]. They are usually insoluble and difficult to processing. As a consequence conducting polymers form less ordered structures with many defects and distortion. It is convenient to describe the conducting polymers by considering several groups exhibiting different structural characteristics which depend on the internal chain architecture [11]. The first basic group consists of linear unsubstituted conducting polymers with a stiff (rigid-rod) chains like poly(acetylene) or poly(thiophene) or semiflexible (rods) chains like polyaniline [12]. The investigations carried out to develop new materials with better properties for new applications result in next group with a range of structural form. This group of compounds called hairy-rod is based on flexible side group substitution to the conducting polymer backbone [13].

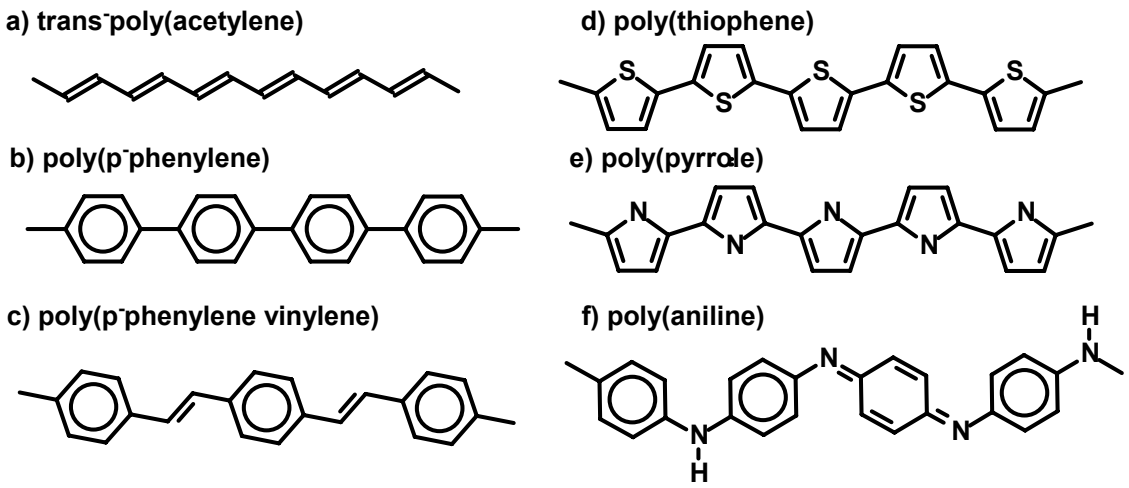

Fig. A.2.2 The family of linear rod-like conducting polymers.

Linear unsubstituted chains

Rigid-rod polymers

(non doped forms)

Rigid-rod polymers were the first conducting polymers synthesized. They have been deeply studied since poly(acetylene) unique electrical properties were discovered almost 30 years ago by MacDiarmid et al. The structural properties of these systems seem to be relatively well understood. Specific examples of these polymers are shown in Fig(A.2.2) and include poly(acetylene) PA, poly(p-phenylenevinylene) PPV, poly(phenylene) PPP, poly(thiophene) PT and poly(pyrrole) PPy. Typically these compounds exhibit crystalline phase within orthorhombic or monoclinic unit cell, common to many conventional linear polymers such as polyethylene or poly propylene, with characteristic herringbone packing shown on Fig(A.2.3) . The unit cell with p2gg symmetry consist of two chains which average orientation in respect to equatorial lattice vector a is set by angle φ. In nonequatorial chain direction fluctuations in axial chain to chain ordering are often present. This type of distortion leads to the paracrystallinity (broadening) or even disappearing of 001 reflections in c chain direction. The crystallinity for some rigid-rod conducting polymers may exceed up to 80%, but typically is much lower. The typical values of coherence lengths range from 50 to 200Å depending on specificities of the sample like particular synthesis details and additional processing procedures [14]. In many cases, sample processing lead to partial orientation of crystallites.

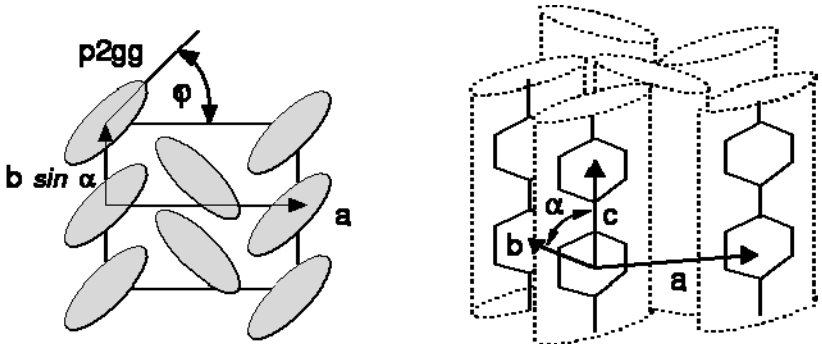

Fig.A.2.3 Characteristic herringbone crystal packing in polyphenylene. Typical equatorial packing for non-doped conducting polymers with linear rod-like rigid chains.

Poly(acetylene) PA and poly(phenylene) PPP

Experimental studies of *trans*-poly(acetylene) are consistent with 2D *p2gg* equatorial packing of the PA chains [15]. Three different space groups, $P2_1/a$ [16], $P2_1/n$ [17], Pnam [18][19] have been proposed with respect to 3D unit cell. The $P2_1/a$ structure has two chains in an in-phase relationship, while the $P2_1/n$ space group leads to out of phase arrangement. Some experiments suggest the alternatives of the structure being partially in phase, partially out of phase or having a random phase relation of bond alternation. This may be an explanation of absence of 001 peak in diffraction patterns. The concept of average structure is expressed in Pnam symmetry based unit cell.

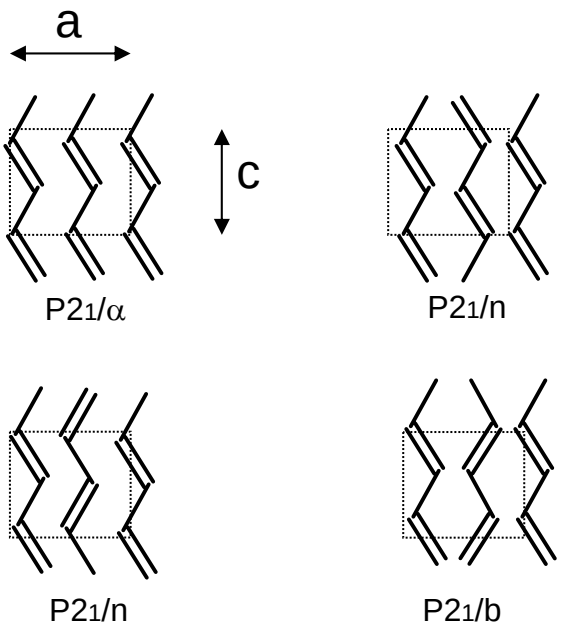

Fig. A.2.4 The influence of polyacetylene chains lateral shift on the space group of the crystallographic lattice.

Poly(p-phenylenevinylene) PPV, poly(thiophene) PT and poly(pyrrole) PPy

2D space group of the unit cell in equatorial direction of PPV can also be determined as p2gg with two chains traversing the cell. 3D monoclinic unit cell typically exhibits large lattice angle α=123°. Such a large monoclinic angle results from the shift of neighboring chains in the (b,c) plane, by which they reduce lateral phenyl-phenyl interaction and achieve close packing [20].

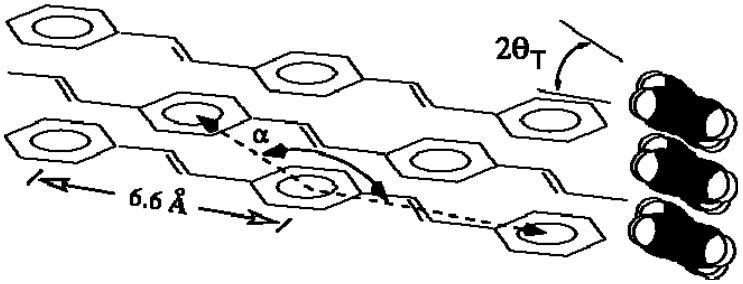

Fig. A.2.5 Structural organization of undoped PPV viewed in the (b,c) plane.

Semi-flexible rods: Polyaniline

The family of semi-flexible rod like conducting polymers includes some derivatives of poly(p-phenylene) and polyaniline PANI in its semi-oxidized emeraldine base EB form. Polyaniline chains are slightly more flexible compared to rigid-rod like polymers what is related to the contents of amine and imine nitrogen linkages within the main chain. The nitrogen sites also induce large phenyl ring torsional displacement, so the polyaniline exhibits bigger deviation from planarity than other π-conjugated chains. The polyaniline structural behavior is strongly determined by these effects. The most detailed structural studies of polyaniline report that structural parameters are very sensitive to the processing chemical treatment after synthesis [21]. Two classes of emeraldine base form of polyaniline named EB-1 and EB-2 have been presented. Emeraldine samples belonging to EB-2 class are prepared originally in the un-doped insulating form. The most common crystalline form EB-2 has an average structure best described within the orthorhombic *Pbcn* space group as shown on fig(A.2.6). The EB-2 class ranges from amorphous up to 50% crystalline [22]. The coherence lengths are also quite small, with values of 70Å or less [23]. EB-1 class is formed as a result of un-doping (deprotonation) of emeraldine salt ES-1 and is reported to be

amorphous. The amorphous polymer retains memory of its corresponding base or salt state. For example protonation (doping) of amorphous EB-1 or EB-2 results in partially crystalline ES-1 or ES-2 respectively. Recent studies of water influence on the structural properties of polyaniline demonstrate the important role of absorbed irreversible "structural" water molecules on the crystalline properties of polyaniline [24].

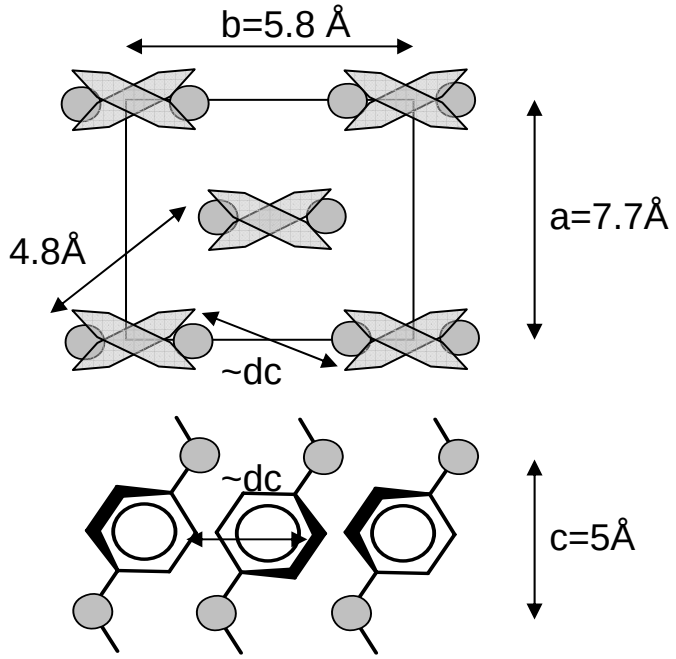

Fig. A.2.6 Unit cell of emeraldine base

Structural evolutions in the doped state

The conducting polymers are semiconducting in their ground undoped state. The doping procedures induce local electronic excitations necessary for charge transport and higher electrical conductivity. Typically doping concentrations in conducting polymers are much higher compare to classical semiconductors and may achieve one dopant ion per one monomer unit. The overall charge neutrality in the system requires uniform distribution of dopant ions in the polymer host matrix. Doping-induced structural evolution is strongly affected by the particular anisotropy of polymer chains, with strong covalent bonding along the chains and much weaker inter-molecular interaction between neighboring polymer chains. The ordering of such guest-host system may be described in equatorial direction perpendicular to the polymer chains and along the chains separately [25]. Many structural phases depending on dopant and chain properties in doped conducting polymers were

reported. In general they may be divided into two characteristic groups forming channel or layered structures.

Channel structures

The channel structures are forming usually for small dopant molecules. The dopant ions fill up the quasi-one-dimensional channels surrounded by some number of polymer main chains. The forming of channel sites is usually associated with cooperative rotation of polymer chains around their chain axes [26] [27] [28] [29] [30]. The various reported channel schematic 2D structures are shown on fig(A.2.7). Examples of conducting polymers exhibiting channel structure are shown in fig(A.2.8).

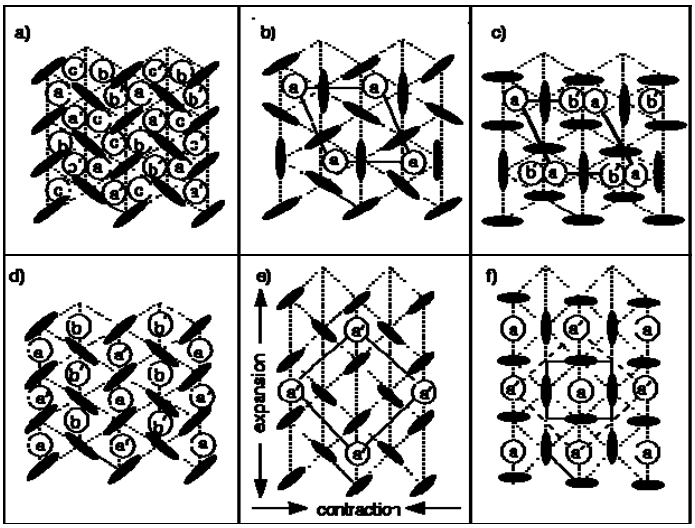

Fig. A.2.7 Schematic view of different channel structures reported in doped conducting polymers.

Layered structures

Sometimes layered organization in dopant-conducting polymer is more energetically favorable. Layered structures were reported often for molecular dopants of bigger sizes or anisotropic shapes. Some conducting polymer chains also prefer to stay in stacks (polyaniline with overlapping π-orbitals of neighboring chains) separated by dopant molecules layers. Examples of such structures are also shown in Fig. A.2.8. [31][32][33].

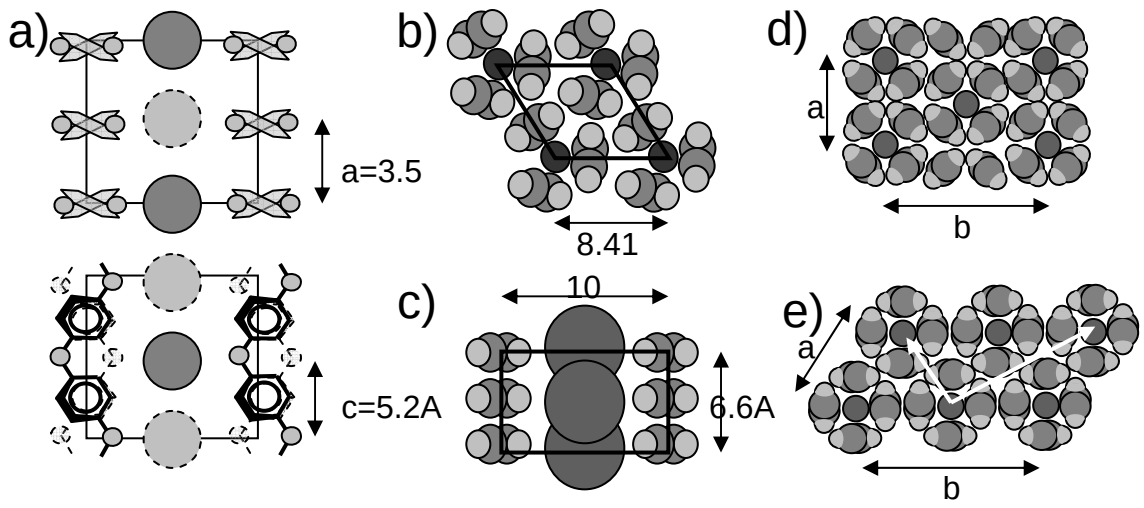

Fig. A.2.8 Various examples of the structure of doped conducting polymers. Layered structures: a) emeraldine salt of HCl acid structure ES-2, c) structure of PPV doped with AsF_3, SbF_3, ClO_4^- or H_2SO_4. Channel structures: b) hexagonal ordering with three fold structure of Na-doped PPV, e) and f) four fold structures of polyacetylene doped with potassium and rubidium respectively

Polymers with flexible side chains

Hairy-rod polymers

The addition of flexible side chains to the stiff conducting polymer backbone is the most effective procedure for obtaining soluble and processable materials. Using this approach it is possible to create new materials that exhibit the structural properties that do not exist in unsubstituted host such as lyotropic liquid crystallinity and structural self-assembly [34]. The majority of side-chain containing conducting polymers consists of alkyl, alkoxy, or phenylalkyl side chains of varying lengths that are chemically substituted at various hydrogen atom sites along the conducting polymer chain. The common example of this type of substitution is Poly(3-alkyl thiophene) P3AT [35] (Fig.A.2.9).The other approach is to use functionalized dopants containing flexible tails for doping unsubstituted linear host conducting polymers. The conducting polymer preparation employing this approach is the doping of polyaniline with various surfactants. Possible self-assembled structures of hairy-rod conducting polymers are shown in figs (A.2.10) and (A.2.11).

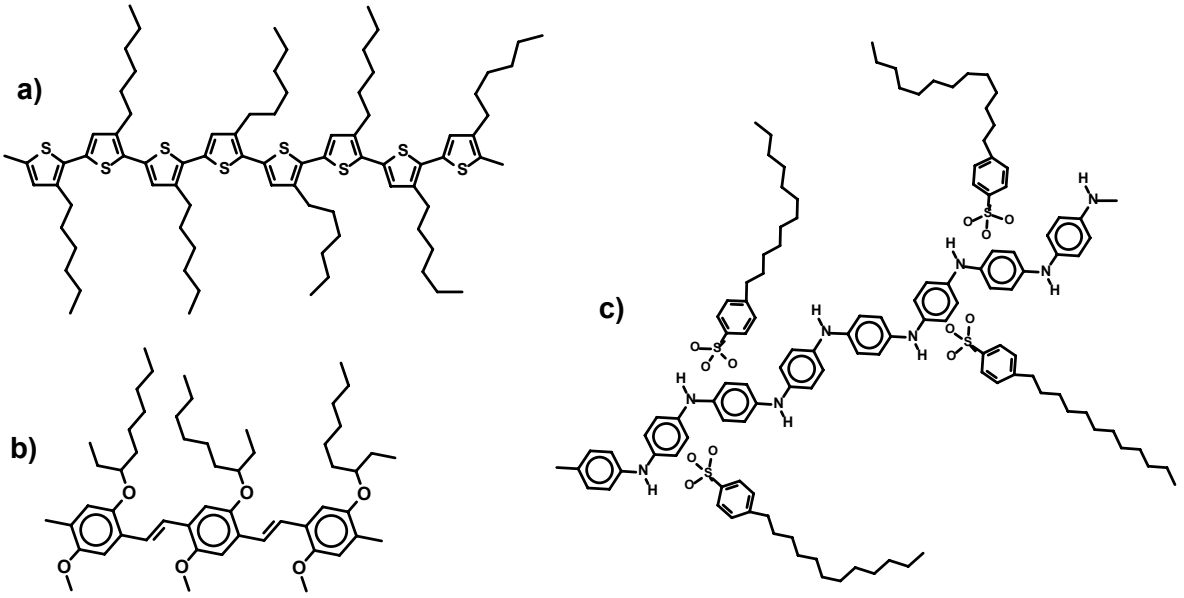

Fig. A.2.9 Chemical structure of conducting polymers with flexible side groups a) chemically substituted regioregular poly(3-hexyl-thiophene) (P3HT), b) MEH-PPV c) Polyaniline protonated with functionalized acid DBSA, The side groups (counter-ions) are connected to the polymer backbone by ionic interaction.

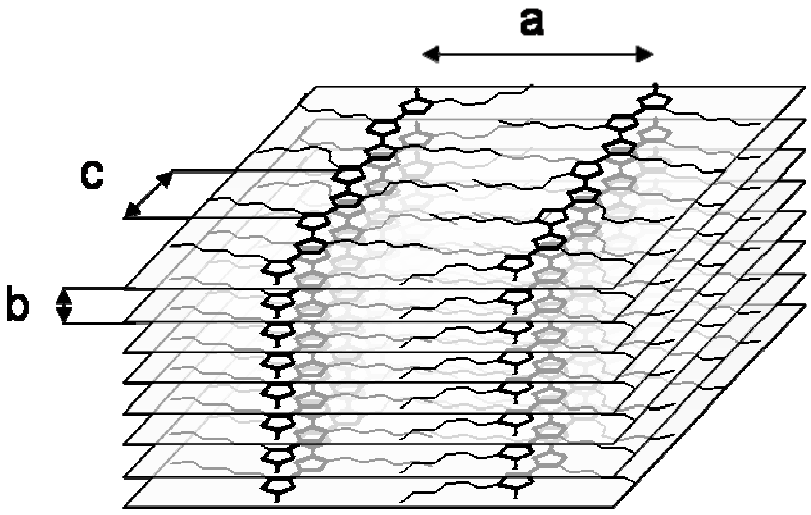

Fig. A.2.10 Structural organization (lamellar stacking) proposed for P3HT.

Functionalized dopants

The lamellar like self-assembled structure organization is frequently observed in systems containing relatively stiff chains of conducting polymers doped with surfactant type ions with long flexible tails. This type of organization was postulated for polypyrrole doped with n-alkylsulfates and for polyaniline doped with dodecylbenzene sulfonic acid DBSA [36]. Similar lamellar organization with conducting polymers stacks forming layers separated by layers of doping counter-ions have been proposed for polyaniline doped with camphorsulphonic acid CSA Fig.A.2.11[37].

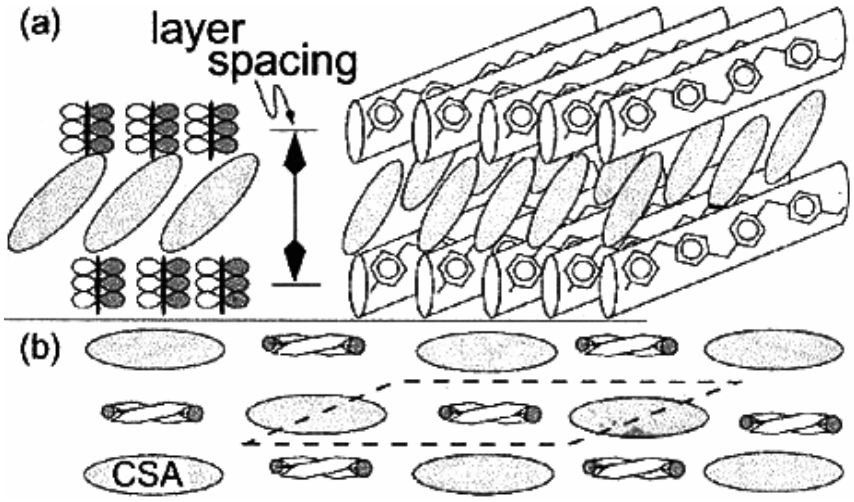

Fig. A.2.11 Lamellar structures proposed for polyaniline doped with CSA

A.3 Conductivity in polymers

Introduction

Conventional polymers are known as good insulators. The insulating properties of polymers are determined by the chemical structure of polymeric chains since the valence electrons of main chain atoms are included in covalent bonding with neighboring atoms and localized. This is in contrast to metals where electrons are free mobile in entire sample. Localization of electrons leads to a wide energy gap in the electronic band structure and the electrical conductivity is similar to typical insulating materials between 10^{-18} and 10^{-8} S/cm.

The family of conducting polymers differs from the conventional polymers by possessing the particular chemical structure with the extended π-conjugated system that is formed by the overlap of carbon p_z orbitals and alternating single and double bond lengths along the polymer chains. This particular conjugation of chains gives rise to distinct electronic properties of non-doped conducting polymers. The unpaired p_z electrons may contribute in electrical transport of the system. The electrical conductivity of such polymers vary in a very wide range from insulating form up to highly conducting metallic conductivity similar to copper conductivity around 10^5 S/cm, but in un-doped state they are semiconducting or insulating due to the chains dimerisation leading to an energy gap in the band structure. It is relatively easy to modify the electrical properties of the conducting polymers by chemical doping. This doping procedure may permanently increase the conductivity of even 15 orders of magnitude. The main difference between chemical doping of conducting polymers and doping of standard semiconductors is that in standard semiconductors the electron can be removed from the valence band while the whole structure remains rigid, in contrast to conducting polymers where the electronic excitations are accompanied by a disorder or relaxation of the lattice around the excitation which results in defect states along the polymer chains [38]. The chemical doping of conducting polymers typically is a redox reaction which changes the oxidation state of polymer chains by removing electrons from valence band or adding to the conduction band. Typical example of this technique is p- or n-type doping of polyacetylene. The other doping technique is using protonic acid for doping is called nonredox since the number of electrons associated with the polymer chain after doping remains unchanged (i.e doping of polyaniline) (see part B). The electrical behavior of conducting polymers is determined by several prominent aspects: individual chain properties, interchain interactions, interaction between chains and dopants, structural disorder, sample morphology and finally sample preparation conditions. The electrical conductivity of various conducting polymers depending on doping procedures compared to that of other classical materials are illustrated in the fig (A.3.1).

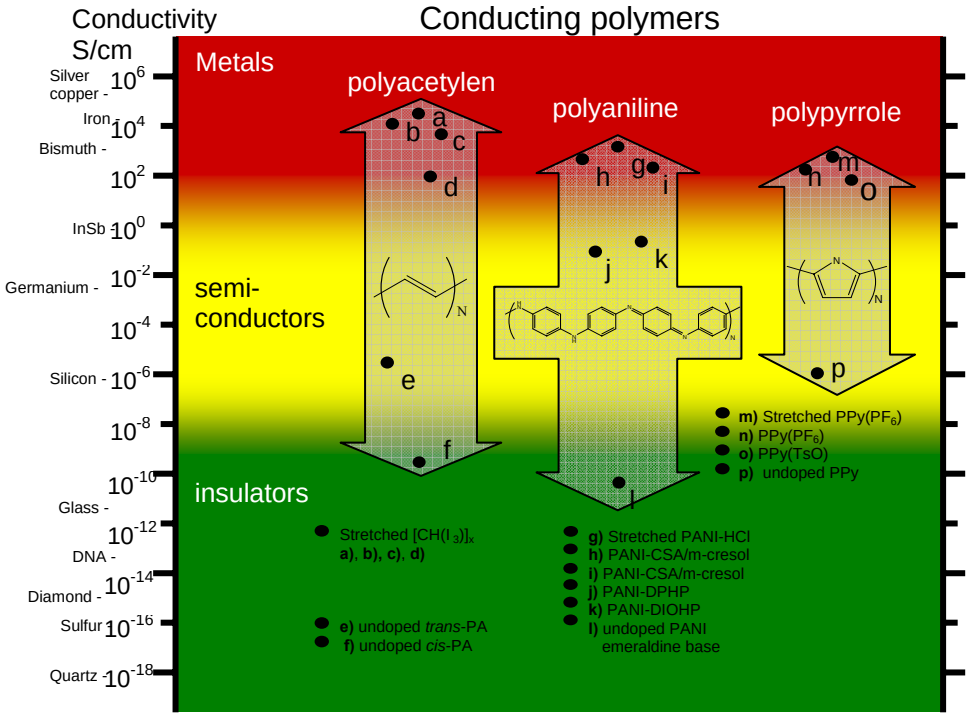

Fig. A.3.1 Electrical conductivity of conducting polymers. From ref: a)[39], b)[40], c)[41][42], d)[43], e)[44], f)[45]

Mechanisms of conductivity

In general there are two fundamental mechanisms of charge transport in condensed matter: hopping and band transport. In band transport mechanism due to extended states, known as bands, the charge carriers (electrons) behave as "free particles". The electrons are moving freely accelerated by the applied electric field loosing their momentum through scattering by impurities (defects) and phonons. In a band transport phonons are a source of resistance and the conductivity decreases with an increase of temperature as an effect of more intense phonon scattering. The electron motion may be described as quantum diffusion. This conductivity behavior occurs in bulk metals with small and moderate disorder. Band transport mechanism of conductivity leads to non-zero conductivity at 0 K, which is determined by the scattering on the impurities and lattice defects. In the hopping mechanism the electrons are hopping between localized states by absorbing or emitting phonons. Since the charge carriers are localized the external energy of phonons is necessary to initiate the electron jumps. The electronic transport is realized as a random walk of successively hopping electrons. This process may be described as classical incoherent diffusion and is inelastic. In contrast to band transport, in hopping mechanism phonons are the source of electrical conductivity. The hopping conductivity increases with temperature and vanishes at 0 K. Hopping transport is a

general mechanism for the electrical conductivity of disordered materials with localized electronic states such as doped semiconductors and glassy materials. The probability of a hopping event depends on the physical distance to another site/chain and the difference in energy between the sites. Hence, the extent of the hopping and the hopping range are limited by the available energy of phonons. As the temperature increases more phonons of higher energy becomes available and the electrons can hop to states further and further away or higher in energy. Obviously, the localization length L_{loc} of the electronic states strongly influences the hopping rates. The degree of charge carrier localization depends on the amount of structural disorder in the material, and well ordered films are thus expected to have better charge transport properties.

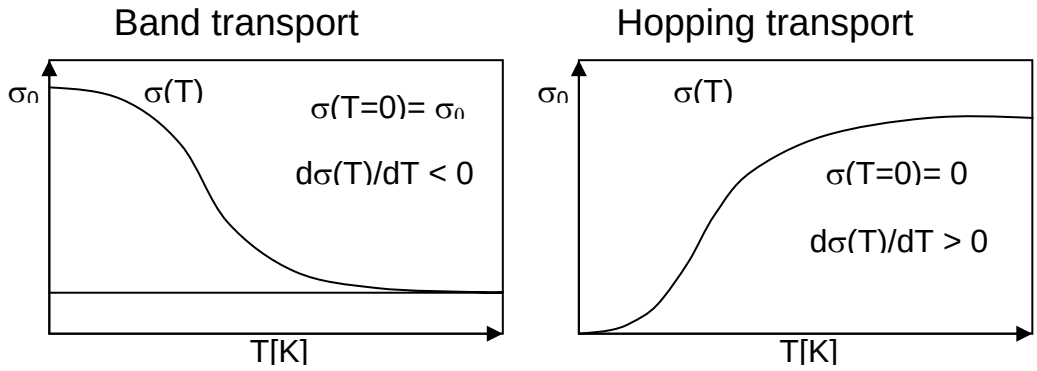

Fig. A.3.2 Characteristic temperature dependences of electrical conductivity for different transport mechanisms

The nature of electrical conductivity of conducting polymers can not be completely accounted for by considering only one of the mechanisms described above, because of their complex structure. The interplay of strongly disordered (amorphous) parts and the relatively well ordered crystalline regions play the crucial role for the global electronic properties of the system. The nature of local electronic transport in crystalline and amorphous regions is also strongly determined by the molecular anisotropy of polymeric chains, its flexibility and possible conformations. Some conducting polymers exhibits the electrical conductivity temperature dependence characteristic for semiconductors, others show metal-insulator like transitions. The unique mixture of band and hopping mechanisms of electrical conductivity resulting in the difficulty of development of the one complete (describing all feature) model of electrical transport in conducting polymers. As a consequence many models of electronic transport have been proposed and the electrical phenomena of conducting polymers are still strongly debated.

Charge transport in inhomogeneous disordered conducting polymers.

Conducting polymers in majority are not homogeneously disordered, being partially crystalline and partially disordered. If the localization length L_{loc} of electrons in disordered parts is comparable or smaller than the crystalline coherence lengths, then the disorder present in the conducting polymer is viewed as inhomogeneous[46]. The schematic view of inhomogeneously disordered polymer is shown in Fig (A.3.3). In this approach the polymer structure consists of crystalline regions considered as nanoscale metallic islands (grains) embedded in an amorphous poorly conducting medium. Electronic wave functions are delocalized inside the well ordered islands due to good overlap between the chains and the metallic type band transport may occur. Outside the crystalline regions the chain order is poor and the electronic wave functions are strongly localized (small localization length L_{loc}). Due to its high molecular weight individual polymeric chains may belong to more than one well ordered metallic island and form an amorphous network between neighboring islands.

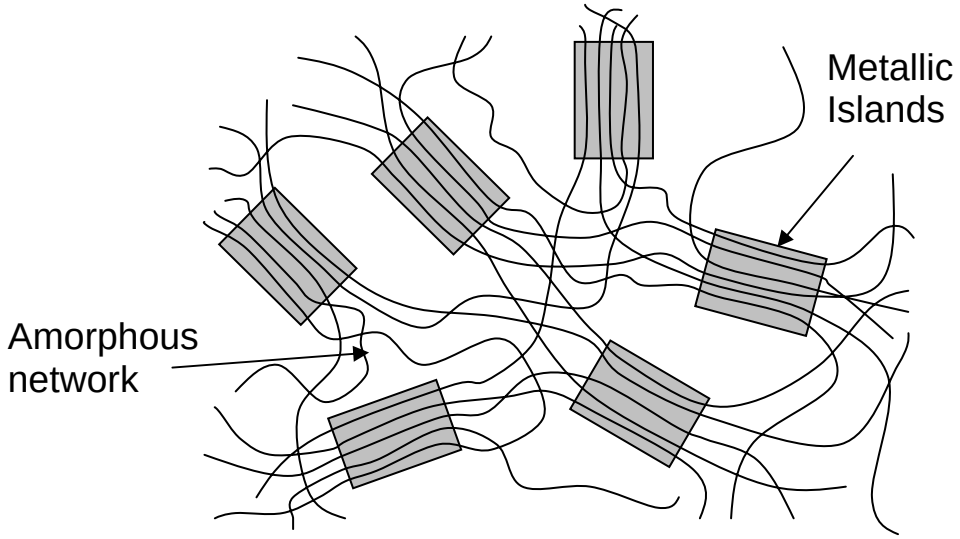

Fig. A.3.3 Schematic view of inhomogeneous disorder in conducting polymers

The electrons participating in charge transport moving through high mobility metallic regions meet barriers of low mobility regions at the edge of grains. The disordered amorphous regions extend between ordered regions in the distance comparable to the metallic island sizes (i.e. 50% of crystallinity) therefore direct tunneling of charge carriers between metallic regions should be suppressed. Instead of direct tunneling the model of mechanism of quantum resonance hopping between metallic grains was proposed [47]. In

this mechanism inter grain charge transfer is effectively provided by tunneling through resonance states in the amorphous regions Fig (A.3.4). The morphology of polymeric chains in disordered inter grains regions play the crucial role for charge transport in inhomogeneous polymer, since the charge localization is the main source of electrical resistivity. Hopping transport through the low mobility regions may be the main limiting factor for the overall mobility in the system. Localization length L_{loc}, essential for charge in transport through the localized states, depends on the morphology of disordered regions. L_{loc} is larger for rod-like (with more parallel chains) and smaller for coil-like morphology of inter grain amorphous network.

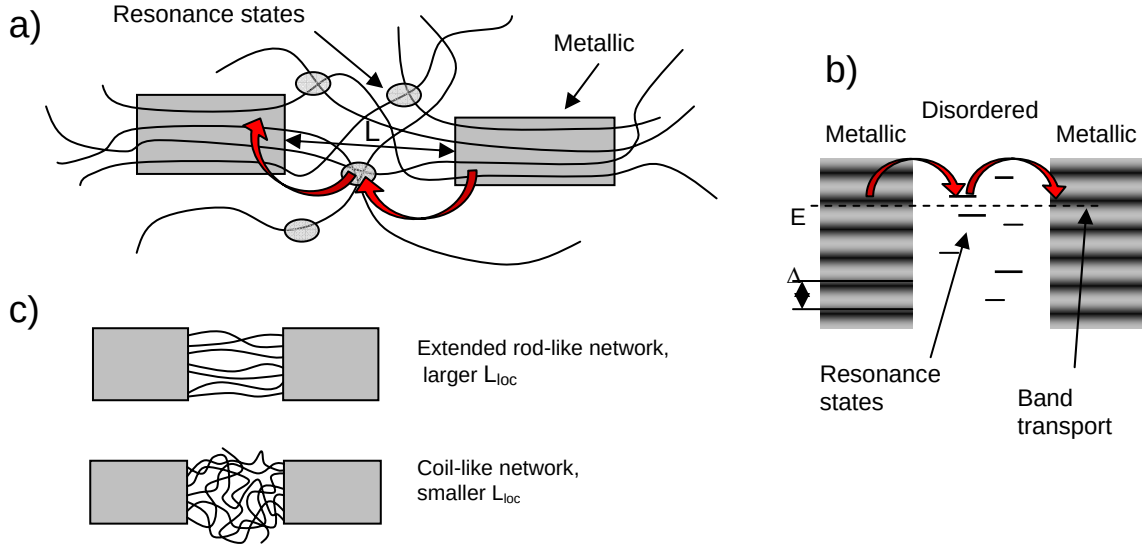

Fig. A.3.4 a) the electrical coupling between metallic grains provided by resonance tunneling through the localized states b) bands structure in coupling regions c) schematic view of amorphous network morphology which may influence the electrical transport in the system.

The global electrical behavior of inhomogeneously disordered conducting polymers is a superposition of several phenomena occurring in different parts of the system. The metallic state may be induced by the improvement of ordering of polymer chains inside the crystallites (strengthening of interchain interaction), but also by strengthening the coupling between metallic regions which depend upon the amorphous cross-links morphology.

B. Polyaniline

B.1 General info. Chemical formulae

The base form of polyaniline may be described with the general formula:

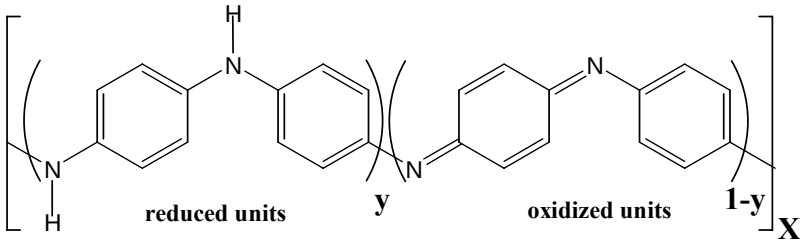

Fig. B.1.1 General formula of polyaniline

The polyaniline chain consists of alternating reduced and oxidized units. The average oxidation state can be varied continuously from y=1 to give the completely reduced form called "leucoemeraldine", to y=0.5 to give half-oxidized form "emeraldine", to y=0 to give the completely oxidized form "pernigraniline". The half-oxidized emeraldine base form of polyaniline commonly abbreviated as PANI is very stable and easy to convert to the highly conducting emeraldine salt by chemical reaction with protonic acids. In our studies we only used emeraldine form of polyaniline.

B.2 The protonic doping of PANI and how it allowed a dopant engineering

There are two possibilities for chemical doping of the conducting polymers: the "redox" oxidative doping or "non-redox" protonic acids doping. Conducting polymers like poly(acetylene), poly(thiophene) or polyaniline (leucoemeraldine) undergo p- or n-redox doping by chemical process during which the number of electrons assisted with polymer chain changes. The protonic acids doping "non-redox" process differ from "redox" doping in that the number of electrons assisted with polymer chain does not change during the doping process and new electronic states are introduced by protonation. The polyaniline in emeraldine base form was the first organic polymer which was converted to highly conducting form by the process of this type to produce an environmentally stable polysemiquinone radical cation [48].

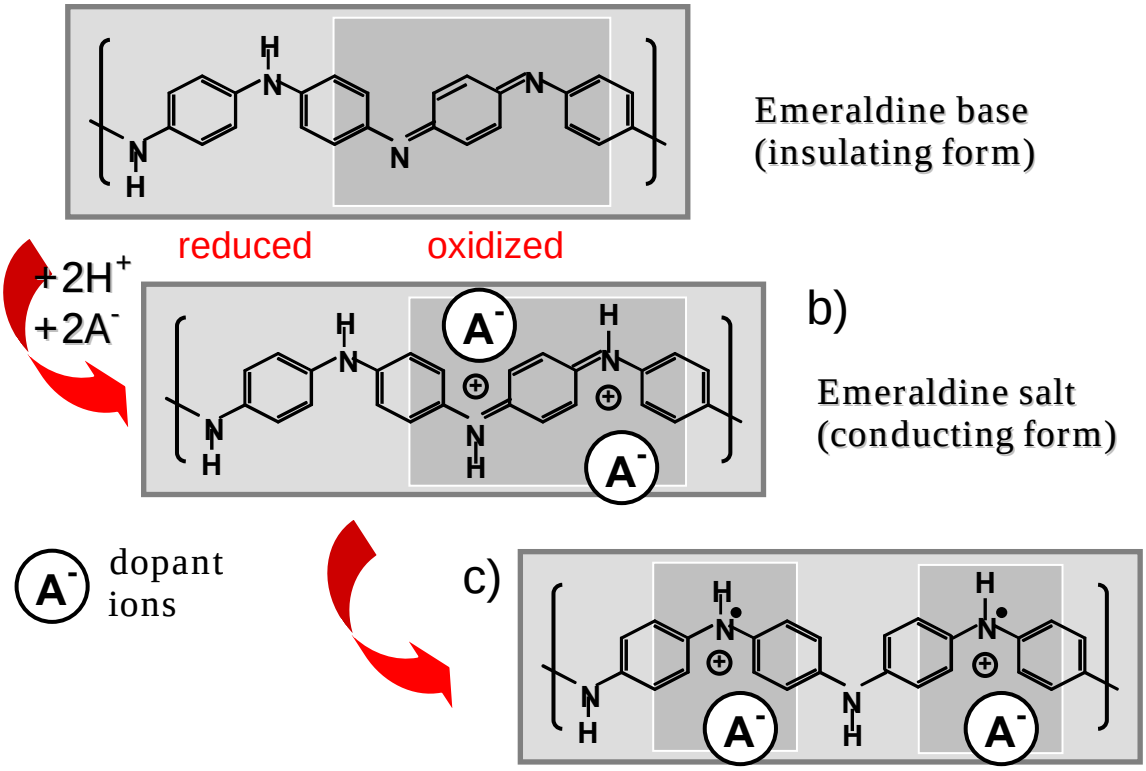

Fig. B.2.1 Protonic acid doping of polyaniline

Emeraldine base form of polyaniline (PANI) can be doped (protonated) with sufficiently strong protonic acid to give the corresponding emeraldine salt. This process is shown in fig. (B.2.1).. It is known from XPS and other spectroscopic studies that imine nitrogen are preferentially protonated [49]. Thus protonation of PANI (see fig B.2.1 a) gives

first the product in which the charge is stored in a form of bipolarons (see fig B.2.1 b). Then a charge redistribution occurs which can be considered as an internal redox process which transforms these bipolarons into polarons (so-called polaron lattice) (see fig B.2.1 c).The polymer chain adopts the structure of a poly(semi-quinone) radical.

Upon the doping process electronic, vibrational and other properties of polyaniline are strongly altered as well as its supramolecular structure. The most spectacular result of the doping is the increase of electrical conductivity over several orders of magnitude.

There is also another prominent aspect of protonic acid doping method of polyaniline especially important from technological point of view, since upon doping process only proton from protonating acid is transferred and chemically bonded to polymer chain, the rest of the acid molecule can vary in chemical structure, size and shape without change of electronic properties of the polymer chain. The rest of the acid molecule (negatively charged ion) stays connected to positively charged polyaniline chain via electrostatic interaction. This feature of protonic acid doping allows the dopant engineering which results in the development of several families of functionalized dopants which induce additional properties to the polyaniline based material while conserving its electrical properties.

B.3 Processibility and plasticization of polyaniline

B.3.1 Doping induced processibility

The unsubstituted conjugated polymers like polyaniline or polythiophene are generally insoluble. This is associated with the rigidity of their chains and strong interchain interactions. The typical procedure of rendering rigid-chain polymers soluble is to attach flexible side groups to the stiff polymer backbone. Such approach resulted in the preparation of soluble derivatives of polythiophene with flexible alkyl tails covalently attached to the backbone. However conducting polymers substituted this way are still in their undoped form and upon doping they become insoluble what is inconvenient from a technological point of view. The idea of the preparation of conductive polymers processible in their doped state is slightly different. The processing improving groups are introduced to the polymer matrix not as a side groups attached to the polymer backbone by the covalent bond but rather as an inherent part of doping anions. This method is widely used for preparation of conducting polyaniline processible in their doped state. The above outlined approach can be exemplified by the design of several dopants from the families of sulfonic [50][51] and phosphonic [52] acids as

well as phosphoric acid esters [53] which in addition to their doping functions contain chemical constituents improving the polymer processibility in its doped (conducting) state (fig. (B.3.1))

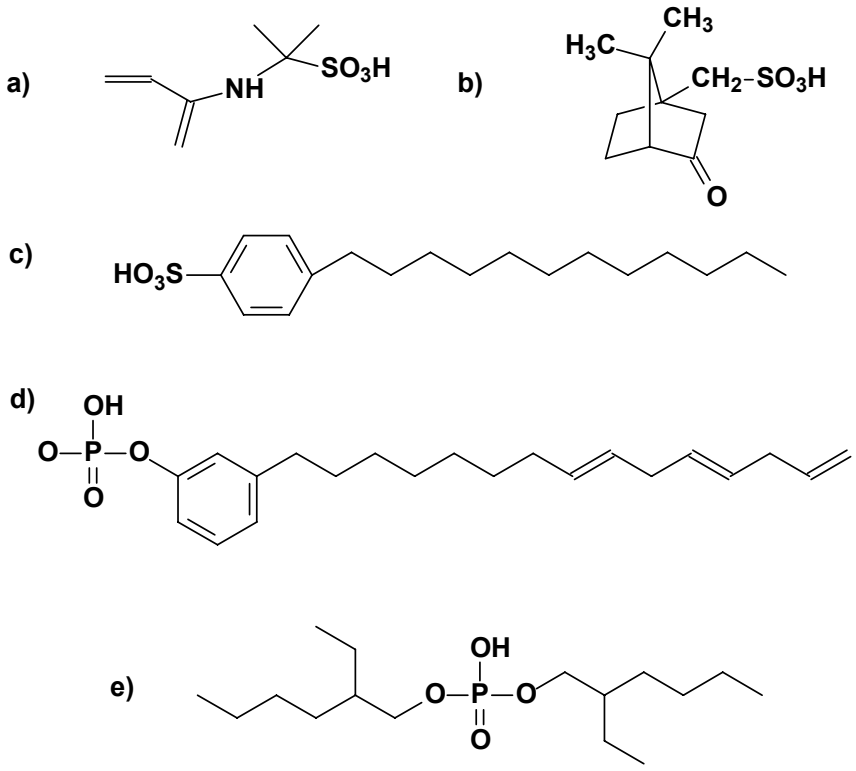

Fig. B.3.1 Protonic acids used for preparation of conducting polyaniline in their doped state

B.3.2 "Plast-doping" of PANI

The best results of electrical conductivity of polyaniline were found in the polyaniline doped with "camphor sulfonic acid /CSA". The highly conducting free standing films of polyaniline obtained from the solutions of Polyaniline and CSA mixtures with meta-cresol have very poor mechanical properties. For this reason they are difficult to use for any practical applications. Additionally the solvent meta-cresol is very difficult to remove from the system due to the hydrogen bonding between solvent and CSA molecules. Even 15 to 20 weight percents of toxic meta-cresol is still present in prepared films. These residual solvent molecules then migrate slowly to the surface of the film and evaporate. As a consequence the properties of the film are still changing in time. Because of these inconvenient limitations it was necessary to develop a new system based on polyaniline. This system must have much

better and stable mechanical properties and must be easy to processing while conserving the high electrical conductivity of PANI/CSA system.

There are several strategies we can choose to develop such systems. One way is to develop new family of doping molecules. These molecules usually derivatives of sulfonic or phosphoric acids may have two functions. They both influence insulator-metal transition (protonate polyaniline) and plasticisize the system to obtain better mechanical properties. The doping molecules with such properties are called “plast-dopants”. Plast-dopants may be used to prepare conducting compounds with or without any solvent depending on their properties. Conducting polyaniline prepared by mechanical mixing of polyaniline with plast-dopant in proper molar ratio, is free of any residual solvents always present in the films prepared from solution. The advantage of this method is that we are sure the system has only two components but disadvantage is that we don’t know if the system is homogenized. The new family of doping molecules (figs(B.3.2 and B.3.3) allows preparing the conducting films from a solution of less toxic than meta-cresol solvents as “dichloroacetic acids” (DCAA) obtaining stable films of good quality with very small amount of residual solvents.

The other strategy is to develop the system consisting of three components, a polyaniline, a doping molecule and a plasticizer molecule. The method is well known and commonly utilized for plasticizing conventional polymers. Several commercially used plasticizers such as various phosphoric acid triesters were used to plasticize conducting polyaniline compounds. The main disadvantage of this strategy is that system with so many components is complex and its quite difficult to be described and to control its supra-molecular structure.

The third option is based on mixing of polyaniline/CSA system with conventional polymers like poly-methyl-metacrylate (PMMA) or polystyrene (PS) which has very good mechanical properties. The composites obtained this way are very complex usually. It is possible to prepare conducting films with relatively small amount of polyaniline less than 1% but the electrical conductivity is decreased of several orders of magnitude. There are many studies of such systems.

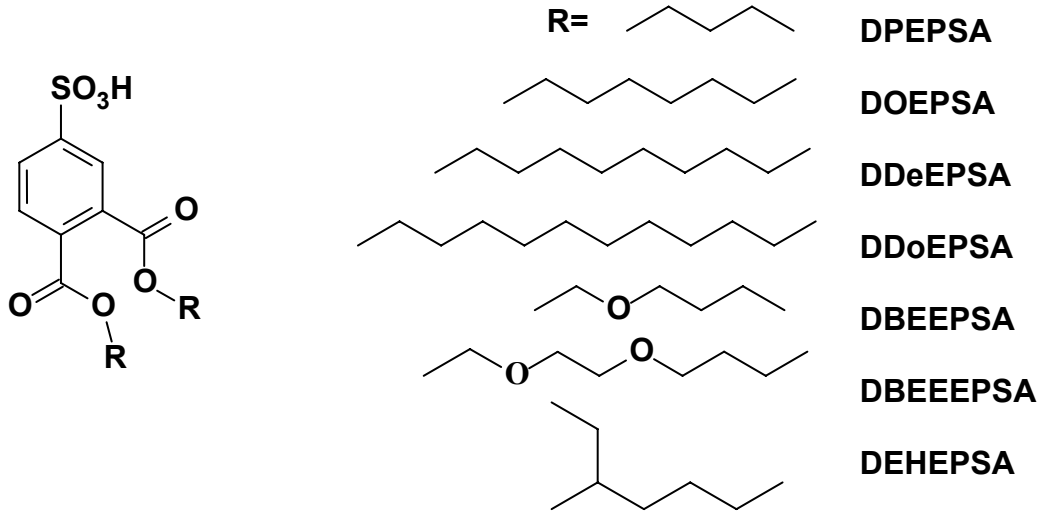

Fig. B.3.2 diesters of 4-phthalosulfonic acids (1st generation of plastdopants termed DEPSA)

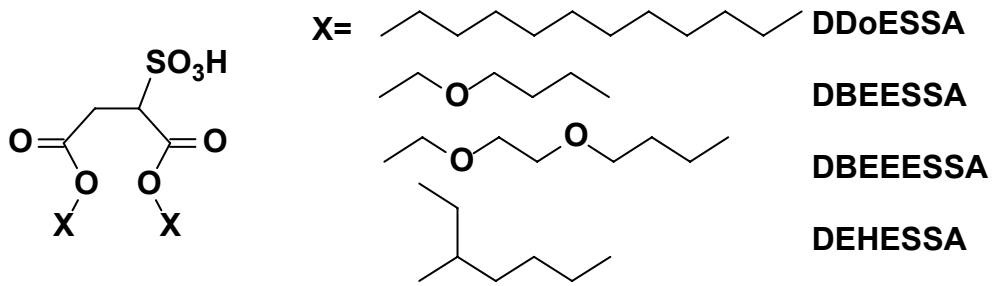

Fig. B.3.3 diesters of sulfosuccinic acid (2nd generation of plastdopants termed DESSA)

Diesters of sulfophtalic and sulfosuccinic acids (fig. B.3.2 and B.3.3 respectively) combine polyaniline doping ability with plasticizing properties. Alkyl and alkoxy tails of these diesters render polyaniline soluble in DCAA and other solvents. The films cast from this solvent are flexible, can be bent several times without damage and show elongation at break exceeding 190% (see fig.B.3.4). In Fig.B.3.5 is shown the temperature dependence of macroscopic DC conductivity of free-standing films of polyaniline doped with diester of sulfophtalic acids. Electrical conductivity, stretchability, and temperatures of glass transitions for 1st and 2 generation plast-dopants are collected in table B.1.1 [54] .

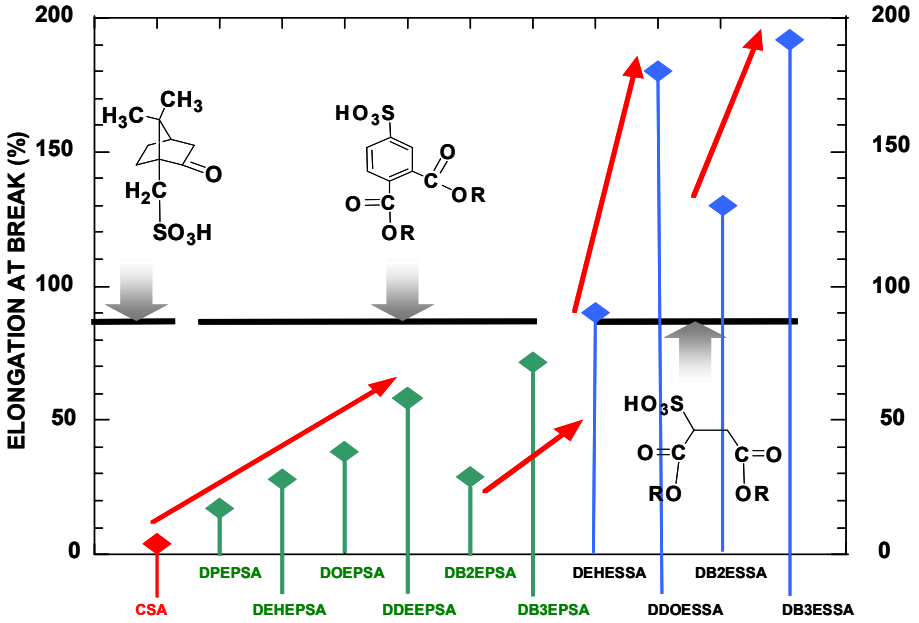

Fig. B.3.4 Stretchability of free-standing films

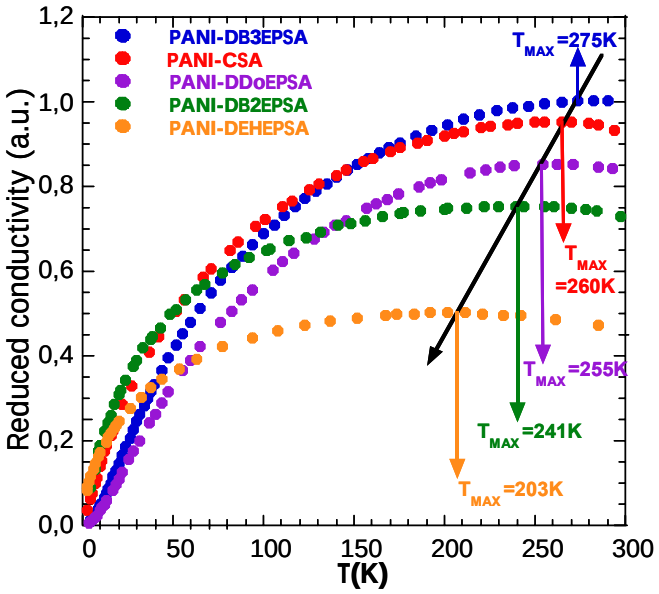

Fig. B.3.5 Temperature dependence of macroscopic DC conductivity for free-standing films.

Table B.1.1

DEPSA protonated PANI film	Tg_1 [K]	Tg_2 [K]	$\Delta l/l_0$ [%]	σ_{dc} [$S.cm^{-1}$]	DESSA Protonated PANI film	Tg_1 [K]	Tg_2 [K]	$\Delta l/l_0$ [%]	σ_{dc} [$S.cm^{-1}$]
PANI/DPEPSA	257	304	17	138	PANI/DEHESSA	228	294	90	110
PANI/DEHEPSA	-	283	28	115	PANI/DDoESSA	249	-	180	97
PANI/DOEPSA	-	299	39	100	PANI/DB2ESSA	-	294	130	125
PANI/DDeEPSA	208	-	58	59	PANI/DB3ESSA	221	302	195	90
PANI/DDoEPSA	243	-	78	79					
PANI/DB2EPSA	-	301	29	172					
PANI/DB3EPSA	231	281	72	97					

C. Experimental section

C.1 Sample preparation

C.1.1 Synthesis of polyaniline

Polyaniline hydrochloride salt was synthesized by chemical oxidative polymerization of aniline at -27°C as described in [55]. It was then converted to Emeraldine Base (EB) by treatment with 0.1M aq. NH_3 solution for 72 h and dried till constant mass under dynamic vacuum of ca. 10^{-6} mbar. The 0.1wt% solution of EB in 96wt% H_2SO_4 showed an inherent viscosity of 2.25 $dl.g^{-1}$.

C.1.2 Plast-dopants

Two types of protonating agents were used as dopants: diesters of 4-phthalosulfonic acids (1st generation of plastdopants termed DEPSA), and diesters of sulfosuccinic acid (2nd generation of plastdopants termed DESSA). DEPSA and DESSA alkyl and alkoxy derivatives were synthesized according to the method developed in [4,6]: di(2-ethylhexyl) ester of 4-phthalosulfonic acid (DEHEPSA), di-*n*-dodecyl ester of 4-phthalosulfonic acid (DDOEPSA), di(2-butoxyethyl) ester of 4-phthalosulfonic acid (DB2EPSA), di(2-ethylhexyl) ester of sulfosuccinic acid (DEHESSA), di-*n*-dodecyl ester of sulfosuccinic acid (DDOESSA), and di(2-(2-butoxy-ethoxy)ethyl) ester of sulfosuccinic acid (DB3ESSA).

C.1.3 Preparation of plast-doped polyaniline films

0.5wt% PANI/dopant solutions in 2,2'-dichloroacetic acid (DCA) were prepared by extending mixing of the components at room temperature followed by filtration through a 0.2 μm PTFE filter. Free-standing films of ca. 20μm thickness were obtained by solution-casting on a polypropylene substrate at 318K.

Free-standing thin films of PANI/DEHESSA and PANI/DB3ESSA were mechanically stretched at room temperature with a drawing speed: 1mm/mn.

C.2 X-ray scattering

C.2.1 X-ray diffraction theory

X-ray diffraction is the main tool in structural study of conducting polymers on supramolecular level. X-rays are used because their wavelengths are comparable to the sizes of atoms and molecules, giving rise to diffraction effects by crystals. Diffraction studies give important information about crystallographic structure, structural anisotropy coherence length and degree of crystallinity.

Scattering vector

It is convenient to define the scattering vector ***q*** by:

$$\vec{q} = \vec{k}_f - \vec{k}_i, \quad \left|\vec{k}_f\right| = \left|\vec{k}_i\right| = \frac{2\pi}{\lambda} \qquad \text{(C.2.1)}$$

Where $\boldsymbol{k_f}$ and $\boldsymbol{k_i}$ are final and incident beam wave vectors respectively, $\boldsymbol{\lambda}$ is a wavelength of X-ray beam. The modulus of scattering vector $|q|$ is related to scattering angle θ by equation:

$$\left|\vec{q}\right| = 2\left|\vec{k}_i\right|\sin\theta = \frac{4\pi\sin\theta}{\lambda} \qquad \text{(C.2.2)}$$

Real space crystal lattice, reciprocal lattice, Miller indices.

Crystal lattice is defined in real space by the collection of vectors $\vec{R}$ **:**

$$\vec{R} = u_1\vec{a}_1 + u_2\vec{a}_2 + u_3\vec{a}_3 \qquad \text{(C.2.3)}$$

Where: $\left[\vec{a}_1, \vec{a}_2, \vec{a}_3\right]$ are primitive lattice vectors and $[u_1, u_2, u_3]$ are integers.

The reciprocal lattice is a useful mathematical construction being the spatial Fourier transform of the real space lattice. The reciprocal lattice vectors $\vec{G}$ are given by:

$$\vec{G} = v_1 \vec{b}_1 + v_2 \vec{b}_2 + v_3 \vec{b}_3 \qquad \text{(C.2.4)}$$

where: $\left[\vec{b}_1, \vec{b}_2, \vec{b}_3\right]$ are primitive reciprocal lattice vectors and $\left[v_1, v_2, v_3\right]$ are integers.

The primitive vectors for reciprocal lattice are related to those for real space lattice by:

$$\vec{b}_1 = 2\pi \frac{\vec{a}_2 \times \vec{a}_3}{V}, \vec{b}_2 = 2\pi \frac{\vec{a}_3 \times \vec{a}_1}{V}, \vec{b}_3 = 2\pi \frac{\vec{a}_1 \times \vec{a}_2}{V} \qquad \text{(C.2.5)}$$

For every reciprocal lattice vector $\vec{G}$ there is a set of parallel planes which are perpendicular to $\vec{G}$. The distance between these adjacent planes is given by:

$$d = \frac{2\pi}{\left|\vec{G}\right|} \qquad \text{(C.2.6)}$$

Parallel, equivalent planes are usually denoted with Miller indices [*hkl*]. The reciprocal lattice vector associated with these Miller indices is $\vec{G}_{hkl} = h\vec{b}_1 + k\vec{b}_2 + l\vec{b}_3$ (C.2.7)

Laue condition, Bragg's law

The Laue condition for diffraction is fulfilled whenever the scattering vector ***q*** coincidence with a reciprocal lattice vector. $\vec{G} = \vec{q}$ This is equivalent to the familiar Bragg's law, since part of the Laue condition is $\left|\vec{q}\right| = \left|\vec{G}\right|$ and from eq. (C.2.2) and eq. (C.2.6):

$$\frac{4\pi \sin\theta}{\lambda} = \frac{2\pi}{d_{hkl}} \Rightarrow \lambda = 2d_{hkl} \sin\theta \qquad \text{(C.2.8)}$$

Which is the Bragg condition.

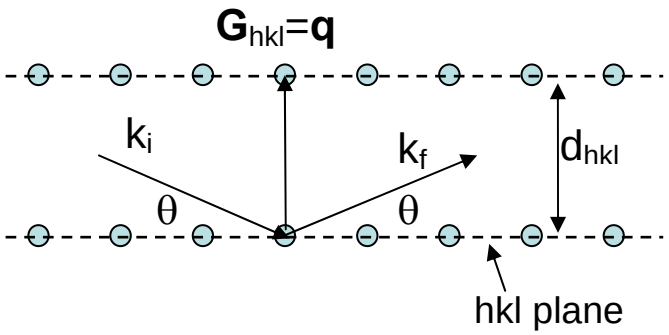

Fig. C.2.1 Schematic illustration of Laue and Bragg condition

Structure factor and diffraction peak intensity

Whereas the position of possible reflections from a given periodic geometry is given by Bragg's law, the peak intensities I_{hkl} are determined by square of the structure factor F_{hkl}:

$$I_{hkl} \sim \left|F_{hkl}\right|^2 \quad \text{(C.2.9)}$$

Where: $F_{hkl} = \sum_j^N f_j \exp\left[2\pi i\left(hx_j + ky_j + lz_j\right)\right]$, (C.2.10)

f_j - atomic form factor

Intensities of diffracted X-rays are due to interference effects of X-rays scattered by all the different atoms in the structure.

X-ray scattering by polymers

When considering X-ray diffractograms of polymers, it is important to realize they are very far from diffractograms of ideal crystals. As described in chapter A.2, polymers structures generally have a significant amorphous volume fraction. As a result of low average degree of order in polymers, the observed diffraction peaks are generally few and broad.

Sample anisotropy

For an isotropic sample, the diffracted intensity from individual crystallites fulfilling the Bragg's law is distributed on 'Debye-Scherrer rings'. The sample anisotropy may be revealed by intensity variation on these rings. Since ***q*** is defined by incident and final wave vectors (eq. (C.2.1)) the anisotropy of the orientation of crystallites can be probed by changing the experiment geometry (transmission or reflection) and by rotating the sample.

Coherence length

The width of Bragg peaks contains information about the coherence length (crystallites dimensions) in the sample. The Scherrer formula gives rough estimate of the crystallite dimensions:

$$L \approx \frac{0.9\lambda}{B\cos\theta} \quad \text{(C.2.11)}$$

Here, θ - is the half of scattering angle and B-the FWHM broadening of the diffraction peak.

Crystallinity index

The X-ray scattering pattern includes the intensity scattered from crystalline and amorphous regions and some background: $I_{total} = I_{crystal} + I_{amorphous} + I_{background}$ The crystallinity index X_c

$$X_c = \frac{\int I_{crystal}}{\int I_{crystal} + \int I_{amorphous}} \quad \text{(C.2.12)}$$

C.2.2 Wide angle scattering experiments (WAXS)

Wide Angle X-ray Diffraction (WAXS) measurements were carried out in θ/2θ reflection and transmission geometries using Cu K_α radiation (1.542 Å). The diffractometer was equipped with a 800 channels linear multi-detector giving a total aperture of 16° in 2θ (2θ being the scattering angle). The scan step was 0.06° (in 2θ) with a counting time of 15 s/step.

In general, raw data have to be folded with the instrumental resolution of the diffractometer. However in our case, broadening of peaks due to disordering is much larger than those of the instruments. We decided to use all experimental curves as measured just modified by a scaling factor accounting for the differences in size of the samples.

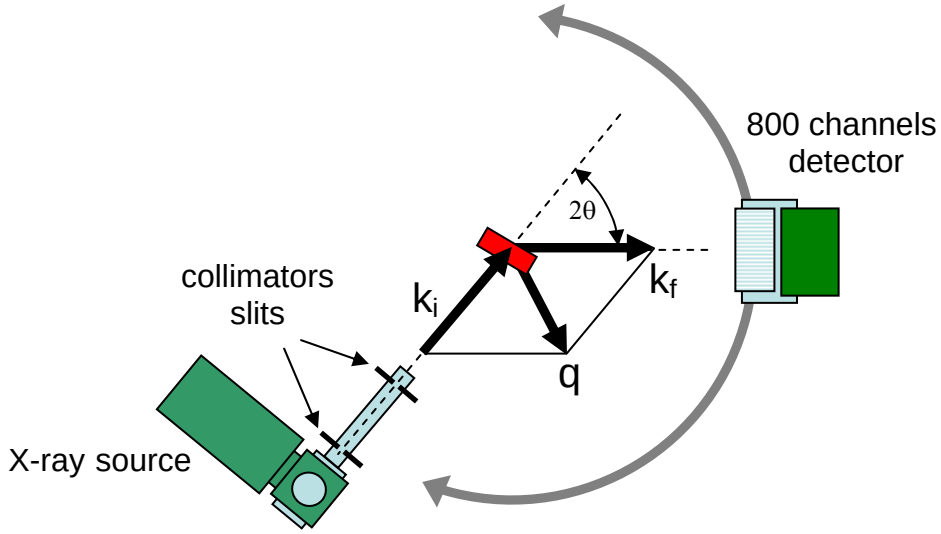

Fig. C.2.2 WAXS experiment

C.2.3 Small angle scattering experiments (SAXS)

Small Angle X-ray Scattering (SAXS) measurements on unstretched films were performed at the European Synchrotron Radiation Facility (ESRF, Grenoble – France) on the high q resolution; ($\Delta q/q \sim 10^{-3}$ - 10^{-4}) French CRG beam line D2AM using a monochromatic beam of 15 keV in energy (wavelength of 1.2 Å). A two-dimensional detector was located at 2.2 m from the sample position. The separation between two channels was 4.5 μm [56]. The two-dimensional scattering profiles of unstretched films were always found isotropically distributed within the plane of films. The background was systematically removed and the intensity was calibrated taking into account the effective efficiency of the detector. The one-dimensional profiles were then obtained by executing a 360° radial grouping of the total scattered intensity.

SAXS measurements performed on the series of stretched films were carried out on a home-built camera using a FR591 Nonius rotating Cu anode operating with a fine focus at a 6° takeoff angle corresponding to a 0.2x0.2 mm^2 apparent beam size. The beam was Kα/Kβ filtered (wavelength: λ=1.5418 Å) and focused in horizontal and vertical directions by total reflection from two curved Franks mirrors (Ni coated glass optical flats). Scattering patterns were recorded with a two-dimensional position sensitive gas-filled detector installed 132 mm from the sample. The sample-detector distance was calibrated using silver behenate as a standard.

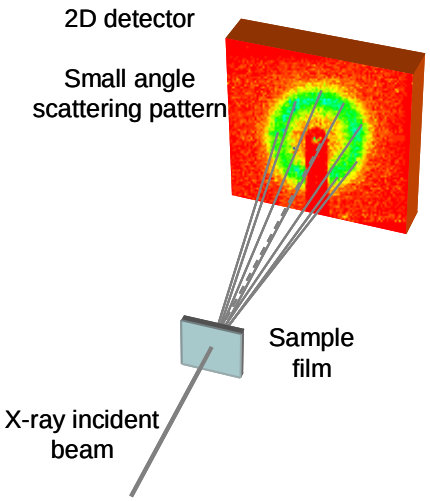

Fig. C.2.3 SAXS experiment

C.3 Incoherent neutron scattering

C.3.1 Neutron scattering theory

This section aims at giving a minimum of information about neutron scattering and especially about Incoherent Quasi-elastic Neutron Scattering (IQNS), referring to standard textbooks for a general survey of the neutron technique [57][58] [59] [60] or a description of quasi-elastic scattering [61] [62]. We want to point out a few general characteristics to which we shall refer in the analysis of the data.

In a typical neutron scattering experiment monochromatic neutrons exchange both energy, $\hbar\omega$ and momentum $\hbar\mathbf{Q}$ during the scattering process. The latter is defined as $\boldsymbol{Q} = \boldsymbol{k} - \boldsymbol{k}_0$ where $\boldsymbol{k}$ and $\boldsymbol{k}_0$ are the scattered and incident wave vectors, respectively. As the incoherent scattering length of the hydrogen atoms ($b = 25.2\text{x}10^{-15}$ m) is an order of magnitude larger than any other scattering length in the system, and as polyaniline/plastdopant system contains a large fraction of hydrogen atoms, only hydrogen incoherent scattering is considered here.

Time-space correlation function and incoherent scattering

In an isotropic medium, time-space correlation function is defined as:

$$G(r,t) = \langle n(0,0)n(R,t) \rangle \qquad \text{(C.3.1)}$$

Where: $n(R,t) = \sum_{i}^{N} \delta(R - R_i(t))$ presents coordinates of all nuclei at time t.

Time-space correlation function has self and distinct part:

$$G(R,t) = G_S(R,t) + G_D(R,t) \qquad \text{(C.3.2)}$$

If at time t_1=0 a particle was at position R_1=0, self part $G_S(R,t)$ gives a probability to find the same particle around position R at time t, and distinct part $G_D(R,t)$ gives a probability to find another particle around position R at time t. Self part of time-space correlation function permits to study the motions of individual particles. The space Fourier transform of self correlation function $G_S(R,t)$ gives an incoherent intermediate scattering function *I(Q,t)* (see eq.C.3.4) The incoherent scattering technique is the best one for the dynamics studies because it gives a direct access to the self correlation function.

Scattering functions

The incoherent dynamic structure factor $\boldsymbol{S}(\boldsymbol{Q}, \omega)$ is the time Fourier transform of the intermediate scattering function, $I(\boldsymbol{Q}, t)$,

$$S(\boldsymbol{Q},\omega) = \frac{1}{2\pi} \int_{-\infty}^{+\infty} I(\boldsymbol{Q},t) \exp(-i\omega t) dt \qquad \text{(C.3.3)}$$

which itself is defined as

$$I(\boldsymbol{Q},t) = \sum_i b_i^2 \left\langle e^{i\boldsymbol{Q}.\boldsymbol{R}_i(t)} e^{-i\boldsymbol{Q}.\boldsymbol{R}_i(0)} \right\rangle \qquad \text{(C.3.4)}$$

The sum over *i* runs over the scattering nuclei in the sample and the thermal average denoted by the brackets holds for the vector positions of these nuclei, $\boldsymbol{R}_i$(t) and $\boldsymbol{R}_i$(0), at time *t* and at time 0, respectively. The hydrogen atoms of the system experience two types of molecular motions: rotations (reorientations of whole molecule or of chemical groups) and vibrations (phonons and internal vibrations).

The interpretation of the data is usually simplified by making the hypothesis that the different kinds of contributions to motions are essentially not coupled between them, because of their respective time-scales and amplitudes. Vibrational motions of a molecule occur on the 10^{-13}-10^{-14} s time-scale and may be considered as independent from diffusive-type rotations which are much slower (10^{-9}-10^{-12} s). That is mathematically expressed by writing the total scattering function as the convolution product of the respective scattering functions :

$$S(\boldsymbol{Q},\omega) = S^{rot}(\boldsymbol{Q},\omega) \otimes S^{vib}(\boldsymbol{Q},\omega) \tag{C.3.5}$$

In the quasielastic region of the spectrum (which corresponds to energy transfers smaller than about 2 meV), the expression above takes the form

$$S(\boldsymbol{Q},\omega) = \mathrm{e}^{-<u^2>Q^2/3}\left[S^{rot}(\boldsymbol{Q},\omega) + S^{inel}(\boldsymbol{Q},\omega)\right] \tag{C.3.6}$$

The Debye-Waller term $\exp[-<u^2>Q^2/3]$ is a scaling factor that describes the attenuation effect due to lattice phonons or molecule vibrational modes of lowest energy. $<u^2>$ stands for the mean square amplitude of vibration. These motions also introduce the inelastic term $S^{inel}(\boldsymbol{Q}, \omega)$ which actually contributes only little to the total scattering in the quasielastic region in the form of a slowly varying function of energy which is most often taken into account as an energy-independent background

$$S^{inel}(\boldsymbol{Q},\omega) = S^{inel}(\boldsymbol{Q}) \tag{C.3.7}$$

Correlations between the positions of the same scatterer at initial time $\boldsymbol{R}(0)$ and at a later time $\boldsymbol{R}(t)$ diminish as a function of time and tend to disappear completely at infinite times. Consequently the thermal average occurring in the intermediate scattering function (2) can be evaluated by considering separately the initial and final positions of the scattering nucleus. Hence, from (C.2.2) and for a single scatterer

$$I(\boldsymbol{Q},\infty) = \left\langle e^{i\boldsymbol{Q}.\boldsymbol{R}(\infty)} \right\rangle \left\langle e^{-i\boldsymbol{Q}.\boldsymbol{R}(0)} \right\rangle \tag{C.3.8}$$

The system being in thermal equilibrium, the distribution of the scattering nuclei is the same at both times, so that

$$I(\mathbf{Q},\infty) = \left|\left\langle e^{i\mathbf{Q}.\mathbf{R}(\infty)} \right\rangle\right|^2 = \left|\left\langle e^{-i\mathbf{Q}.\mathbf{R}(0)} \right\rangle\right|^2 \tag{C.3.9}$$

In the case of a fully isotropic sample (liquid), at infinite times, the scattering nucleus can access any coordinate in space, independently of its initial position. Thus the average $I(\boldsymbol{Q}, \infty)$ vanishes. Conversely in the case of whole molecule reorientations about centre of mass or of internal reorientations of chemical groups, the scatterers remain confined within a certain volume of space. Therefore at infinite times, the probability of finding the scatterer within the volume is equal to unity. $I(\boldsymbol{Q}, \infty)$ is directly linked to the Fourier transform of the spatial distribution of the scattering centres so it does not vanish and its variation with the

momentum transfer, $\boldsymbol{Q}$, provides information about the size and the shape of the restrictive volume.

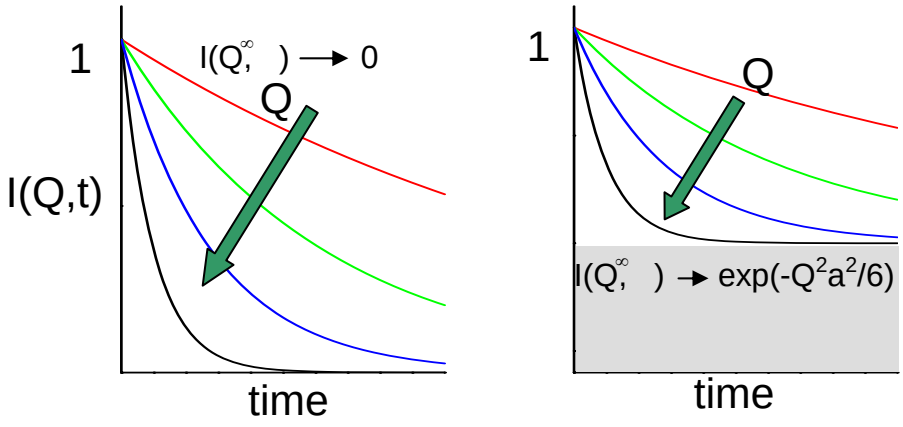

Fig. C.3.1 Intermediate scattering function

At any time, it is possible to separate formally $I(\boldsymbol{Q}, t)$ into its time-independent part, $I(\boldsymbol{Q}, \infty)$ and its time-dependent part $I(\boldsymbol{Q}, t)$ - $I(\boldsymbol{Q}, \infty)$. The presence of a constant term gives rise by Fourier transform to a purely elastic component in the scattering function, hence

$$S^{rot}(\boldsymbol{Q},\omega) = I(\boldsymbol{Q},\infty).\delta(\omega) + \frac{1}{2\pi}\int_{-\infty}^{\infty}\left[I(\boldsymbol{Q},t) - I(\boldsymbol{Q},\infty)\right]exp(-i\omega t)dt \qquad \text{(C.3.10)}$$

In the most simple case $I(\boldsymbol{Q}, t)$ decreases exponentially with time from its initial value $I(\boldsymbol{Q}, 0)$ with a single characteristic time, τ,

$$I(\boldsymbol{Q},t) = \left[I(\boldsymbol{Q},0) - I(\boldsymbol{Q},\infty)\right].exp\left(-\frac{t}{\tau}\right) + I(\boldsymbol{Q},\infty) \qquad \text{(C.3.11)}$$

and the expression of the scattering function involves a quasi-elastic component with a Lorentzian shape underlying a purely elastic component. Its half width at half maximum (hwhm), in energy unit is equal to $1/\tau$.

$$S^{rot}(\boldsymbol{Q},\omega) = I(\boldsymbol{Q},\infty).\delta(\omega) + \left[I(\boldsymbol{Q},0) - I(\boldsymbol{Q},\infty)\right].\frac{1}{\pi}.\frac{\tau}{1+(\omega\tau)^2} \qquad \text{(C.3.12)}$$

In the general case of more complicated reorientations or of several scattering atoms having different dynamics, as far as the movements remain diffusive in nature, the quasi-elastic component is expressed as a sum of several Lorentzian functions whose widths and relative

contributions depend on the precise motions of individual atoms. In all cases the width of the quasi-elastic term is directly related to the characteristic times associated to the relevant motions of the scattering nuclei. The overall importance of the purely elastic component is directly linked to the Fourier transform of the spatial equilibrium distribution of the scattering centers. It has the dimension of a structure factor and is usually denoted as Elastic Incoherent Structure Factor (EISF).

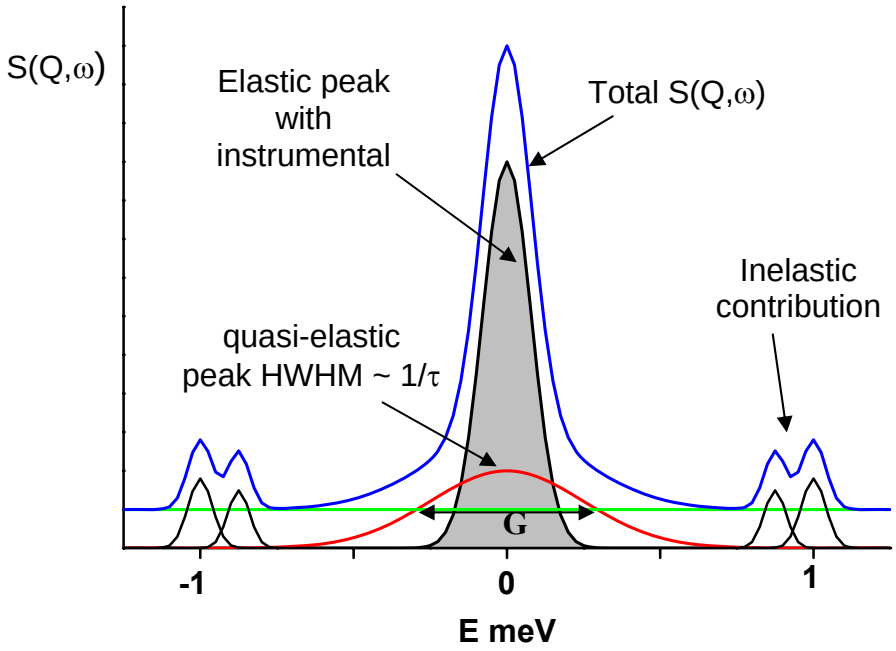

Fig. C.3.2 Dynamic structure factor

The energy resolution of any spectrometer is finite. Thus the elastic peak is never infinitely narrow but rather exhibits some shape characteristic of the instrument, generally triangular or Gaussian. The full width at half maximum (fwhm) of this function determines the lower limit of the observable energy transfers accessible to the spectrometer. It corresponds to the slowest observable movements. Motions that occur on a too long time-scale give rise to very small energy transfers, which yield a quasi-elastic broadening too weak to be observed accurately. For instance typical energy width of the resolution of a backscattering spectrometer like IN10 (Institut Laue-Langevin (ILL), Grenoble, France, see experimental section) is equal to about 1 μeV (fwhm). Assuming that a quasielastic broadening can be measured when its hwhm is at least 1/10 of this value, this instrument allows to investigate motions with a characteristic time faster than 6.6 10^{-9} s. The upper limit in energy accessible to a spectrometer determines the fastest motions which can be observed.

The spectrometer above-mentioned permits to investigate energy exchanges within the limits ± 15 μeV. That is corresponding to motions occurring on a time-scale of about 4.4 10^{-11}s. A faster dynamics of the scattering nuclei results in a wide broadening the major part of which is located outside the instrument energy limits. Within the instrument energy window quasi-elastic scattering appears as a nearly flat background and the determination of its hwhm is very difficult. This point is particularly important in the interpretation of the data obtained by the so-called "fixed-window" technique. The time of flight spectrometer IN6 (ILL, see experimental section) exhibits an energy resolution of the order of 80 -150 μeV (fwhm). Its longest limit for dynamical phenomena is thus 2 10^{-11} -4.4 10^{-11}s. But it allows to observe quasi-elastic energy transfers up to about 2-4 meV (actually this limit is given by the discrimination between the quasi-elastic region and inelastic vibrational part of the spectra). Thus dynamical processes with short characteristic times (3.3 10^{-13} -1.6 10^{-13}s) can be investigated. With IN6, by considering the edge of the experimental energy spectrum, it is possible to obtain the purely inelastic spectrum for low energy vibrational modes (1<E<50 meV). In fact, the quantity directly visualized in these experiments corresponds to the function directly deduced from the inelastic law as:

$$p(\bar{\alpha}) = \beta\hbar\omega\left[\exp(-\beta\hbar\omega) - 1\right]\frac{S^{inel}(\boldsymbol{Q},\omega)}{\bar{\alpha}} \qquad \text{(C.3.13)}$$

with $\bar{\alpha} = \frac{\hbar^2 Q^2}{2mk_B T}$ where the usual quantity $\beta = \frac{1}{k_B T}$ has been introduced. By simple extrapolation (13) provides a determination of the vibrational frequencies distribution $G(\omega)$.

$$\lim_{Q^2 \to 0} p(\bar{\alpha}) = G(\omega) \qquad \text{(C.3.14)}$$

The analysis of the dynamical behavior of a system over a wide temperature range generally requires using several spectrometers having different characteristics each of them being adapted to a particular interval of temperature. But when passing from an instrument to another and increasing the temperature, great care has to be taken to check whether it is actually the same motion which is investigated or if a new kind of movement has appeared.

C.3.2 Time of flight spectrometers

Time-of-flight (TOF) is a general method for finding the energy of a neutron by measuring the time it takes to fly between two points. High-energy neutrons fly fast whilst low-energy or "cold" neutrons are much slower. In the primary part of the spectrometer, i.e. before the sample a monochromator crystal is used to select a continuous beam of neutrons with the same velocity from a beam of neutrons with mixed velocities (Bragg's Law). This monochromatic beam is then pulsed with a chopper. At the sample some neutrons gain or loose energy and they are scattered with new velocities in many directions. We know the time at which the neutrons hit the sample and we wish to know the time of their arrival at the detectors. There are far too many neutrons to measure them individually so we count the number of neutrons arriving within different time periods. This gives us a histogram of the number of neutrons arriving at the detectors within a given period at different times the time-of-flight spectrum. We know that all neutrons hit the sample with equal velocity at the same time so we can calculate how the energy was absorbed or released by various atomic motions in the sample.

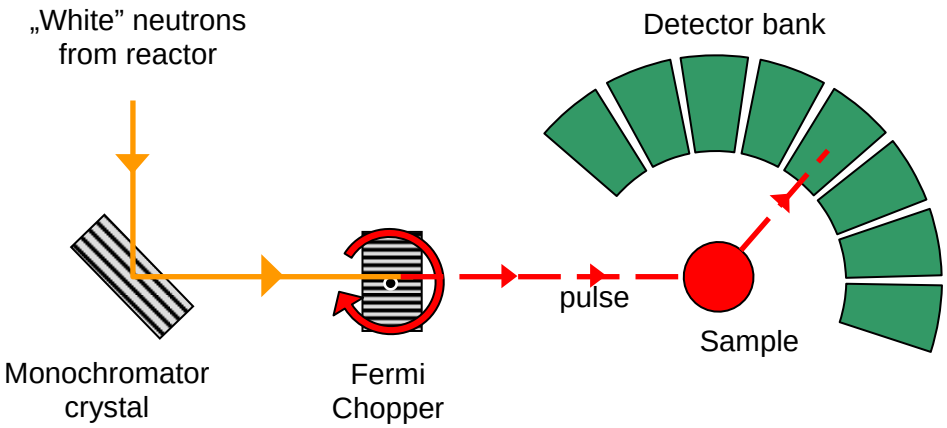

Fig. C.3.3 Schematic view of time-of flight (TOF) spectrometer

C.3.3 Backscattering spectrometers

The basic idea of backscattering spectroscopy (BS) is to use single crystal diffraction of neutrons with Bragg angles near 90 degrees for monochromatisation and energy analysis. In this way one achieves a very high energy resolution which is better than 1 μeV for cold neutrons. The energy of the incident beam is modulated with Doppler motion of a monochromator crystal. This operation permits to investigate energy exchanges within the limits ± 15 μeV. Backscattering technique can operate over a very wide range of momentum transfer simultaneously and potentially can access a time-range between 0.01μs and 100ps.

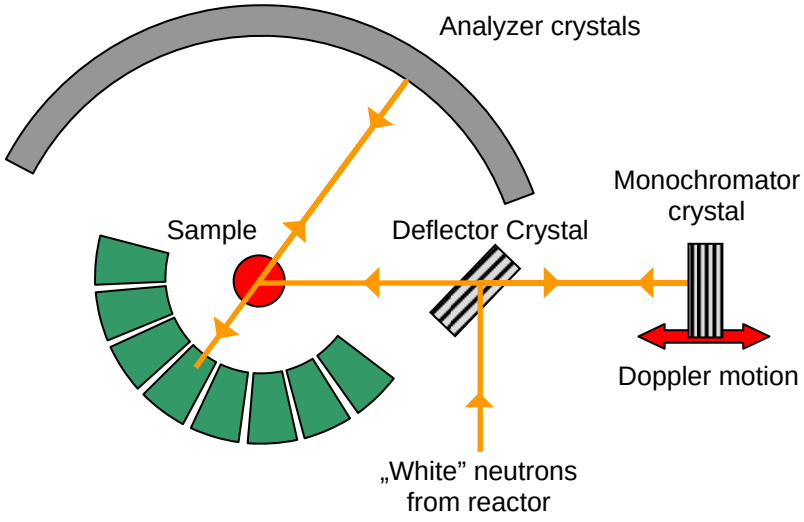

Fig.C.3.4 Schematic view of backscattering (BS) spectrometer

C.3.4 Quasi-elastic neutron scattering experiments

ILL experiments

We first performed incoherent QENS experiments at the high-flux reactor of the Institut Laue Langevin (ILL) (Grenoble, France) with the time focusing time-of-flight spectrometer IN6 [63], with an incident neutron wavelength $\lambda = 5.12$ Å. Spectra were simultaneously recorded at 89 angles, ranging from 14.7° to 113.5°. The experiments were carried out, with the sample set at $\alpha = 135°$ with respect to the incident beam. In such transmission geometry the energy resolution varies from 77 μeV at small scattering angles to

about 120 μeV for the largest values. It was measured with a vanadium plate, 1 mm in thickness, which also served for calibration of the detectors efficiencies. The obtained time-of-flight spectra, after the usual corrections for absorption and scattering from the container were transformed into $S(\theta,\omega)$ using the program INX of the ILL library. Still at ILL another series of experiments was performed with the high resolution backscattering spectrometer IN16.(for $PANI_{0.5}$DDoESSA only) with a wavelength of 6.28Å and an energy resolution of 0.9μeV (FWHM). Data were recorded at 2θ scattering angles ranging from 10.95° to 135.5° and grouped into 12 spectra. The detector efficiencies were calibrated from the measurement of a vanadium standard and the energy spectra were obtained by using the SQW program from the ILL library.

LLB experiments

Intermediate resolution measurements were carried out at the Orphée reactor of Laboratoire Léon Brillouin (LLB) (Saclay-France) by using the time-of-flight spectrometer MIBEMOL. Measurements were performed using an incident wavelenght of 7.5Å. 68 spectra were recorded simultaneously for different scattering angles ranging from 25.5° to 138.6°. The films were held in a flat aluminum container 0.2 mm in thickness. After removing the data affected by shadowing of the sample holder itself, we grouped the data into five spectra ranging in a momentum transfer (**Q**) interval extending from 0.370 to 1.568 $Å^{-1}$.The energy resolution measured with a 0.2 mm thick vanadium plate was found to be 42μeV (FWHM) while the same measurement allowed us to calibrate the detector efficiencies. All the raw data were corrected for absorption, scattering from container and transformed in energy by using programs of the LLB Library.

RAL experiments

In order to be able to cover continuously more than three orders of magnitude in time, we have also investigated the samples with the time-of-flight inverted geometry crystal analyzer spectrometer IRIS at the pulsed spallation neutron source ISIS at the Rutherford Appleton Laboratory (Chilton – UK). We used the spectrometer in the so-called asymmetric HOPG 002 analyzers configuration which provided an energy resolution of 15 μeV (FWHM). The data were grouped into 9 spectra covering a Q range from 0.464 to 1.834 $Å^{-1}$. We used

the RAL library for treating all the data. In particular we used the fast Fourier Transform code elaborated by H.S. Howells [64] for evaluating the intermediate scattering function I(**Q**,t) from the scattering functions S(**Q**,ω). This program has also been adapted in order to obtain I(**Q**,t) from the measurements performed on the three other above mentioned spectrometers.

All the experiments were made as a function of the temperature in between 150 and 340 K while the energy resolution was always evaluated from a low temperature (typically 3-4 K) measurement of the sample itself.

C.4 Molecular dynamics numerical simulations

C.4.1 Force field based molecular dynamics simulation (MD)

The force field based molecular dynamics simulation method is based on Newton's second law or the equation of motion [65]:

$$\vec{F}_i = -\nabla_i V = m_i \frac{d^2 \vec{r}_i}{dt^2} \qquad \text{(C.4.1)}$$

Where F_i is the force exerted on the atom i with a mass m_i and d^2r_i/dt^2 is acceleration of this atom. From knowledge of the force on each atom or gradient of the potential energy function V, it is possible to determine the acceleration of each atom in the system. Integration of the equations of motion then yields a trajectory that describes the positions, velocities and accelerations of the particles as they vary with time. From this trajectory, the average values of properties can be determined. The method is deterministic; once the positions and velocities of each atom are known, the state of the system can be predicted at any time in the future or the past. Several various integration algorithms are used for finding trajectories from Newton's equation. All the integration algorithms assume positions, velocities and accelerations of atoms can be approximated by a Taylor series. Positions at time t+Δt where Δt is integration step:

$$\vec{r}_i(t+\Delta t) = \vec{r}_i(t) + \frac{d\vec{r}_i}{dt}\Delta t + \frac{1}{2}\frac{d^2\vec{r}_i}{dt^2}\Delta t^2 + \ldots \qquad \text{(C.4.2)}$$

And at time t-Δt :

$$\vec{r}_i(t-\Delta t) = \vec{r}_i(t) - \frac{d\vec{r}_i}{dt}\Delta t + \frac{1}{2}\frac{d^2\vec{r}_i}{dt^2}\Delta t^2 + \ldots \qquad \text{(C.4.3)}$$

Summing these two equations lead to the expression of Verlet algorithm:

$$\vec{r}_i(t-\Delta t) = 2\vec{r}_i(t) - \vec{r}_i(t+\Delta t) + \frac{d^2\vec{r}_i}{dt^2}\Delta t^2 \qquad \text{(C.4.4)}$$

The Verlet algorithm uses positions and accelerations at time *t* and the positions from time (t-Δt) to calculate new positions at time (t+Δt). The Verlet algorithm uses no explicit velocities. The advantages of the Verlet algorithm are, *i)* it is straightforward, and *ii)* the storage requirements are modest. The disadvantage is that the algorithm is of moderate precision. Therefore, to calculate a trajectory, one only needs the initial positions of the atoms, an initial distribution of velocities and the acceleration, which is determined by the gradient of the potential energy function. The initial distribution of velocities is determined from random distribution with magnitude conforming to the required temperature of simulation. Random distribution must be corrected to obtain overall momentum equal to 0.

$$\vec{p} = \sum_{i=1}^{N} \vec{v}_i m_i = 0 \qquad \text{(C.4.5)}$$

Temperature is a state variable that specifies the thermodynamic state of the system and is also an important concept in dynamics simulations. This macroscopic quantity is related to the microscopic description of simulations through the kinetic energy, which is calculated from the atomic velocities. The temperature and the distribution of atomic velocities in a system are related through the Maxwell-Boltzmann equation:

$$f(v)dv = \left(\frac{m_i}{2\pi k_B T}\right)^{\frac{3}{2}} \exp\left(-\frac{mv^2}{k_B T}\right) 4\pi v^2 dv \qquad \text{(C.4.6)}$$

This formula expresses the probability $f(v)$ that a molecule of mass m has a velocity of v when it is at temperature T. The thermodynamic temperature can be calculated from the atoms velocities using the relation:

$$T = \frac{2}{3Nk_B}\left\langle \sum_{i=1}^{N} \frac{{p_i}^2}{2m_i} \right\rangle \qquad \text{(C.4.6bis)}$$

Where N is the number of atoms in the system.

Statistical ensembles

Most of natural phenomena occur under exposure to external pressure or heat exchange, which must be taken into account in molecular dynamics simulations. Depending on what kind of thermodynamic properties we are interested in, it is possible to choose one of four methods for controlling the temperature and pressure during the simulation [66].

Four possible thermodynamical ensembles are:

- Microcanonical ensemble (NVE) : The thermodynamic state characterized by a fixed number of atoms, N, a fixed volume, V, and a fixed energy, E. This corresponds to an isolated system.
- Canonical ensemble (NVT): This is a collection of all systems whose thermodynamic state is characterized by a fixed number of atoms, N, a fixed volume, V, and a fixed temperature, T.
- Isobaric-isothermal ensemble (NPT): This ensemble is characterized by a fixed number of atoms, N, a fixed pressure, P, and a fixed temperature, T.
- Grand canonical ensemble (μVT): The thermodynamic state for this ensemble is characterized by a fixed chemical potential, μ, a fixed volume, V, and a fixed temperature, T.

NPT is the ensemble of choice when the correct pressure, volume, and densities are important in the simulation. This ensemble is very useful during equilibration and structure stabilization. NVT constant-volume and temperature ensemble is useful for equilibrated system to avoid artificial fluctuation of parameters like periodic box dimensions occurring during the simulation especially for small systems.

C.4.2 Force field (potential energy surface) parameterization

That is very important for Molecular Dynamics Simulations (MDS) to describe correctly the all inter atomic interactions in order to have good potential surface with parameters well reproducing the force field. All molecular dynamics simulations were performed using

condensed-phase *ab-initio* optimized second-generation force field COMPASS (condensed-phase optimized molecular potentials for atomistic simulation studies)[67]. The functional forms of this force field are of the consistent force field type (CFF). Bonded terms were derived from Hartree-Fock calculations (HF), non-bonded parameters were initially transferred from the polymer consistent force field and optimized using MD simulations of condensed-phase properties. The functional forms used in this force field (eq.C.4.7) can be divided into two categories, valence terms including diagonal and off-diagonal cross-coupling terms and non-bonded interaction terms.

$$
\begin{aligned}
&E_{total} = \sum_{b}\left[k_2(b-b_0)^2 + k_3(b-b_0)^3 + k_4(b-b_0)^4\right] + \\
&\sum_{\theta}\left[k_2(\theta-\theta_0)^2 + k_3(\theta-\theta_0)^3 + k_4(\theta-\theta_0)^4\right] + \\
&\sum_{\phi}\left[k_1(1-\cos\phi) + k_2(1-\cos 2\phi) + k_3(1-\cos 3\phi)\right] + \\
&\sum_{\chi} k_2\chi^2 + \sum_{b,b^{\copyright}} k(b-b_0)(b^{'}-b_0^{'}) + \sum_{b,\theta} k(b-b_0)(\theta-\theta_0) + \\
&\sum_{b,\phi} k(b-b_0)\left[k_1\cos\phi + k_2\cos 2\phi + k_3\cos 3\phi\right] + \\
&\sum_{\theta,\phi} k(\theta-\theta_0)\left[k_1\cos\phi + k_2\cos 2\phi + k_3\cos 3\phi\right] + \\
&\sum_{\theta,\theta^{\copyright}} k(\theta-\theta_0)(\theta^{o}-\theta_0^{o}) + \sum_{\theta,\theta^{\copyright},\phi} k(\theta-\theta_0)(\theta^{o}-\theta_0^{o})\cos\phi + \\
&\sum_{ij}\frac{q_i q_j}{r_{ij}} + \sum_{ij}\varepsilon_{ij}\left[2\left(\frac{r_{ij}^{o}}{r_{ij}}\right)^9 - 3\left(\frac{r_{ij}^{o}}{r_{ij}}\right)^6\right]
\end{aligned}
\qquad \text{(C.4.7)}
$$

The valence term represents internal coordinates of bond (b) (bond stretching), angle (θ) (bond angle), torsion angle (χ), and cross-coupling terms include combinations of internal coordinates, bond-bond, bond-angle, bond-torsion angle which are the most frequently used terms. The nonbond interactions, which include van der Waals interactions (vdW) represented by Lennard-Jones function LJ-9-6 and Coulombic function for electrostatic interaction are used for interaction between pairs of atoms that are separated by two or more intervening atoms or those that belong to different molecules [68].

Bonded interaction (bonded terms)

Bonded valence terms are divided into three main groups: bonds, angles and rotation (torsion) angles and additional cross-coupling terms

$$E_{valence} = \underbrace{E_{bond-strech} + E_{bond-angle} + E_{bond-torsion}}_{diagonal} + E_{cross-coupling-terms} \quad \text{(C.4.8)}$$

Bonds stretching

This term is a harmonic potential representing the interaction between atomic pairs where atoms are separated by one covalent bond. This is the approximation to the energy of a bond as a function of displacement from the ideal bond length, b_0. The force constant, K_b, determines the strength of the bond. Both ideal bond lengths b_0 and force constants K_b are specific for each pair of bound atoms.

$$E_{bond-stretch} = \sum_{1,2\,pairs} K_b (b - b_0)^2$$

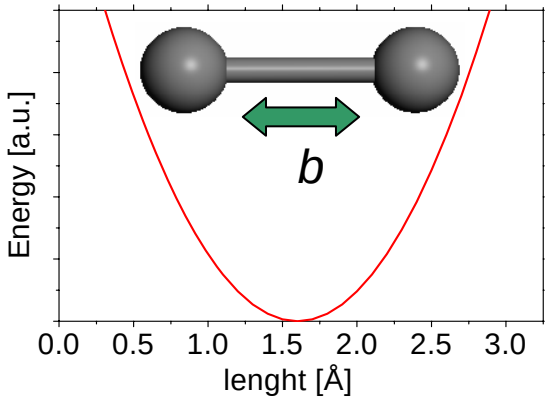

Bond angle

This term is associated with alteration of bond angles theta from ideal values θ_0 , which is also represented by a harmonic potential. Values of θ_0 and K_θ depend on chemical type of atoms constituting the angle.

$$E_{bond-angle} = \sum_{1,2\,pairs} K_\theta (\theta - \theta_0)^2$$

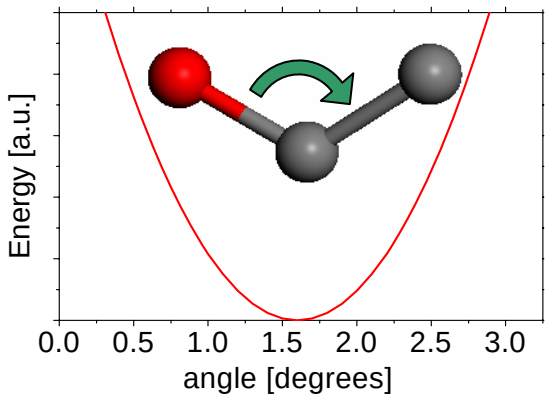

Rotation (torsion) angle

This term represents the torsion angle potential function which models the presence of steric barriers between atoms separated by 3 covalent bonds (1,4 pairs). The motion associated with this term is a rotation, described by a dihedral angle and coefficient of symmetry *n=1,2,3*), around the middle bond. This potential is assumed to be periodic and is often expressed as a cosine function.

$$E_{bond-torsion} = \sum_{1,4\,pairs} K_\phi (1 - \cos(n\phi))$$

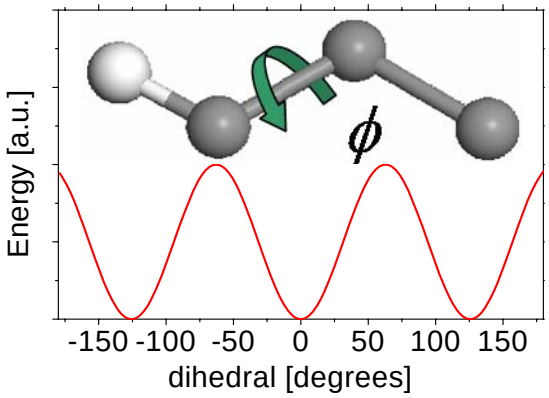

In earlier so called first generation force fields, the diagonal energy functions were the simplest possible, containing only one type of term, the quadratic or harmonic term. Second generation force field like COMPASS extends the diagonal energy expression by adding cubic and quartic terms:

$$\sum_b \left[k_2 (b - b_0)^2 + k_3 (b - b_0)^3 + k_4 (b - b_0)^4 \right] \qquad \text{(C.4.9)}$$

Cross-coupling terms

Bond-bond term: $\sum_{b,b^{\copyright}} k(b-b_0)(b^{'}-b_0{}^{'})$

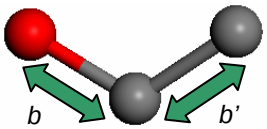

Bond-angle term: $\sum_{b,\theta} k(b-b_0)(\theta-\theta_0)$

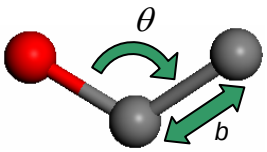

Angle-angle term: $\sum_{\theta,\theta^{\copyright}} k(\theta-\theta_0)(\theta^{o}-\theta_0{}^{o})$

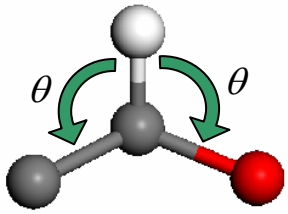

Angle-torsion term:

$\sum_{\theta,\phi} k(\theta-\theta_0)[k_1\cos\phi + k_2\cos 2\phi + k_3\cos 3\phi]$

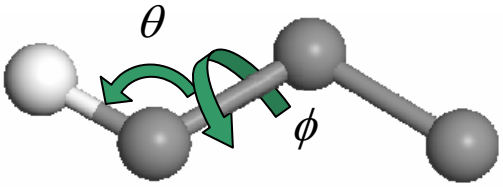

Improper out of plane term: $E = \sum_{\chi} k_2 \chi^2$

Non-bonded interactions (non-bonded terms)

The most time consuming part of a molecular dynamics simulation is the calculation of the non-bonded terms in the potential energy function, e.g., the electrostatic and Van der Waals forces.

$$E_{non-bonded} = \sum_{ij} \frac{q_i q_j}{r_{ij}} + \sum_{ij} \varepsilon_{ij} \left[2\left(\frac{r_{ij}^{o}}{r_{ij}}\right)^{9} - 3\left(\frac{r_{ij}^{o}}{r_{ij}}\right)^{6} \right] \qquad \text{(C.4.10)}$$

Electrostatic Van der Waals

To speed up the computation, the interactions between two atoms separated by a distance greater than a pre-defined distance, the cutoff distance, are ignored. Several different ways to terminate the interaction between two atoms have been developed over the years; some work better than others.

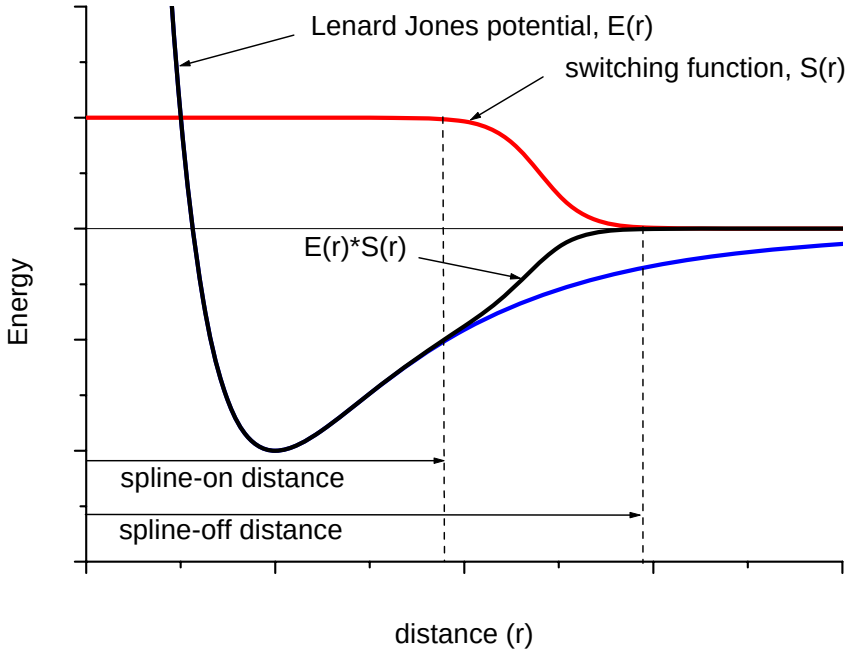

Fig. C.4.1 Lennard Jones Potential Energy profile and its modification due to the effect of the spline operation.

Van der Waals Interactions

Van der Waals interactions are parameterized by Lennard-Jones (L-J) '6-9' potentials of the form

$$E_{VdW} = \sum_{ij} \varepsilon_{ij} \left[2\left(\frac{r_{ij}^{o}}{r_{ij}}\right)^{9} - 3\left(\frac{r_{ij}^{o}}{r_{ij}}\right)^{6} \right] \qquad \text{(C.4.11)}$$

The (L-J) '6-9' parameters (ε and r^{o}) are given for like atom pairs and tabulated. For unlike atom pairs, a 6th order combination law (combination rules) is used to calculate off-diagonal parameters:

$$r_{ij}^{o} = \left(\frac{(r_i^o)^6 + (r_j^o)^6}{2} \right)^{\frac{1}{6}}$$
$$\varepsilon_{ij} = 2\sqrt{\varepsilon_i \varepsilon_j} \left(\frac{(r_i^o)^3 (r_j^o)^3}{(r_i^o)^6 (r_j^o)^6} \right) \qquad \text{(C.4.12)}$$

C.4.3 Charge equilibration techniques

The force field based molecular dynamics simulations need effective method for determining the electrostatic energies. The accurate prediction of charge distribution within the molecules is essential for good description of electrostatic interactions. Looking from this point of view the polyaniline chain-counterion system may be characterized with two aspects that strongly determined it structural and dynamical properties. First important aspect is that due to the protonation reaction the polyaniline chain-counterion interaction has a strongly ionic character. Negatively charged counterion heads interact with positively charged polyaniline chains. Another important aspect is the problem of delocalization of charge along the polyaniline backbone due to the presence of conjugated bond system and between chains due to overlapping of π-orbitals of neighbor chains. That delocalization of charges is quite difficult or impossible to modelize properly in force field based semi empirical MD simulations. The fixed charges approach may be only useful and not to far from real situation if we consider relatively uniform distribution of positive and negative charges along polyaniline chains. In that situation calculated charges may be treated as the time average. The ionic character of polyaniline chain-counterion interactions requires very careful treatment of charge prediction procedures.

The electrostatic interaction is represented using atomic partial charges. To make the charge parameters transferable, bond increments δ_{ij} which represent the charge separation between two valence-bonded atoms i and j, are used in the force filed as parameters. For atom i, the partial charge is the sum of all charge bond increments δ_{ij}:

$$q_i = \sum_j \delta_{ij} \qquad \text{(C.4.13)}$$

Where *j* represents all atoms, that are valence-bonded to atom *i.* This method leads to the artificial situation when partial charge on a given atom depends only on the types and number

of the neighbor valence-bonded atoms. All the charges are fixed and independent to the charges on the neighbor molecules. The MD simulations of the ionic compounds mainly based on electrostatic interaction become inconsistent. Dynamic simulation using fixed charge cannot represent the relaxation of charge distribution that depends upon changing molecular structure. The solution is to use semi-empirical based on electronegativity rules charge equilibration approach (Qeq) proposed by Rappé and Goddard [69] or estimate partial charges using density functional theory (DFT) based calculations. Using DFT based calculations partial charges are optimized to reproduce calculated electrostatic potential (ESP) or using the Mulliken population analysis. These methods let us predict charge distribution that depends upon molecular geometry.

Charge equilibration (Rappé Goddard)

In order to estimate the equilibrium charges in molecule, we consider how the energy of an isolated atom changes as a function of charge. Energy of atom A:

$$E_A(q) = E_{A_0} + q_A\left(\frac{\partial E}{\partial q}\right)_{A_0} + \frac{1}{2}{q_A}^2\left(\frac{\partial^2 E}{\partial q^2}\right)_{A_0} + \ldots \qquad \text{(C.4.14)}$$

Including only terms trough second order lead to:

$$\begin{aligned} E_A(+1) &= E_{A_0} + \left(\frac{\partial E}{\partial q}\right)_{A_0} + \frac{1}{2}\left(\frac{\partial^2 E}{\partial q^2}\right)_{A_0} \\ E_A(0) &= E_{A_0} \\ E_A(-1) &= E_{A_0} - \left(\frac{\partial E}{\partial q}\right)_{A_0} + \frac{1}{2}\left(\frac{\partial^2 E}{\partial q^2}\right)_{A_0} \end{aligned} \qquad \text{(C.4.15)}$$

That leads to:

$$\left(\frac{\partial E}{\partial q}\right)_{A_0} = \frac{1}{2}(IP + EA) = \chi_A^0 \quad ; \quad \left(\frac{\partial^2 E}{\partial q^2}\right)_{A_0} = IP - EA = J_{AA}^o \qquad \text{(C.4.16)}$$

IP and EA denote the ionization potential and electron affinity, χ_A is referred to as electronegativity. To understand the physical significance of second-derivative quantity $\partial^2 E/\partial q^2$, consider the simple case of a neutral atom with a simply occupied orbital ϕ_A. J^o_{AA} is the Coulomb repulsion between two electrons in the $\phi_A$orbital (the self-Coulomb integral).
Using (C.3.14) and (C.3.16) leads to:

$$E_A(q) = E_{A_0} + \chi_A^0 q_A + \frac{1}{2} J_{AA}^0 {q_A}^2 \qquad \text{(C.4.17)}$$

χ_A^0, J^o_{AA} can be derived from atomic data however they must be corrected for exchange interactions present in atoms but absent in molecules.

In order to calculate the optimum charge distribution, we need to evaluate the interatomic electrostatic energy. This leads to a total electrostatic energy:

$$\begin{aligned} E(q_1 ... q_N) &= \sum_A (E_{A0} + \chi_A^0 q_A + \frac{1}{2} q_A^2 J_{AA}^0) + \sum_{A<B} q_A q_B J_{AB} \quad or \\ E(q_1 ... q_N) &= \sum_A (E_{A0} + \chi_A^0 q_A) + \frac{1}{2} \sum_{A,B} q_A q_B J_{AB} \end{aligned} \qquad \text{(C.4.18)}$$

Where J_{AB} is the Coulomb interaction between unit charges on centers A and B (depends on the distance between A and B)

Taking the derivative of E with respect to q leads to an atomic-scale chemical potential:

$$\chi_A(q_1 ... q_N) = \frac{\partial E}{\partial q_A} = \chi_A^0 + \sum_B J_{AB} q_B \quad or \quad \chi_A(q_1 ... q_N) = \chi_A^0 + J_{AA}^0 q_A + \sum_{B \neq A} J_{AB} q_B \qquad \text{(C.4.19)}$$

Now χ_A^0 is a function of charges on all the atoms. For equilibrium, we require that the chemical potentials be equal, leading to *N-1* conditions:

$$\chi_1 = \chi_2 = ... = \chi_N \quad ; \quad q_{total} = \sum_{i=1}^{N} q_i \qquad \text{(C.4.20)}$$

Adding the condition on total charge leads to *N* simultaneous equations for the equilibrium self-consistent charges that are solved once for a given structure.

To predict more realistic partial charges for a given structure is necessary to introduce some shielding corrections. The Coulomb potential J_{AB} between unit charges on centers A and B is inversely proportional to separation distance R for large separations. However for small separation distance where charge distributions overlap, the simple Coulomb law is no longer valid. The shielding of charge distributions may be expressed as the Coulomb integral between atomic densities obtained from accurate Hartree-Fock (HF) or local-density calculations for a given system. More accurate the DFT based calculations and the Mulliken population analysis of our systems give partial charges that differ by a multiplicative constant of the charges estimated with Qeq approach. This difference may be due to fact that all the parameters used in charge equilibration procedure are optimized only for a series of typical organic and inorganic compounds. That is why they are not ideally optimized exactly for our more complex systems. Additionally, for much distorted systems, application of Qeq approach may give not realistic, unphysical results.

C.4.4 Structure stabilization, MD simulations protocols

Small simulation box

Structure Stabilization

A triclinic periodic box of plast-doped polyaniline (PANI-DB3EPSA) consisting of 4 poly(aniline) chains and 8 counter-ion molecules was constructed. Along the polymer chain direction (c-direction) the box dimension is determined by the smallest poly(aniline) repeat unit (four phenyl rings as aniline monomers). 8 doping molecules per 16 aniline monomers units gives the correct doping level equal to 0.5. The periodic box dimension along b-direction is fixed by a single lamellar distance with one layer of poly(aniline) and two layers of counter-ions molecules. Poly(aniline) chains are stacked along a-direction. Periodic box dimension in this direction is determined by a characteristic intermolecular distance of stacked phenyls in poly(aniline) chains i.e. ~3.5Å multiplied by four (4 PANI chains). Poly(aniline) and doping molecules were built and geometrically optimized individually before to construct the "crystal". This model was used as a starting configuration for molecular dynamic simulations. It is shown in the figure C.4.2

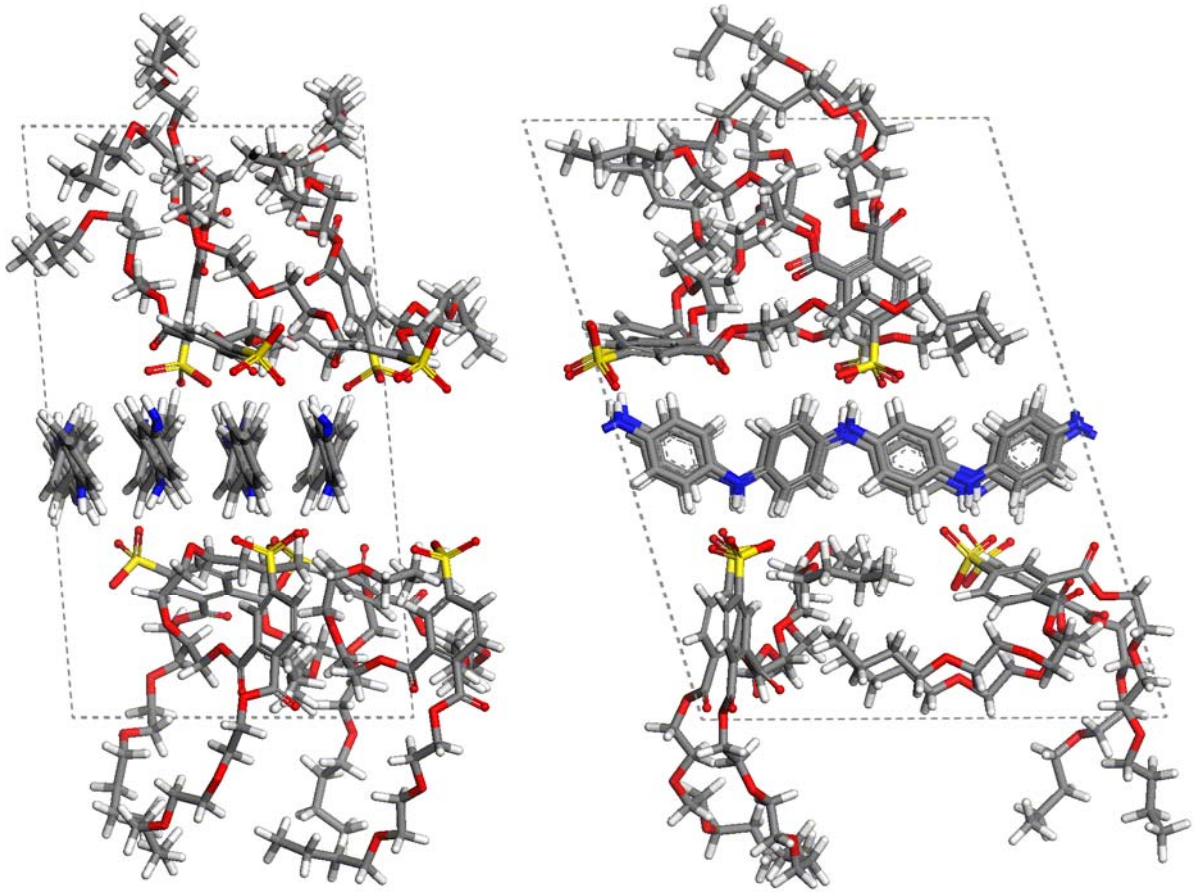

Fig. C.4.2 Small simulation box

The periodic box with starting configuration of atoms was then brought to the procedure of structure stabilization to avoid the artificial diffusion effects during MD simulations. The stabilization procedure (geometry optimization) was a combination of several steps repeated until the total energy of the system reached a constant value. First the charge equilibration (Qeq) was done for 500 steps of energy minimization procedure using “smart minimizer” and truncated Newton algorithm. These two steps were subsequently repeated until energy became stable. Next, the initially equilibrated models were used as a starting point for a 200 ps long molecular dynamic simulation with constant pressure and temperature (NPT ensemble). The charge equilibration was done every 20 ps simulation step. At each step, the energies, pressure and cell parameters were checked and analyzed. The trajectory files with frames saved every 0.2 ps were created. Usually after 100 ps of simulation, total energy reached a constant value and the cell parameters were oscillating in a small interval around their equilibrium values due to cell size effects. (the oscillation period is proportional to cell dimensions). The average values over the last 100 ps of simulation were taken to estimate parameters of the cell used for further calculations. The stabilization procedure was used to

prepare series of models equilibrated at different temperatures and ready to be used in NVT simulations with constant volume and constant temperature (canonical ensemble). It was necessary to find the models for 110K, 210K, 225K, 280K, 310K, 340K temperatures probed in neutron scattering experiments to solve the problem of thermal expansion of the system.

NVT simulations

The molecular dynamics simulations MD were carried out in the NVT – constant volume, constant temperature – canonical ensemble. Independent simulations were done for the models with starting configurations prepared for all tested temperatures. Six trajectory files for each temperature 110K, 210K, 225K, 280K, 310K, 340K have been saved. The frames with atomic coordinates and other cell parameters were saved every 0.1ps. The MD simulations were performed for the maximum time of 250 ps. The initial atomic velocities were estimated from Maxwell-Boltzmann distribution.

Big simulation box

The periodic box contained 9312 atoms, comprising two consecutive bi-layers PANI/DB3EPSA/DB3EPSA/PANI with 12 PANI segments of 8 benzene rings each (figure C.4.3). The procedure of stabilization of the structure was similar to that described for the small box but this time only one temperature (300K) was considered. The total simulation times were 1 ns for stabilizing the structure and also 1 ns for MD simulations. For this bigger simulation we used a simplified force field. Non bonded interactions were evaluated by using a cut off distance instead of the Ewald summation technique. The cut off was applied with a switching function with a spline-on distance of 8 Å and a spline-off distance of 9 Å for Coulomb interactions, while a simple cut off at 8 Å was used for the Van der Waals interactions. An additional simplification involved switching off the cross terms in the energy expression.

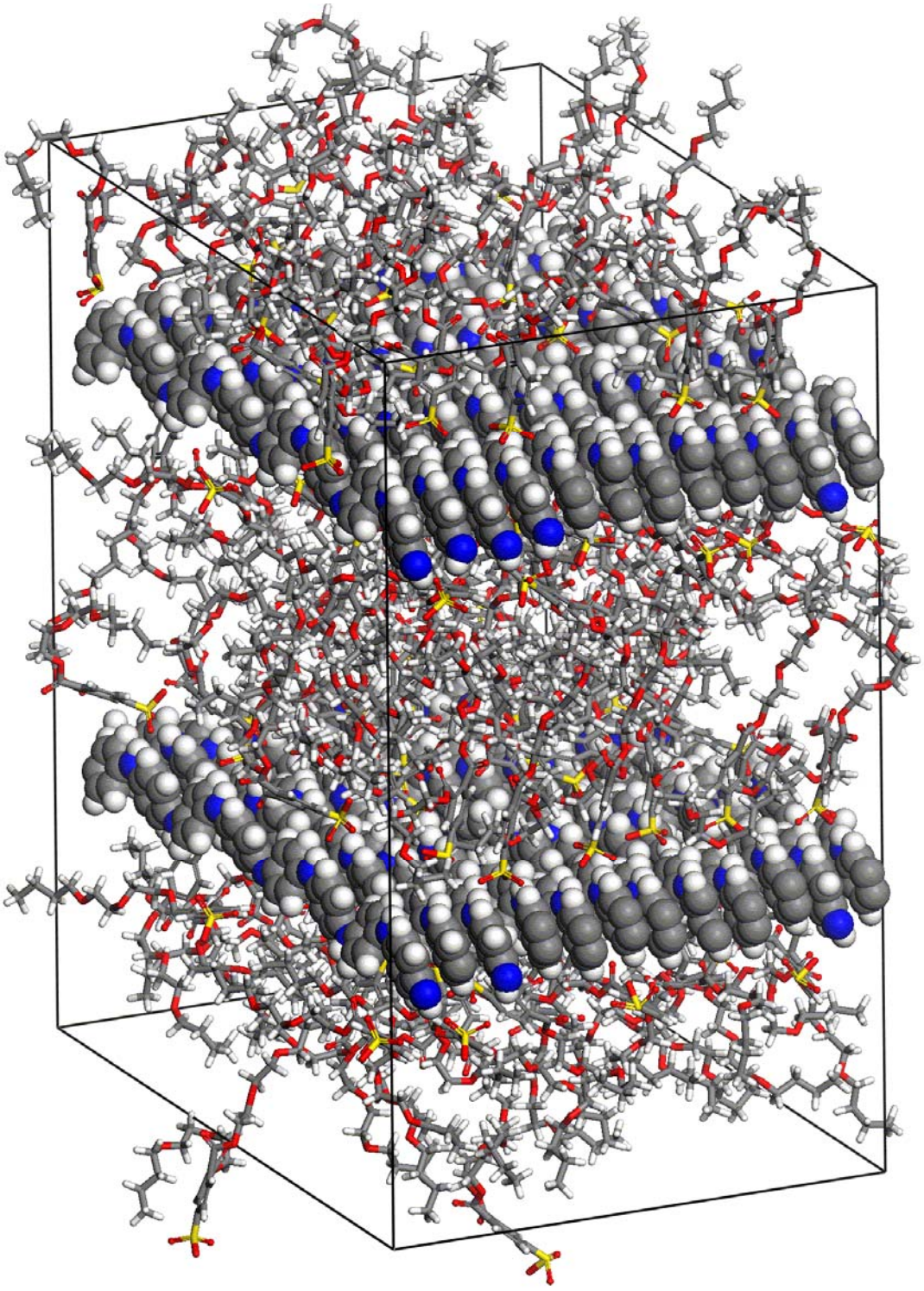

Fig. C.4.3 Big simulation box viewed in perspective

C.4.5 Calculation of neutron scattering functions, atoms mean square displacements, vibrational density of states vDOS

MD simulations are very powerful methods for determining the structural and dynamical properties of molecular compounds. These calculations are complementary to quasi-elastic neutron scattering (QENS) since they probe similar length and time scales (Å and ps-ns). Detailed analysis of the calculated trajectories enables neutron scattering intensities to be determined. Information on the dynamics of individual hydrogen atoms can be obtained from the incoherent scattering function S(q,ω) which is the Fourier transform of Intermediate scattering function multiplied by the resolution function of the instrument used in experiment R(q,t). The incoherent scattering function is called the dynamic structure factor (see chapter C.3.1 QENS theory)

$$S_{inc}(q,\omega) = \frac{1}{2}\int_{-\infty}^{\infty} I(q,t)R(q,t)\exp(-i\omega t)dt \tag{C.4.21}$$

The intermediate scattering functions can be directly computed from MD trajectories of the atoms following the Fourier transform method used in nMoldyn package [70]

$$I(q,t) = \sum_i b_i^2 \left\langle \exp\left[-iqr_i(0)\right]\exp\left[-iqr_i(t)\right]\right\rangle$$
$$or \tag{C.4.22}$$
$$I(q,t) = \int_V G_s(r,t)\exp(iqr)d^3r$$

Where G(r,t) is a time-space self correlation function, $r_i(t)$ describes the position of an atom at time t.

Simulation of QENS experiment in time range of IN6 spectrometer

In the following paragraphs the experimental results of quasi-elastic neutron scattering obtained for plast-doped polyaniline films on IN6 spectrometers are compared with scattering functions computed from the atoms trajectories obtained by the molecular dynamics simulations (MD). Detailed description of the experiments carried on IN6 spectrometer and applied MD simulation techniques are presented in chapter C. Results of the classical analysis of QENS data and proposed models of protons dynamics in various time ranges are presented

in the chapter D.4. Now we can use all the advantages that give us MD simulation techniques to simulate scattering and examine proposed analytical models.

The procedure of calculation of quasi-elastic scattering function from trajectories consists of several steps:

1. computation of the intermediate scattering function I(q,t)

$$I(q,t) = \sum_i b_i^2 \langle \exp[-iqr_i(0)] \exp[-iqr_i(t)] \rangle \qquad \text{(C.4.23)}$$

   where brackets <…> represents an average over the times and all q vector orientations. The summation is performed over all the atoms in the simulation box. Each atomic contribution is multiplied by corresponding normalized incoherent scattering cross-section coefficient b_i^2.
2. The resolution function of the spectrometer was taken into account by multiplying I(q,t) by function R(q,t) whose width is inversely proportional to the resolution function of IN6 spectrometer. Because of Fourier transform properties this multiplication in time domain is equivalent to convolution of S(q,ω) with G(q,ω)-resolution function in energy domain. In our case the resolution function was composed of two Gaussians. It was done by fitting low temperature S(q,ω) scans, where only elastic contribution is present since all diffusive motion are frozen. Experimental resolution function depends on the momentum transfer q. Its width increases and intensity decreases with increase of momentum transfer q. For this reason the resolution functions were estimated separately for each simulated q value.
3. Simulated Dynamic structure factors $S_{sim}(q,\omega)$ were calculated by Fourier transform of the product of simulated intermediate scattering function by experimental resolution function $I_{sim}(q,t)$ *R(q,t).

It should be note that the simulated scattering functions are calculated with constant momentum transfer q. The experimental scattering functions are collected for different scattering angles θ. The momentum transfer q depends on scattering angle, but is also related to the energy transfer $\hbar\omega$ with the equation:

$$q^2 = \frac{8\pi^2}{\lambda^2}\left[1 + \frac{\hbar\varpi}{2E_0} - \left(1 + \frac{\hbar\varpi}{2E_0}\right)^{\frac{1}{2}}\cos\theta\right] \qquad \text{(C.4.24)}$$

Where λ and E_0 are wavelength and energy of incident neutrons respectively

As a consequence the momentum transfer for a given angle is not constant and varies as a function of energy transfer. However, in the case of quasi-elastic neutron scattering (this is our case) energy transfers are small and the momentum transfer varies only a little. In this case we do not do a large error by directly comparing the scattering functions $S_{sim}(q,\omega)$ simulated at constant q with the experimental results obtained at constant scattering angle θ.

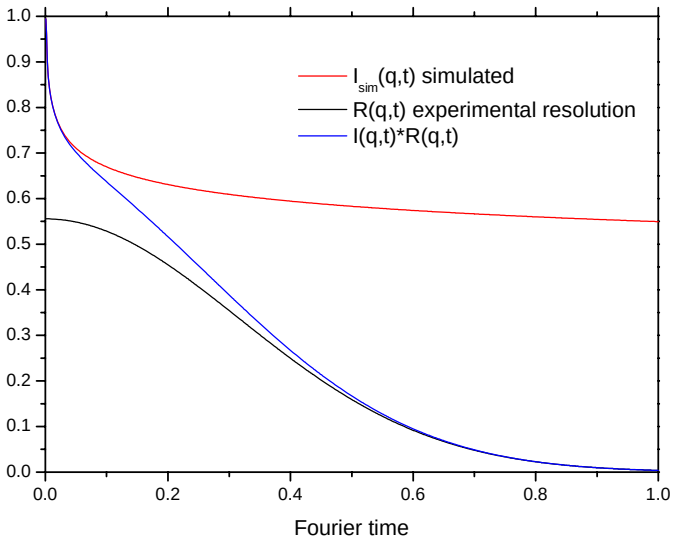

Fig. C.4.4 Simulated Intermediate Scattering function and its convolution with the resolution function

Simulation of elastic incoherent structure factor EISF.

The elastic incoherent structure factor EISF is defined as the long time limit of the diffusive part of the intermediate scattering function. The EISF is the fraction of purely elastic intensity contained in the total integrated intensity.

$$EISF(Q) = \frac{I^{elas}(Q)}{I^{elas}(Q) + I^{quasi}(Q)} \qquad \text{(C.425)}$$

The EISF's were computed from MD trajectories with the following relation:

$$EISF(Q)=\sum_i b_i^2 \left| \left\langle \left\langle \exp(-iQn(t) \right\rangle_t \right\rangle_{\hat{Q}} \right| \qquad \text{(C.4.26)}$$

Where $\langle\ldots\rangle_t$ and $\langle\ldots\rangle_Q$ stand for time average and spherical average, respectively. Due to the experimental EISF extraction procedure, the vibrational motions do not contribute to the measured EISF. The EISF obtained from simulations are computed without decomposition of the atomic trajectories into their vibrational and diffusive parts. To compare experimental and simulated elastic structure factors it is thus necessary to take into account the Debye-Waller factor. The relation between simulated and experimental EISF is therefore:

$$EISF_{sim}(Q)=\exp\frac{-Q^2\langle u^2\rangle}{6} EISF_{\exp}(Q) \qquad \text{(C.4.27)}$$

Where $-Q^2\langle u^2\rangle/6$ is the Debye-Waller factor. $\langle u^2\rangle$ is the mean square vibrational displacement of the atoms.

Mean square displacements

The computation of mean square displacements (MSD) or $\langle r^2\rangle$ are indicating the amplitude and characteristic times of molecular motion in the system.

Mean square displacement is calculated fro molecular dynamics trajectory as follows:

$$< r^2(t) >= \frac{1}{n}\sum_{i=1}^{n}\left\langle \left[r_i(t-t_0) - r_i(t_0) \right]^2 \right\rangle \qquad \text{(C.4.28)}$$

Where n is the number of data points (atoms) used for computation, $r_i(t)$ is a position of atom i at time t, $\langle\ldots\rangle$ stands for an average over the origins of times t_0.

Vibrational densities of states

The vibrational densities of states (vDOS) can be computed directly from the molecular dynamics trajectories as follows:

$$vDOS(\varpi) = \frac{1}{6\pi}\sum_i \int_{-\infty}^{+\infty} e^{-i\varpi t} \left\langle v_i(0)\cdot v_i(t) \right\rangle dt \qquad \text{(C.4.29)}$$

Where $\langle v_i(0) \cdot v_i(t) \rangle$ is the velocity autocorrelation function, $v_i(0)$ and $v_i(t)$ are the velocities of an atom i at times 0 and t respectively. The energy resolution Δω of calculated vDOS(ω) is given by: $\Delta\varpi = \frac{\pi}{t_{\max}}$ where t_{max} is the time length of analyzed trajectory.

D. Results and discussion

D.1 X-ray diffraction and Small angle X-ray scattering results

The following paragraphs present the results of wide angle X-ray scattering (WAXS) obtained in two experimental geometries: transmission and reflection. The results of Small angle X-ray scattering in transmission geometry are also presented. All experimental details are described in chapters C.1. and C.2.

PANI doped with sulfonic acids

First generation plast-dopants (sulfophtalates)

PANI/DPEPSA

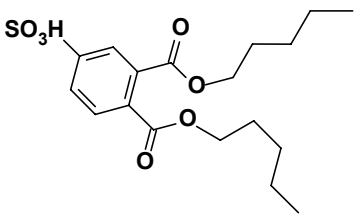

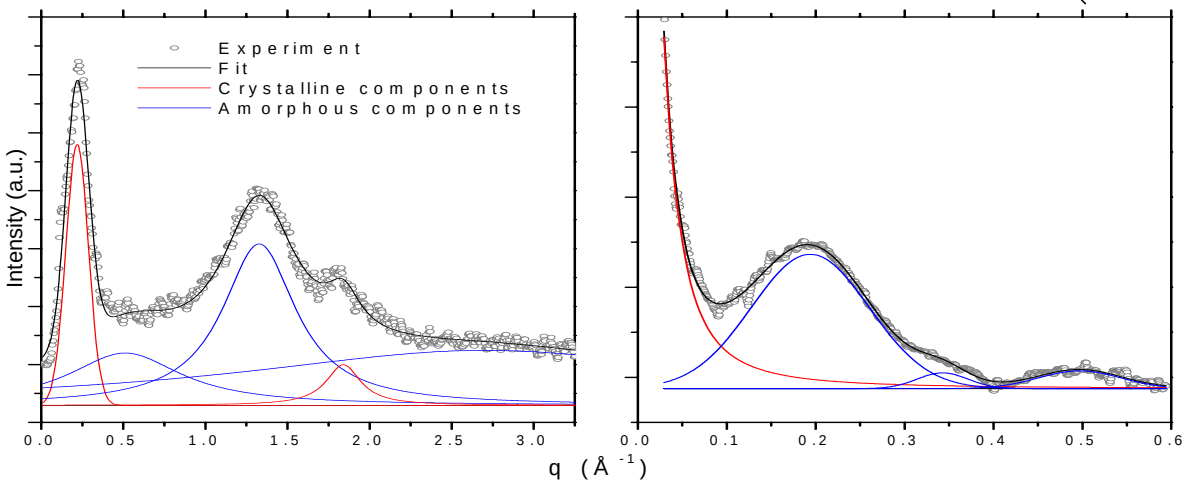

Fig. D.1. 1 WAXS profile (left), SAXS profile (right)

PANI/DOEPSA

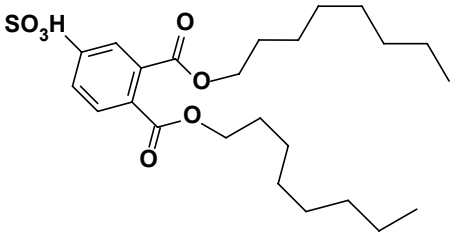

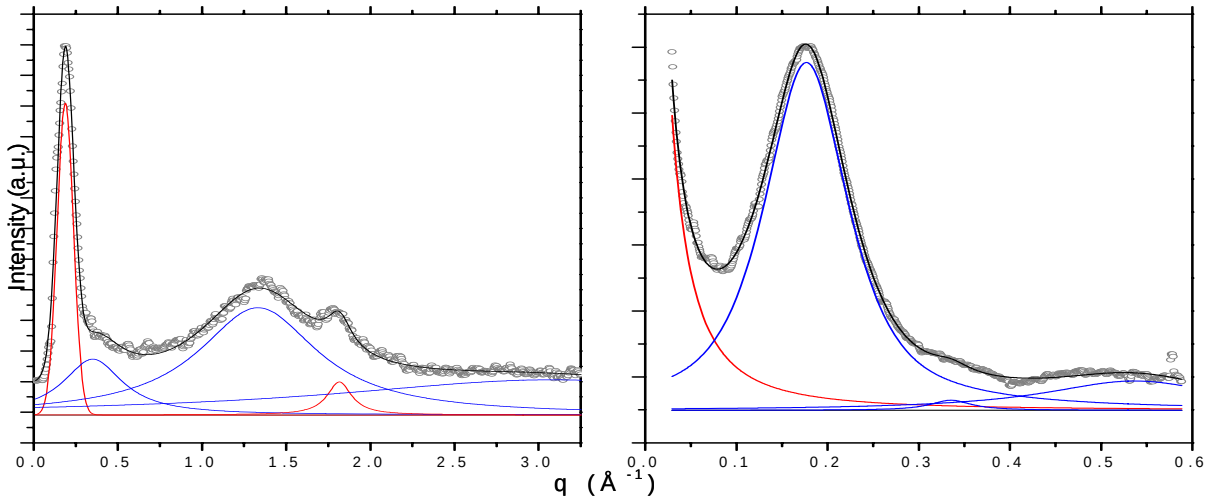

Fig. D.1.2 WAXS profile (left), SAXS profile (right)

PANI/DDEPSA

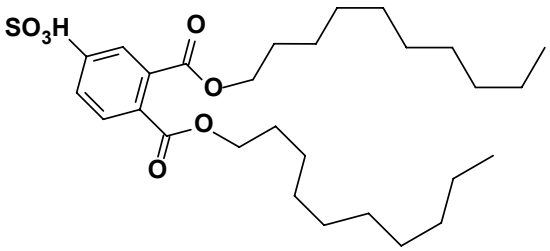

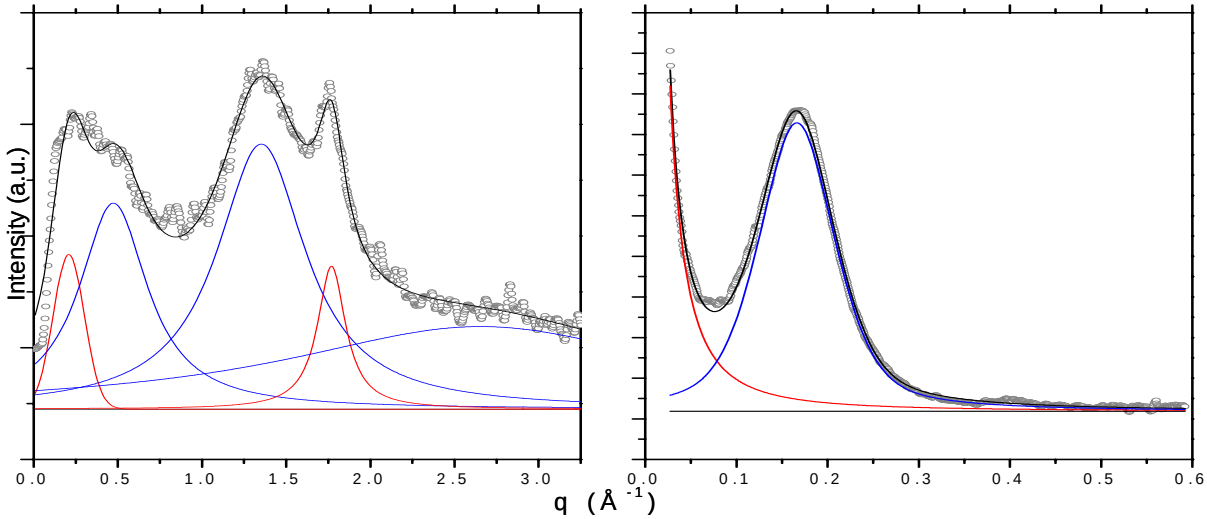

Fig. D.1.3 WAXS profile (left), SAXS profile (right)

PANI/DDoEPSA

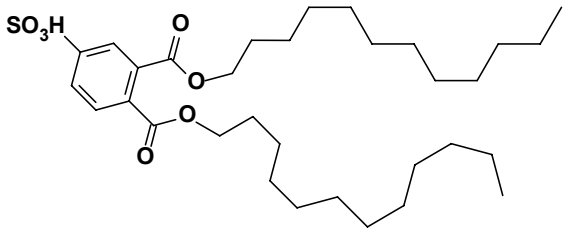

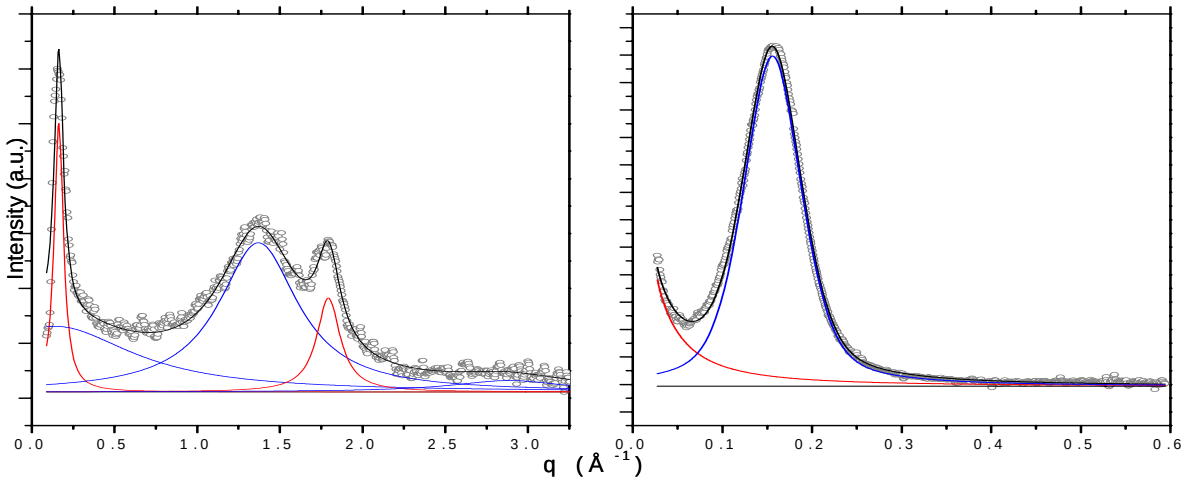

Fig. D.1.4 WAXS profile (left), SAXS profile (right)

PANI/DB2EPSA

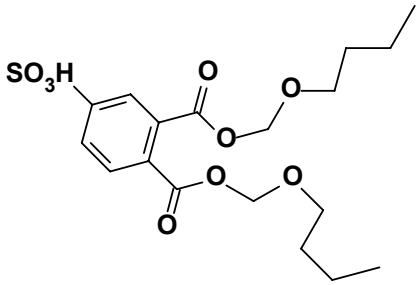

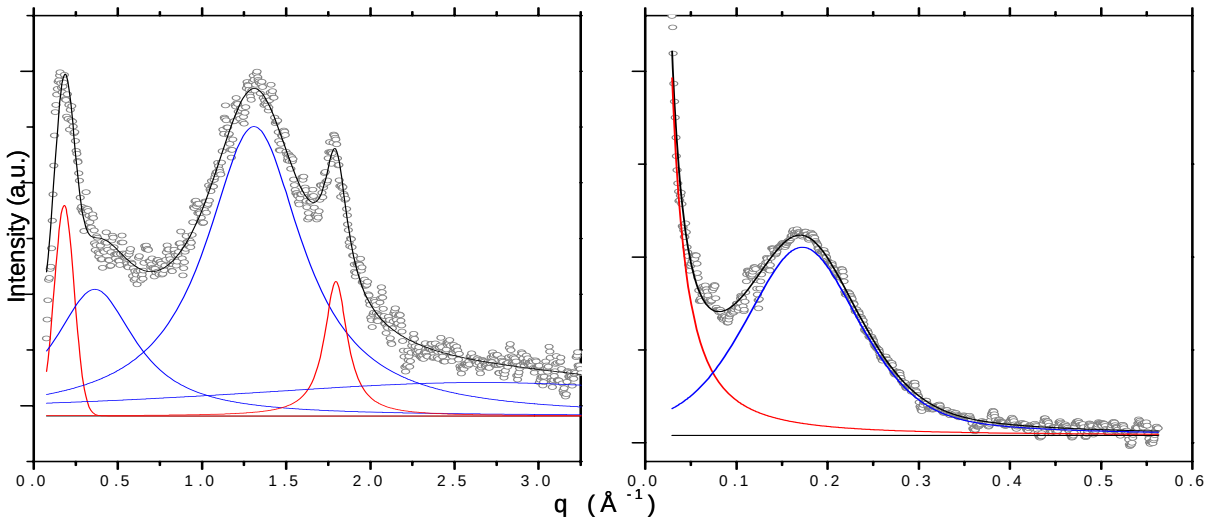

Fig. D.1.5 WAXS profile (left), SAXS profile (right)

PANI/DB3EPSA

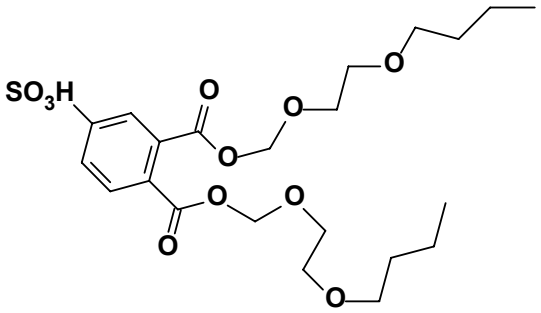

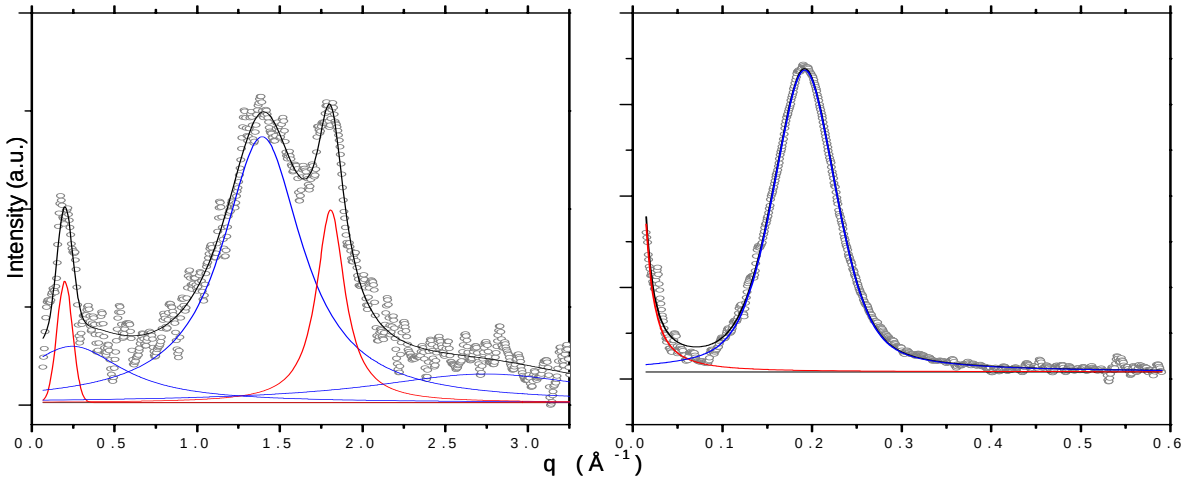

Fig. D.1.6 WAXS profile (left), SAXS profile (right)

Table D.1.1

Plastdopant	WAXS				SAXS		
	Main Peaks pos. (Å^{-1})			Crystallinity index %	Peak pos. (Å^{-1})	Width .(Å^{-1})	Coherence length(Å)
DPEPSA	0.21	1.35	1.8	35	0.193	0.15	98
DOEPSA	0.18	1.33	1.79	40	0.176	0.11	131
DDEPSA	0.2	1.35	1.76	25	0.166	0.09	146
DDoEPSA	0.16	1.37	1.79	38	0.155	0.07	171
DBEEPSA	0.18	1.31	1.79	25	0,172	0.14	110
DBEEEPSA	0.18	1.39	1.8	35	0,191	0.08	145

PANI doped with sulfonic acids

Second generation plas-dopants (sulfosucinate)

PANI/DDoESSA

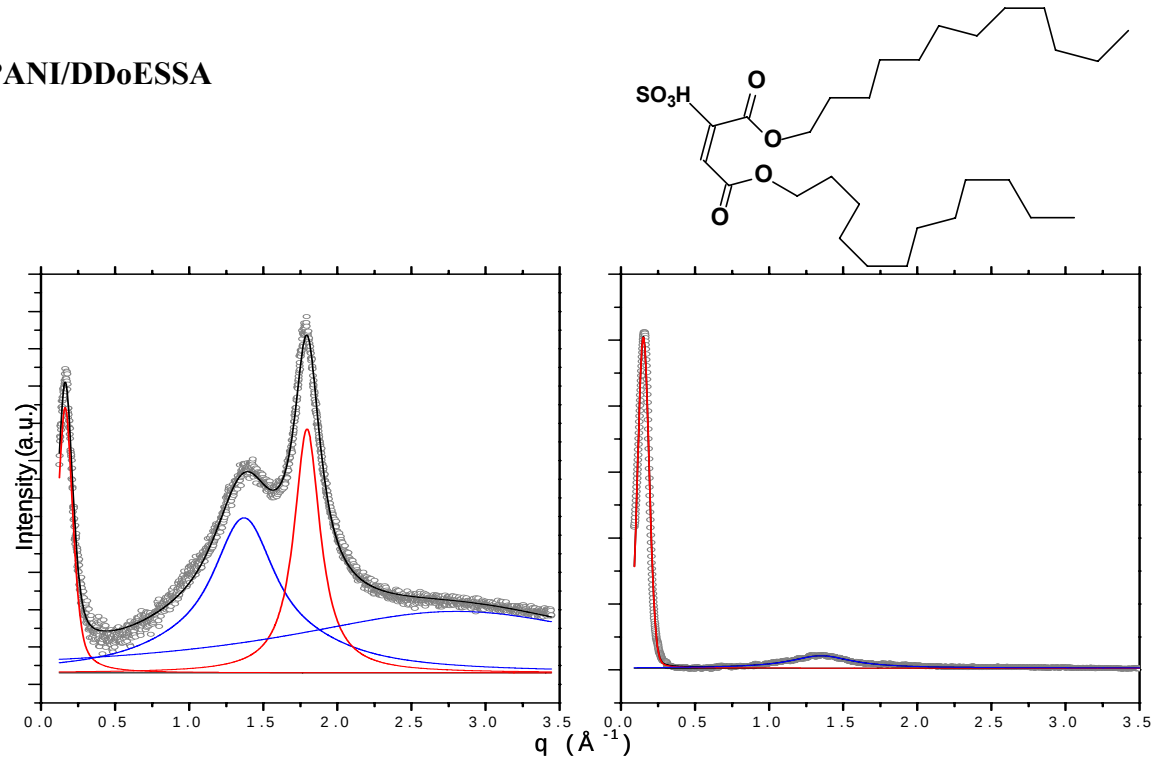

Fig. D.1.7 WAXS profiles reflection (left) transmission (right)

PANI/DB3ESSA

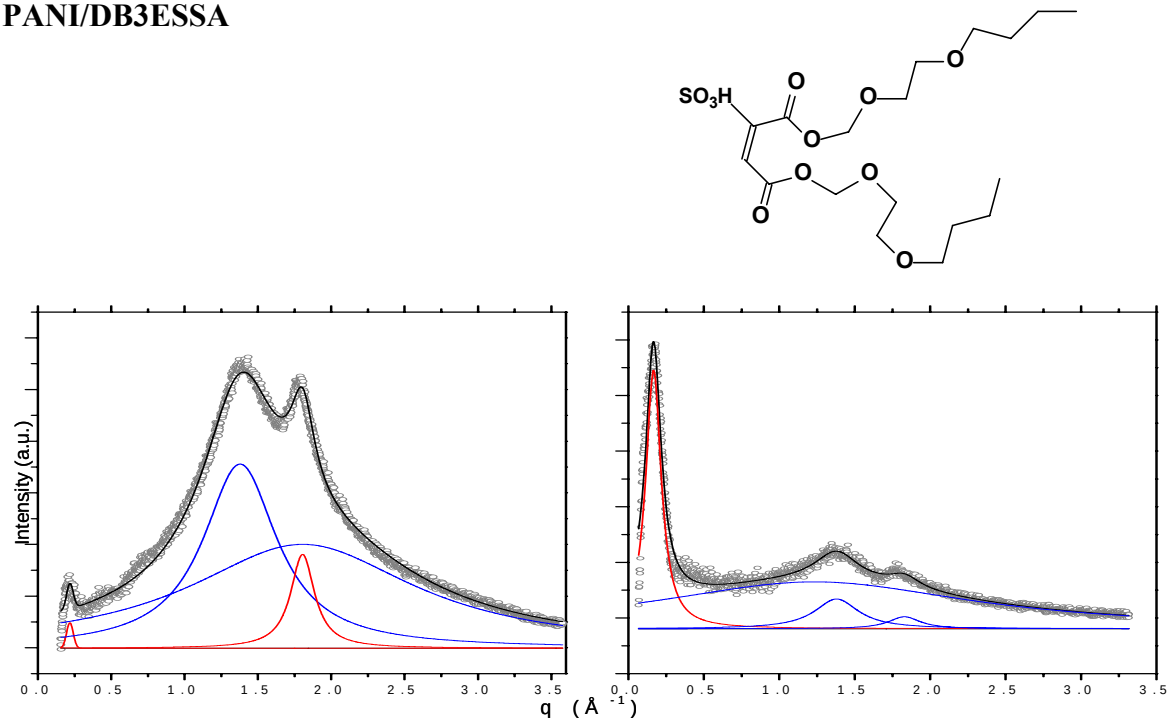

Fig. D.1.8 WAXS profiles reflection (left) transmission (right)

All the previous figures show X-ray scattering results obtained with different plast-doped polyanilines. From the figure D.1.1 to the figure D1.6, wide angle x-ray diffractogramms obtained in transmission geometry are shown on the left while small angle X-ray scattering profiles are shown on the right. All the parameters deduced from these diffractogramms are then collected in the table D.1.1.

The figures D.1.7 and D.1.8 are showing wide angle X-ray diffraction measurements obtained in reflection geometry (left side) and transmission geometry (right side).

D.2 Structural analysis, model of supramolecular structure

D.2.1 X-ray diffraction results obtained on unstretched films

WAXS profiles recorded for PANI doped with plasticizing dopants are shown in the figures D.1.1-8 They are distinctly different from those measured for the crystalline forms of emeraldine base, PANI doped with inorganic acids [71] and PANI doped with camphor sulfonic acid [72]. All these diffraction patterns can be described as consisting of one somewhat sharp reflection at small q values (q= 0.15-0.25 $Å^{-1}$), one broad diffuse feature with an intensity maximum centered at q = 1.35 $Å^{-1}$ and a narrower one at q = 1.78 $Å^{-1}$ (q is the scattering vector whose modulus is $\frac{4\pi \sin\theta}{\lambda}$). The position of the reflection in the small q region is strongly dependent on the size of the alkyl (alkoxy) substituent in the dopant, being shifted towards lower q with increasing alkyl (alkoxy) chain length (see fig.D.2.1). To the contrary, the positions of the two peaks at q = 1.35 $Å^{-1}$ and q = 1.78 $Å^{-1}$, corresponding to d = 4.6 Å and 3.5 Å respectively, are independent of the size of the dopant (fig.D.2.2).

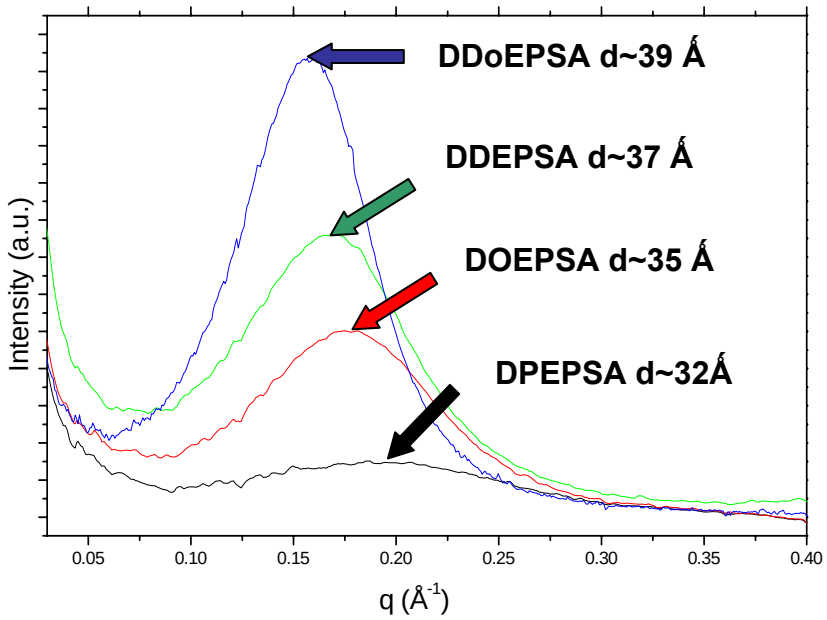

Fig.D.2.1 Evolution of SAXS peak position as a function of the dopant size.

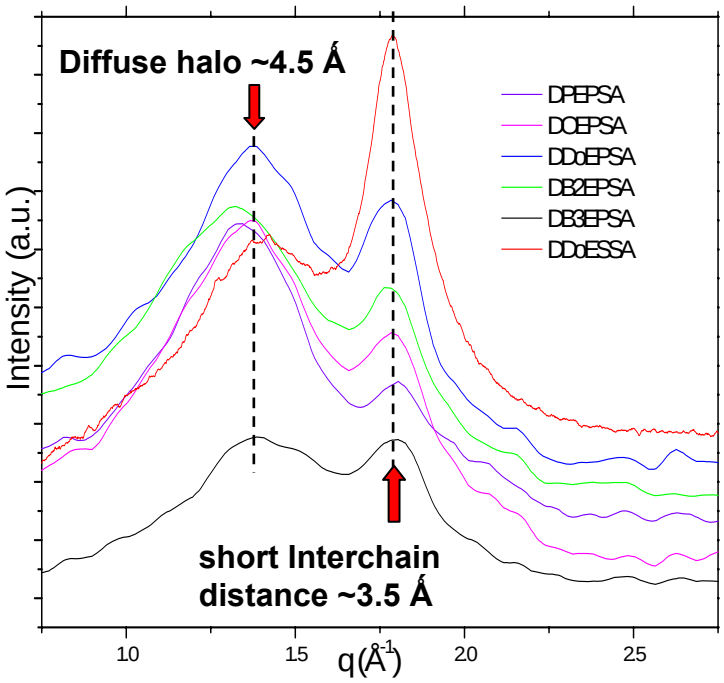

Fig.D.2.2 Comparison of WAXS patterns of polyaniline doped with various plast-dopants

On a simple basis of molecular size and geometry considerations we first attributed the small q reflection to a PANI chain/dopant bilayer/PANI chain repeat distance in which the

alkyl (alkoxy) groups of the dopant act as spacers. The d-spacings corresponding to the two other main reflections are characteristic of van der Waals distances between aliphatic chains (d = 4.5 Å) and between stacks of phenylene rings (d = 3.5 Å). This simple picture led us to a layered structure in which stacks of polymer chains are separated by a bilayer of dopant anions as it is schematically shown in the fig.D.2.3

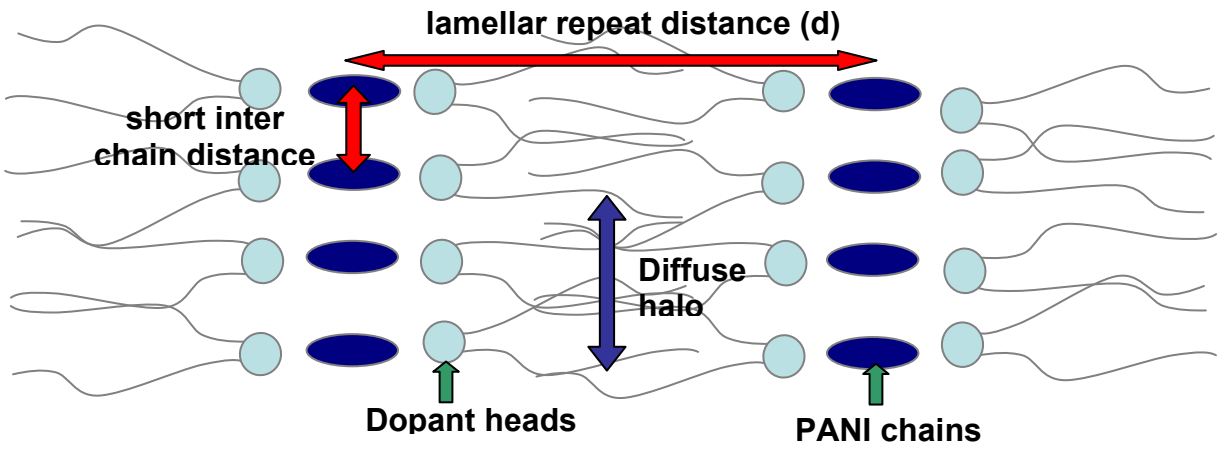

Fig. D.2.3 Schematic view of polyaniline/plastdopant layered structure.

At this stage, it should be noted that such layered and in some cases lamellar like structural organization is frequently observed in systems combining relatively stiff chains of conducting polymers doped with surfactant type anions containing long flexible chains. For example, it was postulated for polypyrrole doped with *n*-alkylsulfates [73] and for PANI doped with dodecylbenzene sulfonic acid [74]. Such molecular architectures were also reported for different types of polymers containing basic sites in their main chain backbone and protonated with acids containing alkyl type surfactant groups [75][76]. The main difference that distinguishes the diffractograms recorded in this research from those observed for PANI doped with dodecylbenzene sulfonic acid [77] is the presence of a relatively sharp reflection at d= 3.5 Å, which is nonexistent in the latter system. This observation may suggest a much more regular stacking of polymer chains in plastdoped PANI as compared to other doped PANI based systems. Finally it is worth to note that recently Stepanyan et al. have theoretically established the stabilization of such lamellar phases in systems constituted of a stiff polymer backbone and flexible side chains [78]. In the case of WAXS experiments the position of the peak at q = 0.15-0.25$Å^{-1}$ is close to the low angle experimental limit. This may

lead to an abrupt cut caused by the beam stop shadowing of the detector and as a consequence to an incorrect determination of the peak features (mainly the position of its maximum and its full width at half maximum). For this reason we have undertaken SAXS experiments which allow for a more precise determination of the position, the width and the global shape of the reflection in the considered q range. All the obtained scattering profiles are shown in the series of figures D.1.1 to D.1.8. Direct comparison of these SAXS peaks clearly indicates that the extent of the above described layered-type ordering in plastdoped PANI strongly depends on the size of the alkyl (or alkoxy) group in the doping ester. In particular the peak, registered for the polymer doped with the ester containing the shortest *n*-alkyl group *i.e.* PANI(DPEPSA)$_{0.5}$, is very broad and rather poorly defined. With increasing length of the alkyl substituent the peak becomes more intensive and narrower indicating an increasing ordering. This narrowing is accompanied by a shift of the peak maximum towards lower q values as expected for the increasing dopant size. It can therefore be noted that different features of the profiles find their physical origin in numerous atomic positional fluctuations modulating the local and global shapes of the assemblies of alternating layers of PANI chains and counter-ions.

D.2.2 Structural anisotropy of unstretched films

By varying the scattering vector q orientation (experiment geometry) we explored ordering of the structure in different directions of space. Combining the experiments in transmission and reflection allow us to study the main structural orientations in the film. Orientations of q vector with respect to the studied film geometry are shown in fig.D.2.4

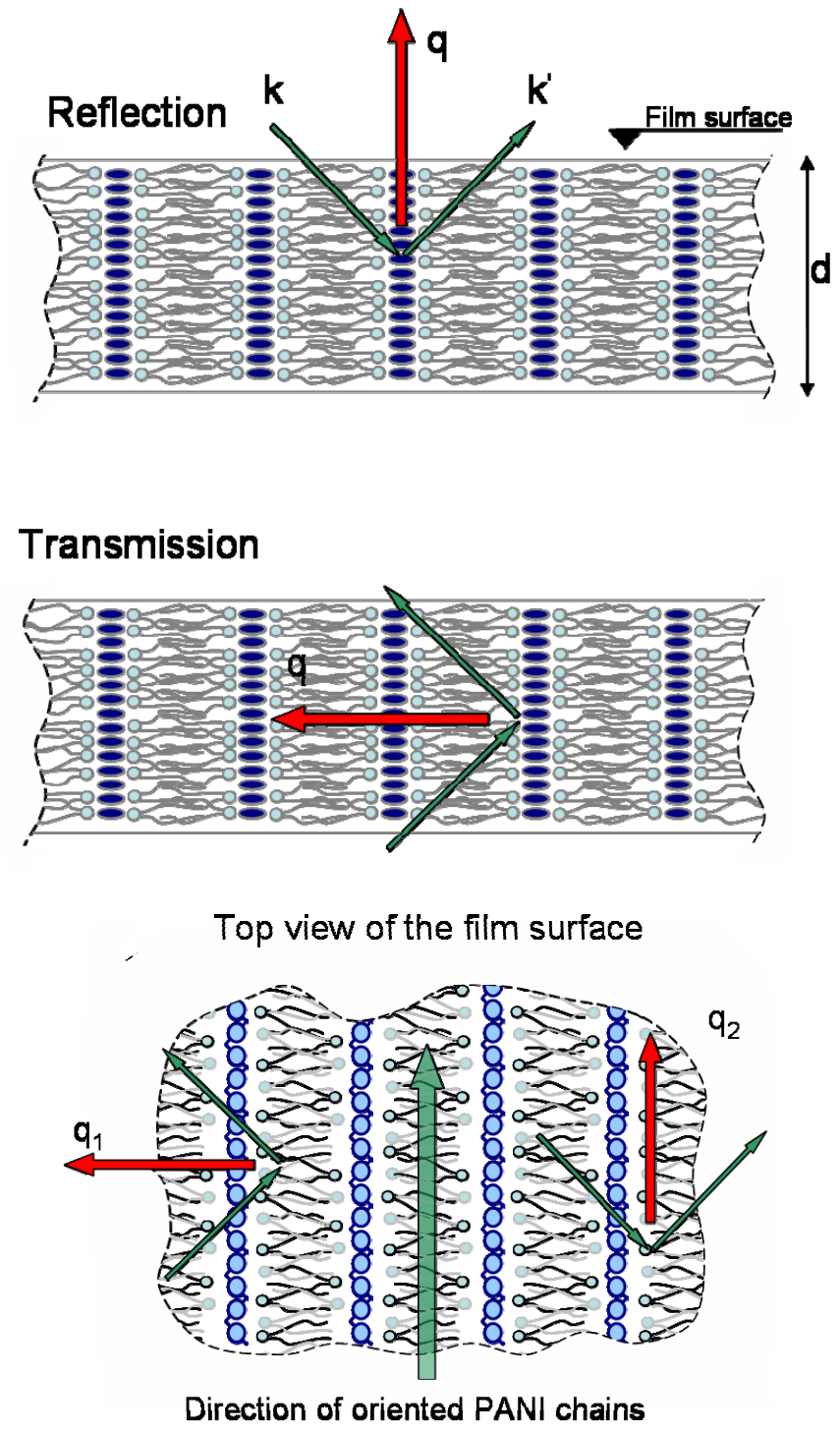

Fig D.2.4 Schematic view of a 100% oriented plast-doped polyaniline film with different possible scattering q vector orientations.

Out of plane structure of films

All the films exhibited a strong anisotropy between the in-plane and the out of plane structures as proved by the comparison between the transmission and reflection diffractograms when q vectors are oriented parallel and normal to the film surface respectively. Relative intensities of sharp maximum at small q values (0.15-0.25 $Å^{-1}$) that corresponds to the long period lamellar stacking distance are much larger in transmission than in reflection. To the contrary, the relative intensities of peak at q = 1.78 $Å^{-1}$, corresponding to d = 3.5 Å (inter chain distance in polyaniline stacks) are higher in reflection than in transmission. For some samples especially containing long and flexible tails in dopants *i.e.* DDoEPSA, DDoESSA and DB3ESSA, this anisotropy seems to be even stronger than for samples with short dopants tails as DPEPSA, DHESSA and DB2EPSA (almost 100% orientation in DB3ESSA). Combining these anisotropy observations with the model of structural organization proposed above, the most reasonable explanation for this feature is that in thin free standing films the crystallites prefer to be oriented with respect to the film surface. In that case it seems to be clear that polyaniline chains must be oriented within the plane parallel to the film surface. Accordingly, polyaniline chains are stacked along the direction normal to the film surface and are separated by dopant counterions as shown in fig. D.2.5

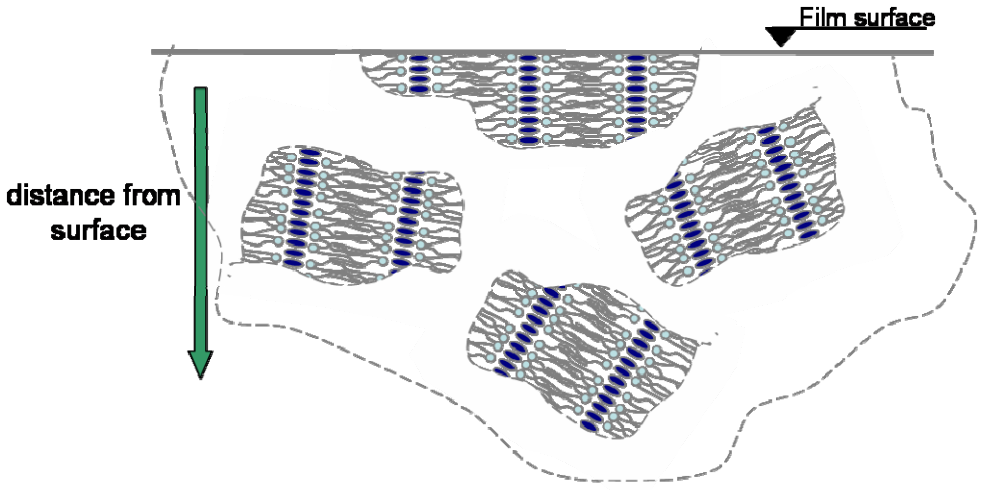

Fig.D.2.5 Schematic side view of plast-doped polyaniline film. Crystallites with various orientations and the effect of orientation near the film surface are shown.

Concerning the long period lamellar ordering, in this respect, it would be oriented within the film plane. Going deeper inside the film, the influence of the surface on this type of orientation may become weaker. That is why we observed only a partial orientation (some

intensities are registered both in transmission and reflection). Stronger anisotropy appears for thin free standing films obtained from solution where surface effects dominate (first and second generation plastdopants). It is interesting to note that for example the films of polyaniline doped with phosphoric acid diesters obtained by mechanical process (pressing) are much thicker, and show only poor orientation. Concerning the broad line around 1.35 $Å^{-1}$, it can be noticed that it was seen in both geometries. In our opinion this diffuse line is centered at a position typical to the mean Van der Waals distance separating aliphatic chains. However, it should be also noted that the relative intensity of this line is much bigger in reflection geometry than it is in transmission geometry. That would indicate that the correlations among flexible tails are stronger in the meridional plane than they are in the equatorial plane. We may call this type of disordered tail organization as "oriented amorphous". The degree of this orientation is also dependent on the dopant tails lengths and shapes. This type of anisotropy is much more visible for long regular tails like DDoESSA and almost disappears for short branched DHESSA tails for example.

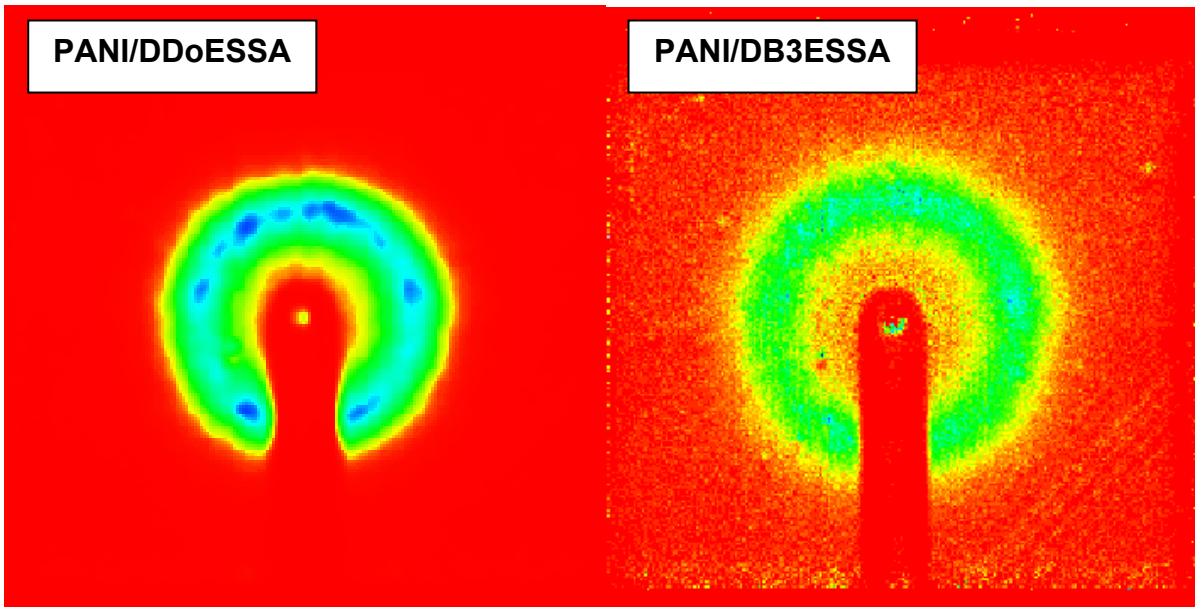

Fig.D.2.6 2D-SAXS patterns of PANI doped with "2nd generation plast-dopants"

In plane structure of films

The two-dimensional small and wide angle scattering profiles (obtained in transmission geometry when q vectors is parallel to the film surface fig.D.2.6) of unstretched films are in majority found isotropically distributed within the plane of films. (Except the profiles obtained for unstretched DDoESSA where we observe some indication of hexagonal or pseudo-hexagonal packing discussed below). Typically there is no reason for appearance of a structural anisotropy within the plane of the film since any direction is preferable, all directions are symmetrical. In a free standing film when solvent evaporates the ordered regions begin to form in many different parts of the film with completely random orientation. As a consequence this in plane structural isotropy distribution within the plane is found.

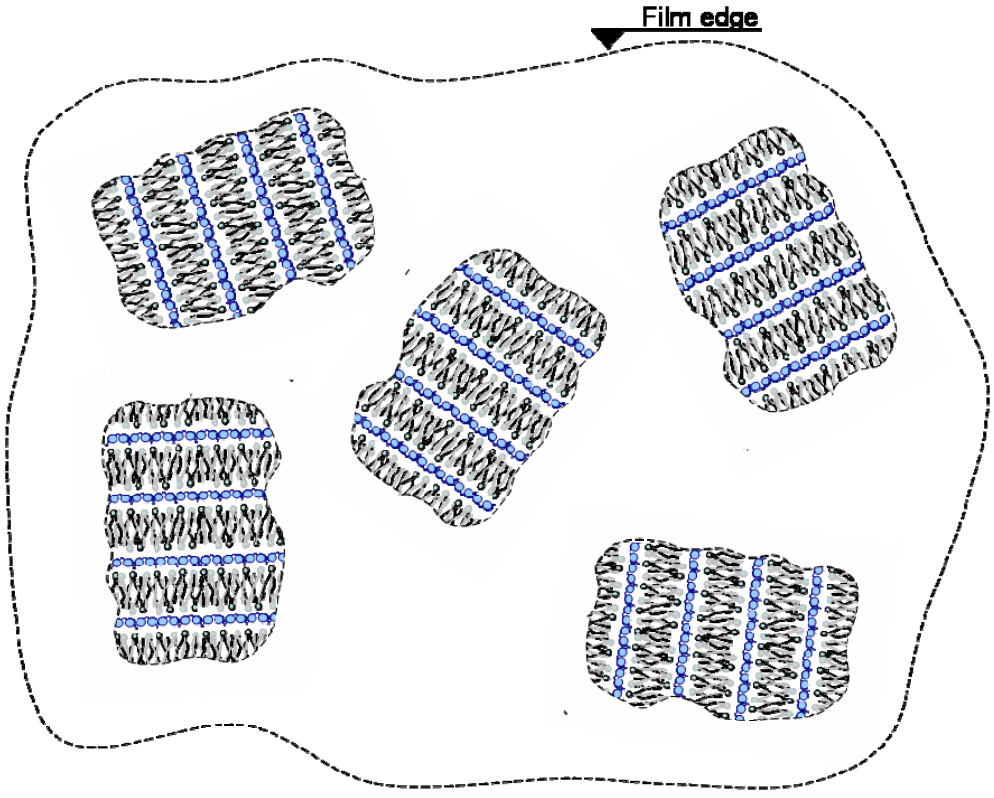

Fig.D.2.7 Random in-plane orientation of ordered regions.

D.2.3 Some remarks on pseudo-hexagonal packing in Pani/DDoESSA unstretched films

2D pattern of small angle X-ray scattering in transmission from the film containing PANI/DDoESSA system shows characteristic ring similar to other samples typical for in plane powder average orientation of the film. But blurred indication of hexagonal packing with the same long period distances as for lamellar packing is observed as six spots regularly distributed along the ring (Fig.(D.2.6)). Several reasonable assumptions may account for such a feature. First we can imagine alternative molecular organization with cylindrical forms packed in a hexagonal lattice. But this concept seems to be unrealistic since these cylindrical forms must be oriented normal to the film surface and perpendicular to the polyaniline chains direction what is difficult to assume. The other explanation may be some integral hexagonal packing inside our model of counter ion head groups for example. But it is also very difficult to imagine. In our view the most promising statement that makes this feature comprehensible is to assume that some orientations are preferred in some cases and this behavior (self assembling) is induced by polyaniline chains properties. This type of self assembling leading to pseudo hexagonal organization was observed for thin films of poly3-hexylthiophenes studied by STM [79] [80]. The explanation of this phenomenon needs some remarks on possible polyaniline chains 2D conformations. The idealized view of extended polyaniline chain is a straight planar zigzag. When we introduce some conformational defect in this planar zigzag by rotating the part of the chains around nitrogen bond we obtain a characteristic bending angle close to 120 degrees between two parts of one polyaniline chain separated by a defect (Fig (D.2.8)).

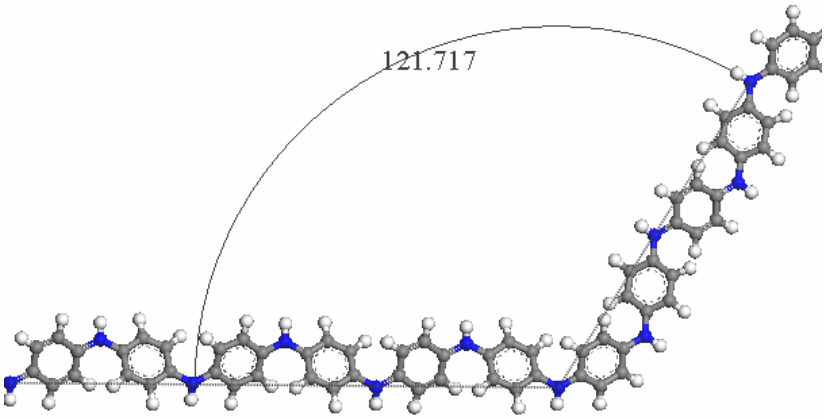

Fig.D.2.8 Planar zigzag of one polyaniline chain with one conformational defect. Characteristic angle between the two parts of the chain is closed to 120 degrees.

It should be noted that such a conformation is highly energetically favored (energy minimization) and this is the only way for one chain to lie in the same plane. If we assume now that one polyaniline chain belongs to more than one ordered region (chains are longer than the coherence length of crystallites) then the orientation of neighboring ordered regions must be correlated (Fig. (D.2.9)). As a consequence in some parts of the film the islands of crystallites oriented with respect to its neighbors are formed giving both pseudo hexagonal and isotropic signatures in the 2D small angle X-ray scattering patterns as seen in the Fig.D.2.6.

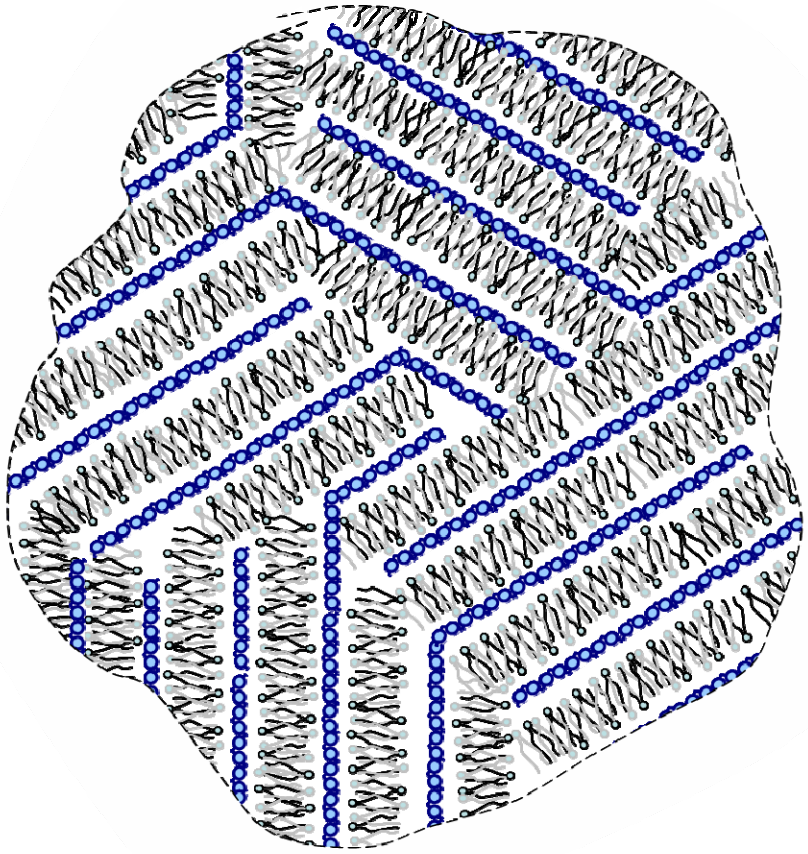

Fig.D.2.9 Schematic view of pseudo hexagonal in plane packing of Pani/DDoESSA film.

D.3 Analysis of distorted lamellar stacking. A model for the statistical fluctuation in the multi lamellar like structure

D.3.1 Theoretical background

From a general point of view, in semi-crystalline polymers, numerous atomic positional defects affect the periodic regularity of the lattice within the crystalline parts of the sample. In order to take into account this physical reality, Hosemann introduced the concept of the paracrystal [81]. The crystal is still built on a perfect crystallographic unit cell but now from cell to cell all the crystallographic parameters can vary statistically. These irregularities influence the X-ray diffracted reflections in shape and intensity. In a typical X-ray diffractogram recorded from a polycrystalline sample, the Bragg peaks appear to be broader and more diffuse than expected on the basis of the classical crystallite size effect. The concept of paracrystallinity led Hosemann to postulate that there are two kinds of distortions of the lattice in real crystal structures. For lattices with the distortions of the first kind, long range periodicity is preserved and the distortions are simple displacements of the atoms from their equilibrium positions prescribed by the ideal lattice points. These distortions are often referred to as frozen thermal displacements and they cause a decrease in the intensity of the series of reflections with increasing reflex order, but no broadening. In a lattice with paracrystalline distortions of the second kind, the long range order is lost and each lattice point varies in position only in relation to its nearest neighbors rather than to the ideal lattice points. Second kind distortions result in both decreasing of intensities and increasing breadth of reflections with increasing reflex order or scattering vector.

The intensity scattered from a lamellar system may be described by the following formula [82]:

$$I(q) = \frac{1}{q^2}\left\langle \left| f(q) \right|^2 s(q) \right\rangle \qquad \text{(D.3.1)}$$

where $q = \frac{4\pi \sin\theta}{\lambda}$ is the absolute value of the scattering vector, f(q) is the form factor, s(q) is the structure factor and $1/q^2$ is the Lorenz factor. Structure and form factors are averaged

over lamellae statistical fluctuations. Then we can consider that the fluctuations within layers are independent of those of the lattice points and accordingly we can write:

$$I(q) = \frac{1}{q^2}\left|\langle f(q)\rangle\right|^2 \langle s(q)\rangle \tag{D.3.2}$$

The form factor for a layered structure is given by the Fourier transform of the electron density distribution profile within a single isolated layer along the z direction perpendicular to the layer surface by

$$f(q) = \int \rho(z)\exp(iqz)dz \tag{D.3.3}$$

According to the paracrystal model, the local spacing between each neighboring pair of layers is a random variable with the mean value d_a and the nearest neighbor fluctuations are independent for each pair of neighboring layers. The mean square fluctuations may be defined by

$$\sigma^2 \equiv \left\langle \left(d - d_a\right)^2 \right\rangle \quad , \quad \sigma_n^2 = n\sigma^2 \tag{D.3.4}$$

where σ_n is the mean square fluctuation of the distance between layers separated by (n-1) layers. That much differs from the mean square fluctuation of the classical crystalline system for which this parameter remains the same for different distances.

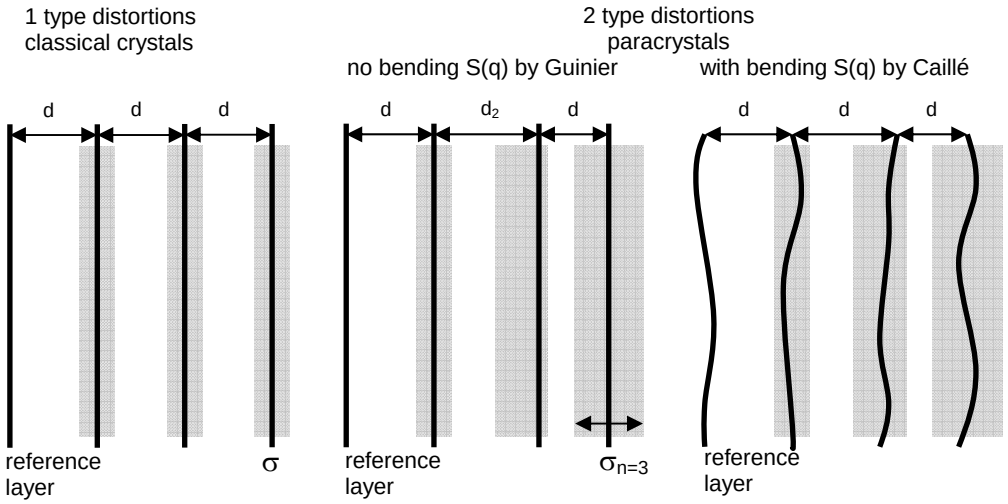

Fig.D.3.1 Schematic view of different types of crystal distortion.

The structure factor giving the scattering from a finite stack of N oriented infinitely thin layers was calculated by Guinier [83]. It may be written in a simplified way as follows:

$$S(q) = N + 2\sum_{n=1}^{N-1}(N-n)\cos(qnd)e^{-n\sigma^2 q^2/2} \qquad \text{(D.3.5)}$$

In this model it is assumed that each lamella remains flat with no bending. The model was generalized to admit such types of disorders by Caillé [84] (Figure D.3.1)

$$S(q) = N + 2\sum_{n=1}^{N-1}(N-n)\cos(qnd)\times e^{-\left(\frac{d}{2\pi}\right)^2 q^2\eta_1\gamma}(\pi n)^{-\left(\frac{d}{2\pi}\right)^2 q^2\eta_1\gamma} \qquad \text{(D.3.6)}$$

where η_1 involves the bending modulus and the bulk modulus for compression of the lattice and γ is the Euler constant. The theoretical structure factors corresponding both to Guinier's and Caillé's models are reported in the figure D.3.2. In the case of phospholipids bilayer systems, it is important to determine the parameter η_1 from the scattering results in order to have a direct access to the microscopic mechanical properties of these model systems for biological membranes [85]. In our case, at this stage of our work on plastdoped PANI, the product ($\eta_1\gamma$) is just considered as a scaling factor.

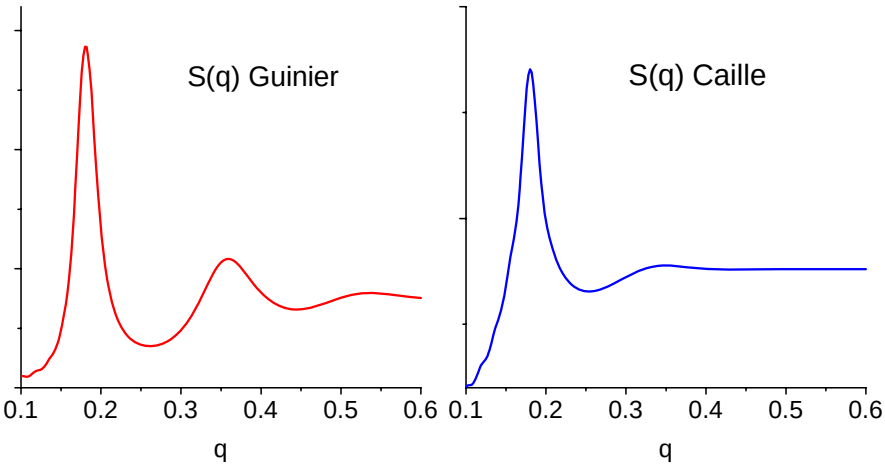

Fig. D.3.2 Theoretical profiles of paracrystalline structure factor S(q) proposed by Guinier and Caillé.

D.3.2 A statistical distribution of the electron density along the stacking direction

The crucial point for carrying out the calculation of the theoretical scattering curves for such lamellar systems is the proper choice of the electron density distribution profile. Plastdoped polyaniline systems and multi-lamellar phospholipid bilayer systems show a remarkable similarity in their respective molecular stacking modes. Accordingly, we have decided to undertake an attempt of modeling the electron density profile as a sum of several gaussian distributions in the same way followed by Pabst et al. [86] for describing some phospholipid bilayer systems. Lamellar model of plastdoped polyaniline is composed of dopant molecules layers with heads and long alkyl (alkoxy) tails separated by the layers of polyaniline chains which may be treated as the host matrix (see the figure D.3.3).

The electron density distributions profile along the z direction of such isolated layers is then described as a sum of gaussian functions as follows:

$$\rho(z) = \rho_H \left(e^{-\frac{1}{2\sigma_H^2}(z-z_H)^2} + e^{-\frac{1}{2\sigma_H^2}(z+z_H)^2} \right) + \rho_T \left(e^{-\frac{1}{2\sigma_T^2}(z-z_T)^2} + e^{-\frac{1}{2\sigma_T^2}(z+z_T)^2} \right) \qquad \text{(D.3.7)}$$

ρ_H and ρ_T are the electron densities of head groups and tails respectively of the counter-ions and they are calculated relatively to the electronic density of one polyaniline layer which is taken as the reference level since it constitutes the host matrix. The gaussian distributions of these electron densities are centered at z_H and z_T, and their widths are σ_H and σ_T. The whole electron density profile is drawn in the figure D.3.3, the different parameters used in the equation (D.3.7) are also reported in the same figure.

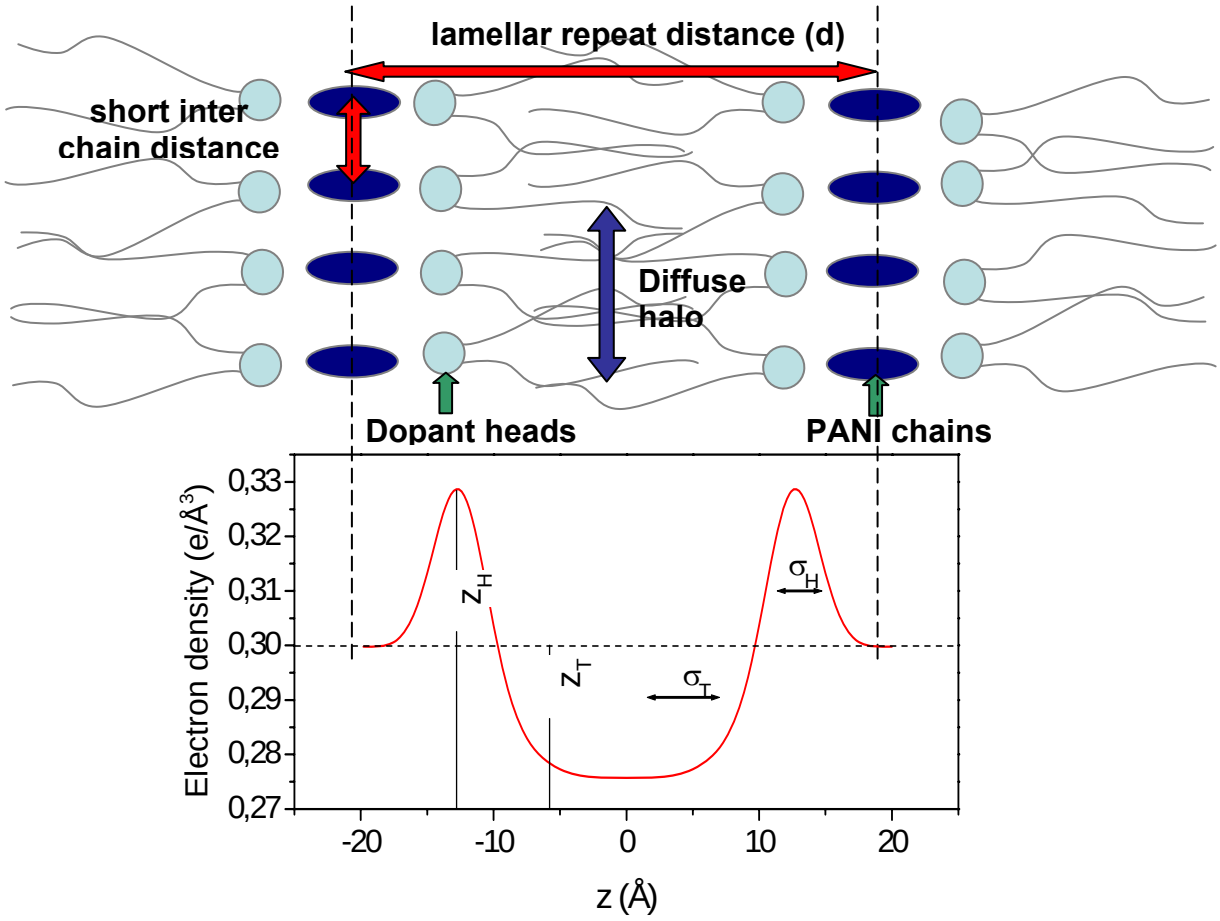

Fig D.3.3 Schematic view of plast-doped polyaniline lamellar structure compared with electron density distribution profile along lamellar stacking (z) direction.

D.3.3 Evaluation of the electron density parameters using molecular dynamics simulations

The main goal was to check the stability of proposed models and extract several important parameters useful for further structural analysis. All the simulations were performed in periodic conditions but the simulation box was big enough to consider that molecules belonging to neighboring boxes are independent from one to each other and that all the correlations are not affected by the periodic conditions (the periodic box contains around 10000 atoms, its dimensions are twice bigger than the long range periodicity of the system). In general, we used force field based molecular dynamics simulation technique to find a realistic model (from a physical point of view) of such layered structure starting from idealized well ordered model and repeating procedure until we obtained statistically disordered with sufficient convergence criteria. Full description of molecular dynamics (MD) simulation techniques, energy minimization, description of potential energy surface (force

field), charge equilibration technique and simulation details are all described in chapter C.4. Building and using a big simulation box enabled a more realistic simulation of the long period lamellar stacking with characteristic statistical fluctuations of inter-lamellar distance, since the individual polyaniline stacked layer is interacting with real neighbor, not only with its mirrors in adjacent boxes. That is essential for estimation of the structural parameters characterizing lamellar sacking in the system. Finally it was shown that applying MD simulation may be useful for the construction of a physically realistic model. This simulation confirmed that the above proposed layered structure is indeed quite stable mainly because of the strong interactions of interdigitating n-alkyl tails as it is shown in the Figure D.3.4, but also because of strong ionic interactions between charged polyaniline layers and counterion head groups.

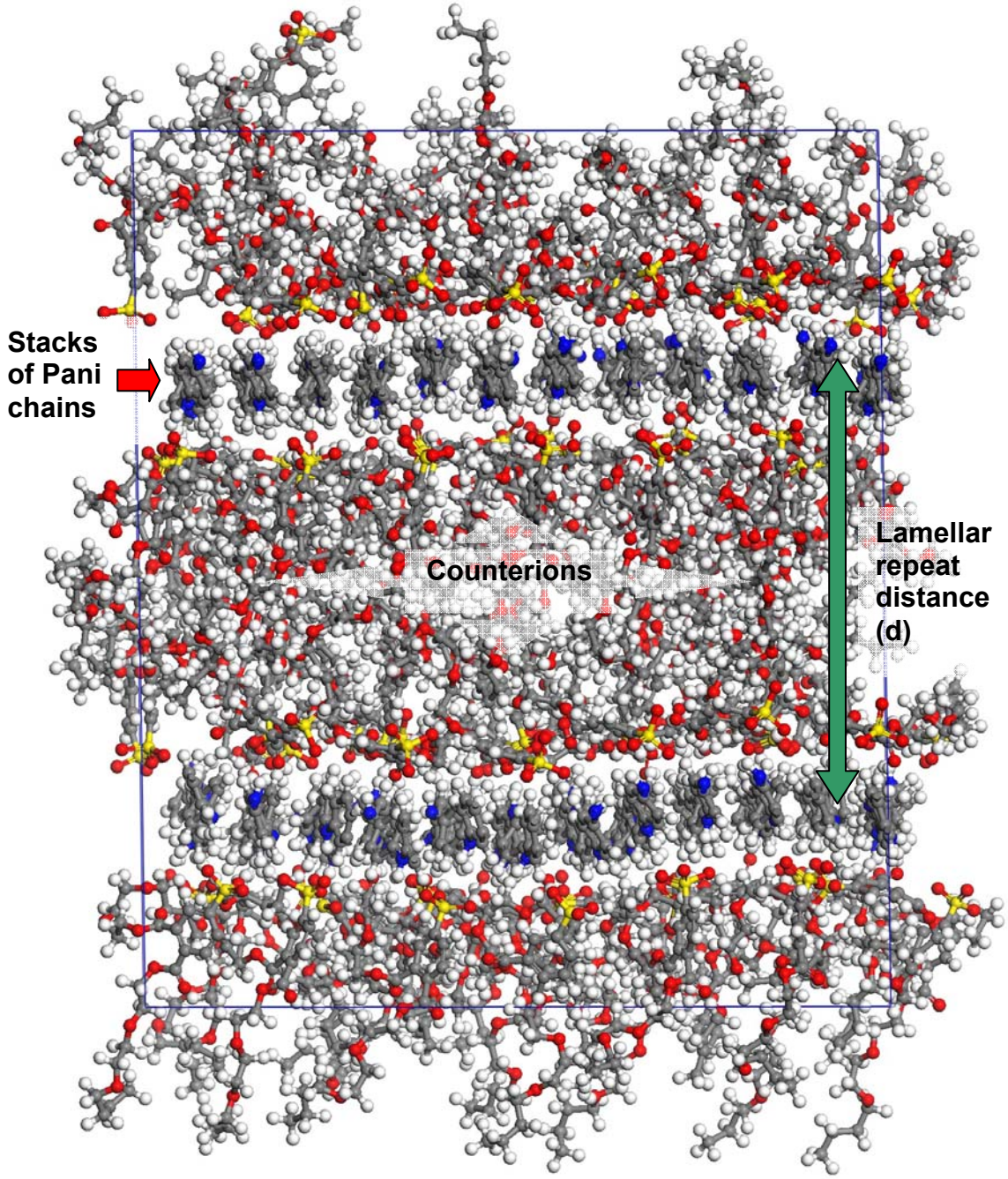

Fig.D.3.4 Periodic box with ~10000 atoms after structure stabilization (1ns MD simulation at room temperature) of Pani/DB3EPSA system. The box contains two bilayers of PANI/DB3EPSA/DB3EPSA/PANI. The view is perpendicular to the PANI chain long axis. The long period lamellar distance is along the vertical direction (carbon: grey, oxygen: red, nitrogen: blue, sulfur: yellow).

D.3.4 Calculation of SAXS profiles

We were particularly interested in carrying out these simulations in order to estimate sets of structural parameters we needed for performing a quantitative analysis of SAXS data and for comparing theoretical calculations with experimental data. In particular, the parameters we could extract from these simulations were necessary to estimate the one-dimensional electronic density distribution profile along the direction perpendicular to the layers as it is written in the equation (D.3.7). Sets of these parameters are collected in the table D.3.4.1. The main parameters we found from the model were the electron densities of the head group ρ_H and that of the n-alkyl tails ρ_T which are reported relatively to the electron density of a PANI chain also estimated from the model and found to be 0.3 e/Å^3. The other important parameters were the mean head to head distance (Z_H*2). If the van der Waals distance in between one PANI chain and the head of one counter-ion is d_{PANI-H}, the repeat distance of the lamellar structure is calculated as $d = 2*(Z_H + d_{PANI-H})$. As value of d_{PANI-H} we found 2.5 – 3 Å if we take d as the position at which is centred the maximum of the SAXS profile (see table D.3.4.1). The electron density distribution profile was used to calculate the form factor of an isolated bilayer consisting of two layers of dopant molecules with head groups being at the surface of the layer and interdigitating n-alkyls tails inside (see Fig. D.3.3). All the form factors of substituents (DPEPSA, DOEPSA, DDeEPSA, DDoEPSA, DBEEPSA and DBEEEPSA) were calculated in the same manner. Form factors combined with Hosemann paracrystalline structure factor let us to reproduce real small angle scattering profiles of the whole family of samples by modifying head to head and interlamellar distances estimated from the model simulated for each dopant molecule. Finally, the paracrystalline structure factor of a finite stack of layers we used in calculations was evaluated by fixing the value of the parameter N which describes the mean number of coherently scattering layers of dopant molecules separated by PANI layers. This parameter multiplied by the mean inter-lamellar spacing gives an estimation of the coherence length or the average crystallite size along the direction perpendicular to the layers. The value of the parameter N was estimated for each dopant to obtain the best agreement with the experimental curve *i.e*. the correct shape at the maximum of the profile. The coherence lengths calculated from the model are collected in the table D.3.4.2 and compared with the values obtained from the Scherrer equation ($\xi(Å) = \frac{0.9\lambda(Å)}{\Delta(rd)\cos\theta}$ with Δ = full width at half maximum of the peak). It can be noticed that for all doped polymers, the coherence lengths estimated both from the model and from

Scherrer equation are quite similar. In the majority of cases and especially in the better ordered systems ($PANI(DOEPSA)_{0.5}$, $PANI(DDeEPSA)_{0.5}$, $PANI(DDoEPSA)_{0.5}$, and $PANI(DBEEEPSA)_{0.5}$) the Scherrer equation gives slightly smaller values due to the fact that this type of analysis does not take into account distortions within the crystallites which of course affect SAXS reflection leading to its broadening. The two systems with shortest dopant molecules (DPEPSA and DBEEPSA) seem to be at the edge of applicability of the Scherrer analysis with only three coherently scattering layers and coherence lengths under 100Å. It should also be noted that only for these two shortest dopants the repetition distance is equal to or larger than twice the estimated length of an isolated molecule. This means that only for these two dopants there is no interdigitation of the flexible alkyl or alkoxy tails contrary to all other cases. The figure D.3.5 shows the full q range experimental SAXS profiles compared with the calculated ones. For all polymers studied, the first order dominant maximum is well reproduced. We also predicted theoretically a second order maximum which is visible on experimental scattering curves of $PANI(DPEPSA)_{0.5}$, $PANI(DOEPSA)_{0.5}$ and $PANI(DDEPSA)_{0.5}$. Some random intensity fluctuations especially for very small q values are due to the calculation method limitations (the calculated sum is not infinite).

Table D.3.4.1

Plastdopant	d (Å)	ρ_H-$\rho_{PANI(*)}$ (e/Å^3)	z_H (Å)	σ_H (Å)	ρ_T-$\rho_{PANI\,(*)}$ (e/Å^3)	z_T (Å)	σ_T (Å)	η_1	N
DPEPSA	28	0.035	11.5	2	-0.02	5	4.5	3	3
DOEPSA	33	0.035	12.5	2	-0.02	5	5	1.5	5
DDEPSA	35	0.035	15	2	-0.02	5	5	1.5	5
DDoEPSA	38	0.035	16	2.5	-0.02	5	5	1	5
DBEEPSA	29	0.035	12	2	-0.02	5	5	3	3
DBEEEPSA	31	0.035	13.5	2	-0.011	5	5	1	5

Table D.3.4.2

Plastdopant	Coherence length(Å)	
	Model	Scherrer equation
DDoEPSA	190	171
DDEPSA	165	146
DOEPSA	155	131
DPEPSA	86	98
DBEEPSA	87	110
DBEEEPSA	155	145

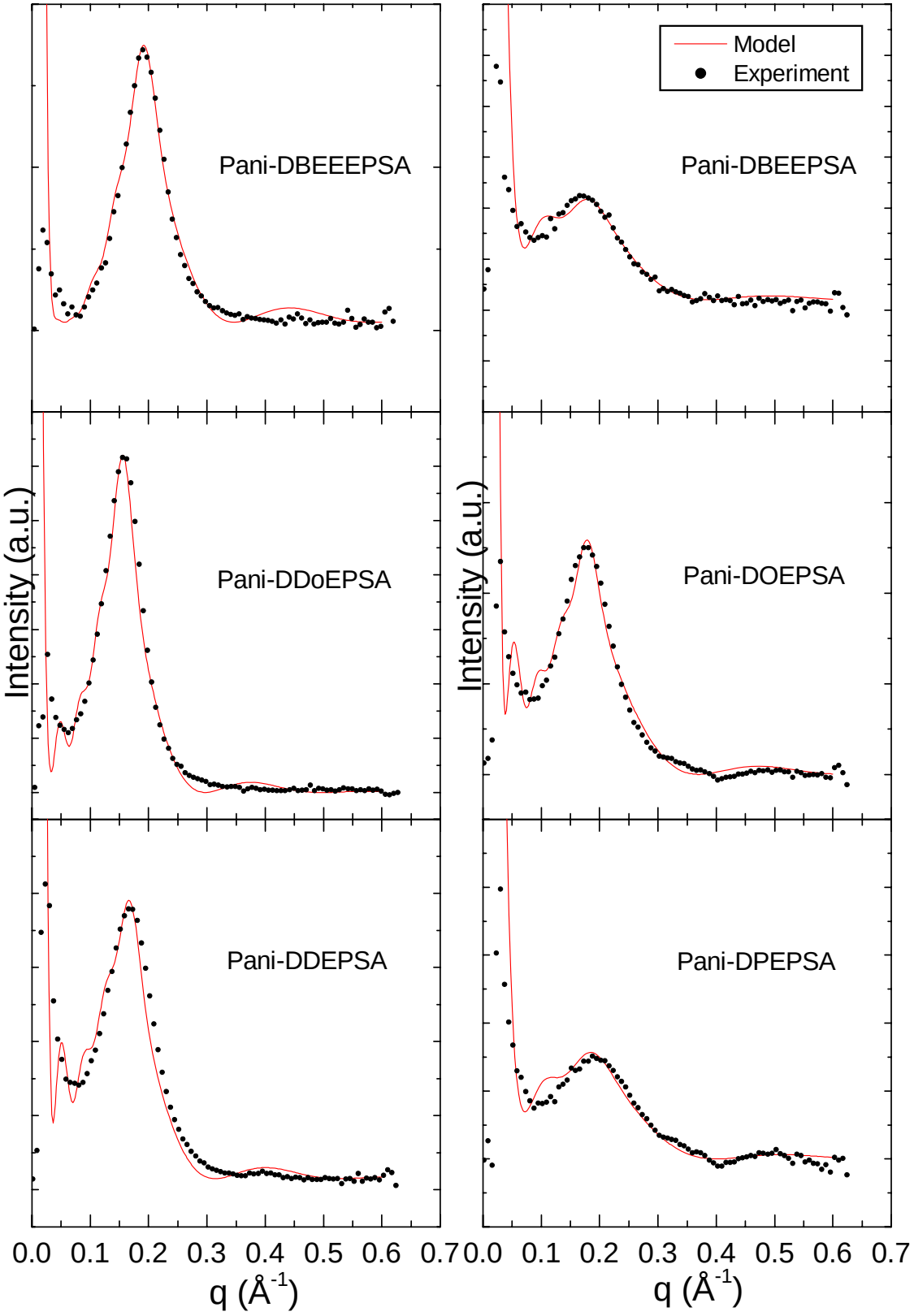

Fig.D.3.5 Calculated small angle X-ray scattering profiles compared with the experimental curves.

D.4 The evolution of the structural orientation in the film upon stretching

The structural studies of stretched samples were done for the films of polyaniline doped with second generation plast-dopants *i.e*. DDoESSA and DB3ESSA which exhibit much better mechanical properties compared to the films with first generation plast-dopants. The results for Pani/DDoESSA are presented in fig.D.4.1. The series of 1D WAXS scattering patterns in transmission and reflection were recorded for all the systems with various stretching ratio ranging from 0% (unstretched) to 170%. In addition, for more detailed studies of in plane structure, 2D small angle scattering patterns in transmission were recorded. The evolution of scattering patterns were deeply studied in terms of changes in crystallinity and diffuse scattering (amorphous halo), coherence length of ordered regions, average long period interlamellar distances, symmetry in the system, and finally orientation of ordered regions.

First of all, as it was shown in previous chapters the samples exhibit strong anisotropy between in plane and out of plane film structures. This anisotropy is generally more pronounced for second generation dopants compared to first generation ones. In the DDoESSA and DB3ESSA systems the anisotropy almost reaches 100% (in DDoESSA the peak at ~1.78$Å^{-1}$ is invisible in transmission; in DB3ESSA long period maximum at small q is very small). For this reason, we performed a more detailed analysis of structural anisotropy of stretched samples.

D.4.1 Analysis of WAXS results

Evolution of the diffraction peaks

Wide angle scattering profiles of stretched samples exhibit similar shape to these of the unstretched ones with dominating long period maximum at small q values (strongly dominating in transmission), one at 1.78$Å^{-1}$ (dominating in reflection) and a similar diffuse halo centered at 1.5 $Å^{-1}$. That suggests the same lamellar like model of structural organization proposed in chapter D.2 is still valid. In other words, stretching does not induce any structural phase transition but only modifies the characteristics of the same structure. However some indication of a broader maxima with a more diffuse character at 2θ ~7deg ~11deg d corresponding to the 7~10 Å distances observed in transmission may be related to higher indexed peaks (002) (003) of a long period distance (001) (Fig. D.4.1). As we will discuss it later, it may suggest a slight decrease of paracrystalline character of lamellar stacking

distortions after stretching. The intensities of those maxima are very small barely emerging from the background. (They maybe became only little more evident due to decrease of the first line width and slight shift to higher q values). Looking at the positions of the long period lamellar stacking maxima at small q on the WAXS profile of the film with DDoESSA, we observe a noticeable decrease of the lamellar stacking distance as a function of the stretching ratio (Table D.4.1 and Fig. D.4.2). In Pani/DDoESSA system the lamellar stacking distance decreases from ~39 Å before stretching to ~35 Å when stretched at 100%. This effect may be associated with some rearrangement of counterions alkyl tails leading to better inter-digitation and more densely packed structure. We should notice that such a ~10% change in lamellar repetition distance demonstrates the softness of the electrostatic potential as a function of the inter-lamellar distance. This is probably the main reason of paracrystalline character of stacking distortion and its changes upon stretching. It will be discussed in more details later. In Pani/DDoESSA system slight changes of the small angle peak position are accompanied with a smooth change of the peak shape. The peak profile becomes less Lorentzian or more Gaussian in shape (quite visible at the right wing of the peak while left wing is somewhat affected by the beam stop or presence of strong scattering at very low angles fig 4.2).

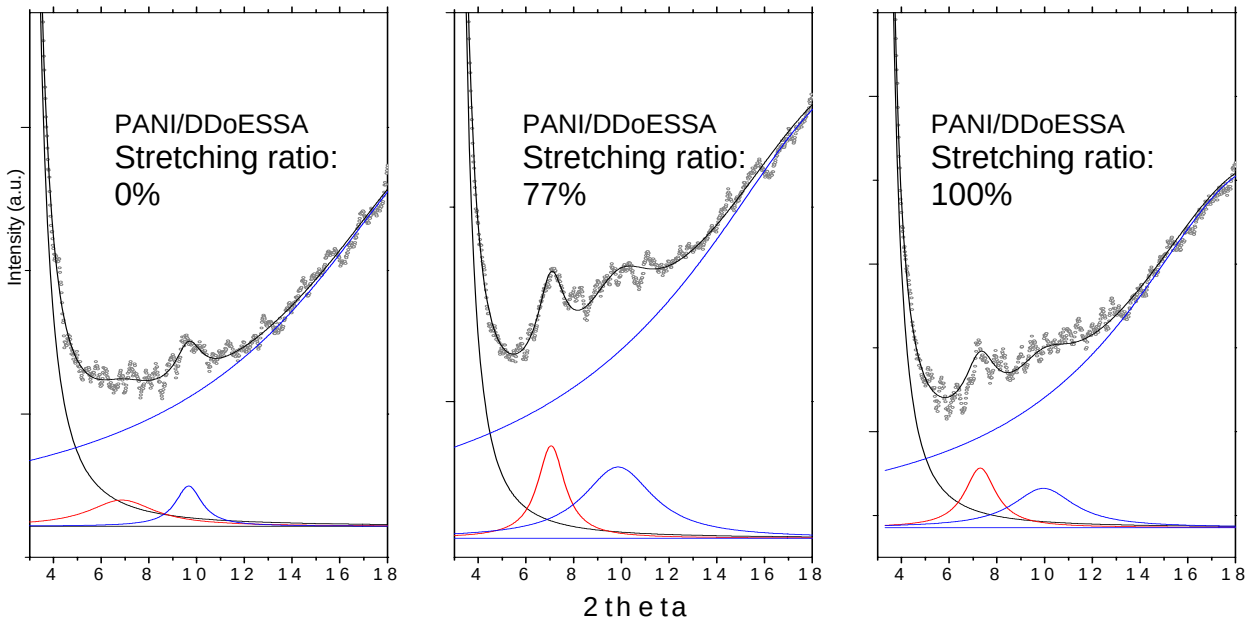

Fig D.4.1 intensity higher indexed peaks of long period distance to visible in PANI/DDoESSA in transmission

Table D.4.1

PANI-DDoESSA				
TRANSMISSION				
Sample	Crystallinity Index	First Bragg peak	Coherence length (Å)	Second Bragg peak
Unstretched	69%	2θ=2.25° d= 39.3Å	86Å	-
77%	62%	2θ=2.38° d= 37.1Å	86Å	2θ=7.17° d=12.3Å
100%	71%	2θ =2,48° d= 35.6Å	99Å	2θ =7.07° d= 11.8Å
REFLECTION				
Sample	Crystallinity Index	Bragg peaks	Coherence length (Å)	ntensity ratio (I1.6°/I2.5°)
Unstretched	50%	2θ =2.5°, 25.4° d=35.3Å, 3.5Å	56Å, 23Å	0.36
77%	45%	2θ =2.5°, 25.4° d=35.3Å, 3.5Å	85Å, 28Å	0,05
100%	47%	2θ =2.5°, 25.2° d=35.3Å, 3.5Å	74Å, 28Å	0.08

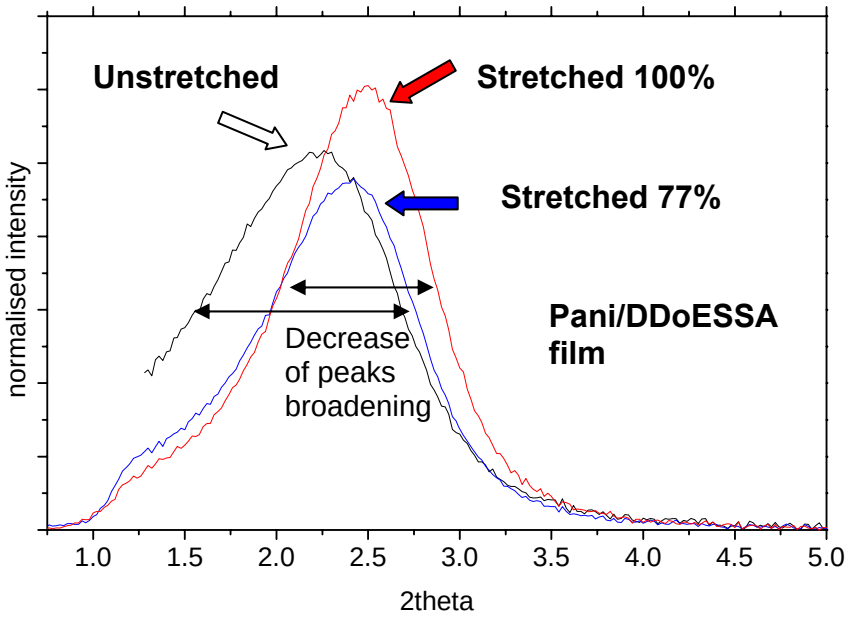

Fig. D.4.2 Evolution of small q first peak position as a function of stretching of DDoESSA doped polyaniline.

Concerning the maximum at 1.78 Å $^{-1}$ or at 25 degrees in 2θ that corresponding according to our model to the inter chain distance between stacked polyaniline chains ~3.5 Å,

we do not observe any change in the position of this maxima after stretching for every system. It seems to be clear since this interchain distance is strongly determined by unique interaction of phenyl ring π-orbitals in polyaniline chains and may be considered as a fixed value.(fig. D.4.3)

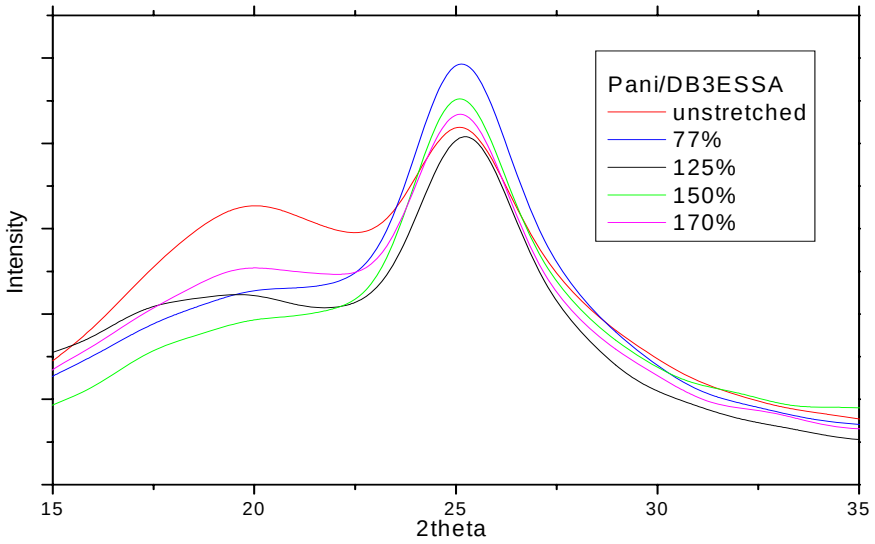

Fig. D.4.3 Characteristic maxima at ~25deg corresponding to pani chain stacking distance as a function of stretching ratio.

Coherence length of ordered regions and crystallinity index.

In Pani/DDoESSA films the analysis of the peak width FWHM of the first small angle maximum in transmission give the average crystallite size or equivalent coherence length of around 100 Å in the film plane and is not very sensitive to the stretching ratio. That corresponds to more or less 2 or 3 lamellar repeat distances in the crystallites. But when we compare this result with the crystallinity index estimated from the area under the same small angle maxima, which ranges between 60 and 70%, it would indicate that the average separation distance between crystallites can not exceed more than 1 or 2 inter-lamellar distances i.e. 35~70 Å. It is possible to imagine such inhomogeneous system with small crystallites separated by thin amorphous regions, but it is better and more realistic to speak in terms of coherence length in homogeneously disordered layered structure oriented in the plane of the film. From this point of view, one can consider continuous (in this order of magnitude) structure of repeated layers (relatively thin amorphous regions are treated as defects or lattice distortion). The correlations are visible only for the layers separated by the distances smaller than coherence length due to paracrystalline disorder. In such a case

broadening of the maxima is determined by structure distortion. The same studies of coherence length in the film of Pani/DB3ESSA system gives smaller value below 50%.

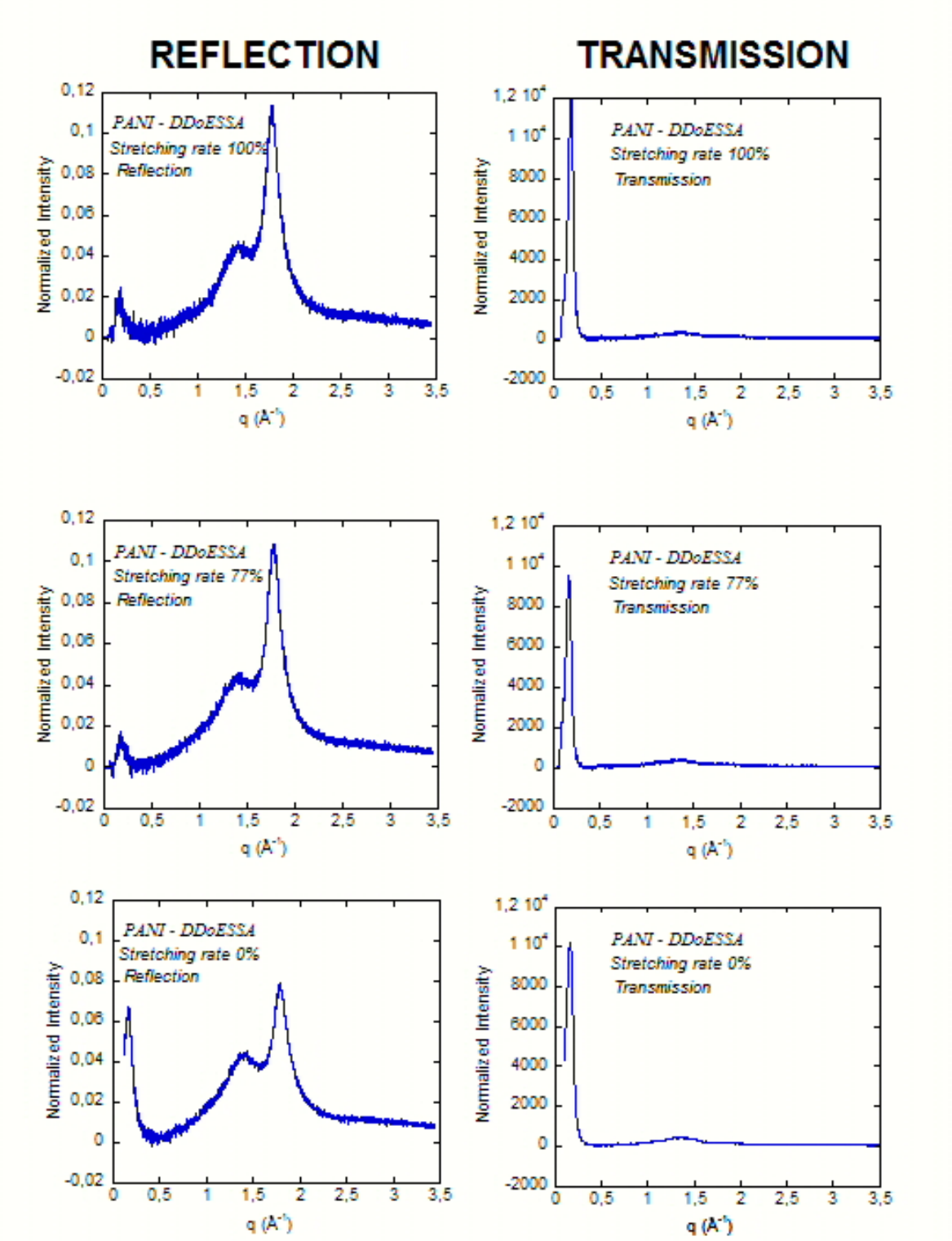

Fig.D.4.4 Comparison of WAXS patterns obtained in transmission and reflection for various stretching ratio of Pani/DDoESSA films

Orientation within the plane of the film

As we pointed out before, even unstretched films of plast-doped polyaniline exhibit strong anisotropy between in plane and out of plane structures. The analysis (comparison) of the diffraction profiles in reflection and transmission geometry obtained for various stretching ratio allow studying changes of this orientation effect upon stretching. In the case of PANI/DDoESSA film the decreases of relative intensity of first maxima at small q related to lamellar distance and increases of the intensity of maxima et q~1.78 $Å^{-1}$ related to polyaniline chains stacking are clearly visible (see fig. D.4.4). That would indicate an increase of the orientation of lamellae upon stretching. Possible mechanisms of changing the orientation of ordered regions within the plane of the film are schematically shown in fig.D.4.5. Rotations of crystallites marked with red arrows lead to an increase of in plane orientation, yellow arrow shows the crystallites reorientation leading to in plane orientation. We will discuss it later.

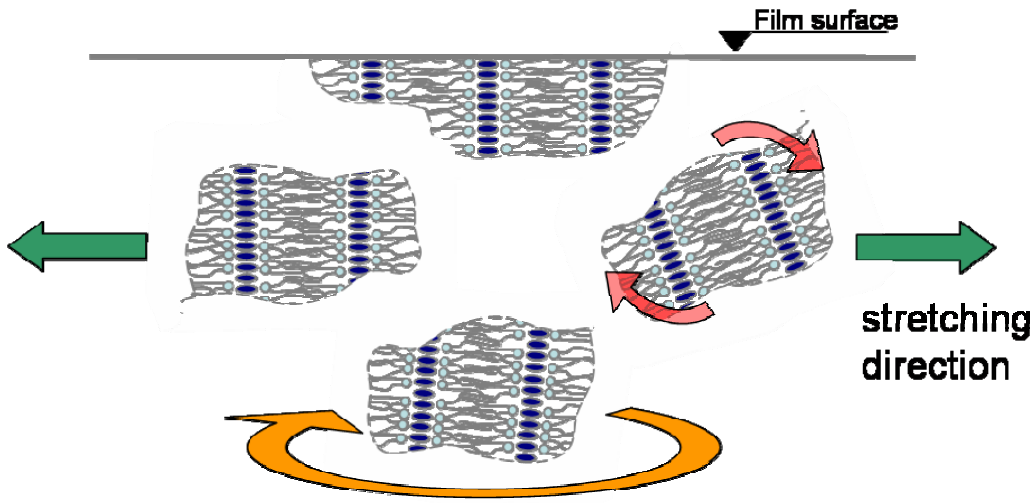

Fig.D.4.5 Possible mechanisms of changing the orientation of ordered regions upon stretching.

The Evolution of the diffuse halo.

The only smooth changes of amorphous diffuse halo are found upon stretching. However the direction of this evolution stays in good agreement with the model crystallite orientation changes upon stretching described above. As we described it in chapter D.1 the main source of diffuse scattering maximum at ~1.5 $Å^{-1}$ is a spatial correlation of disordered counterion tails. Generally, even in unstretched films, counterion tails are oriented more or less parallel to the film surface and along lamellar stacking direction. With the increase of degree of the crystallites orientation, upon stretching the counterions tails become also better packed. It is proved experimentally by the decrease of the relative intensity of the diffuse intensity in transmission (see Fig. D.4.6). In addition, a smooth decrease of the width of the diffuse maximum as a function of stretching is visible in reflection (see Fig. D.4.6). It would indicate slight increase of the counterion tails ordering. Indeed, we may expect such a feature strictly associated with decrease of the inter-lamellar distance. Finally, upon stretching "oriented amorphous" character of the counterion tails is even better pronounced.

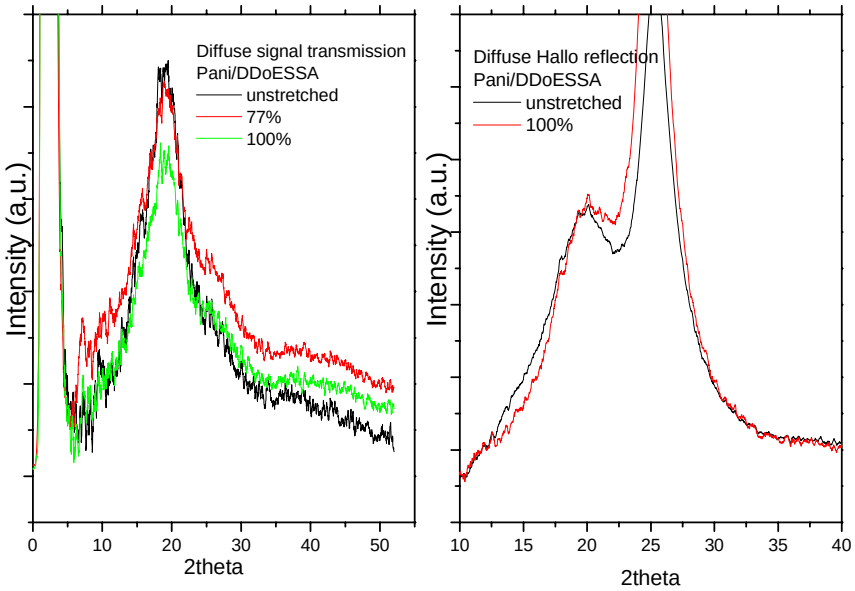

Fig. D.4.6 The evolution of diffuse signal upon stretching studied in transmission and reflection.

D.4.2 Analysis of SAXS results

In plane orientation 2D small angle scattering patterns

Two dimensional small angle scattering patterns in transmission geometry of unstretched and stretched films of Pani/DDoESSA and Pani/DB3ESSA with an indication of stretching direction are presented in Fig.D.4.7. The results of integration of 2D patterns with respect to the stretching direction are shown in Figures D.4.9, 10, 11 and 12.

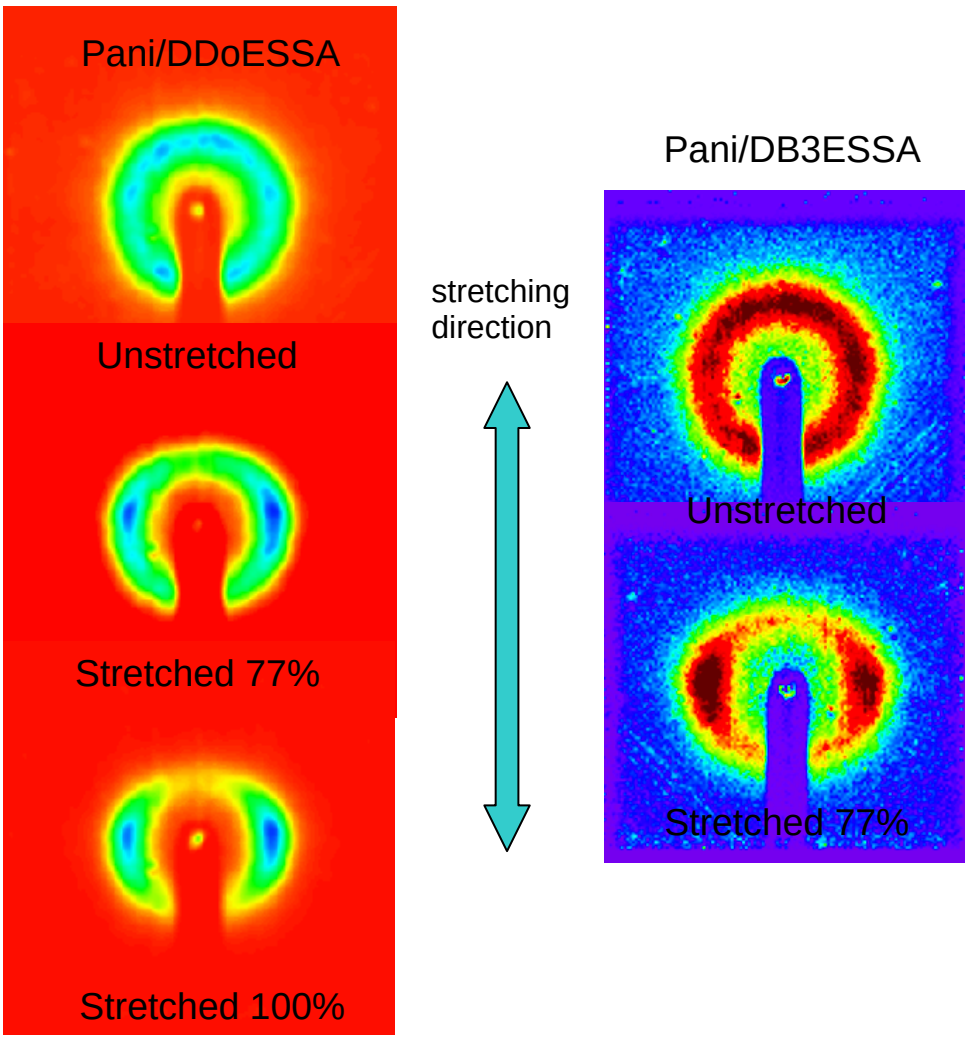

Fig.D.4.7 2-D SAXS profiles of Pani/DDoESSA and Pani/DB3ESSA as a function of stretching ratio

In general 2D SAXS profiles in transmission exhibit dominating ring of first order maximum. That indicates powder average of scattering planes orientation in the film plane. Only for DDoESSA doped samples some pseudo hexagonal orientation effect is observed as superimposed maxima on scattering profile. It has been discussed in the chapter D.2. Upon stretching, this situation changes dramatically. Strong orientation effect is observed as dominating peaks with a maximum intensity located on the axis perpendicular to the stretching direction (q vector orientation perpendicular to the stretching direction). Degree of this orientation depends on the stretching ratio what is clearly visible comparing 2D profiles of DDoESSA doped films stretched 77% and 100%. However even for maximum stretched samples we observed still small intensity of the same maxima on the axis parallel to the stretching direction (q vector along stretching direction). That would indicate that some part of the film exhibits still random orientation. The anisotropy of the film may be describe more quantitatively by introducing some anisotropy parameters. Simple way of defining an anisotropy parameter form scattering profile is following [87]

$$A = \frac{I_{hor} - I_{ver}}{I_{hor} + I_{ver}} \qquad \text{(D.4.1)}$$

Where, I_{hor} and I_{ver} denote the intensity at maximum of the horizontal and vertical cross section of the 2D pattern, respectively. Stretching direction is along vertical direction as indicated in fig. D.4.7. The parameter A tends to zero and unity for isotropic and fully ordered samples, respectively. Obtained values of orientation parameter A for different stretching ratios of Pani/DDoESSA and Pani/DB3ESSA are collected in table D.4.2. The orientation parameter A reach the maximum value 0.79 for 100% stretched Pani/DDoESSA system. It may be note that the same system exhibits also the biggest in-out of plane anisotropy before stretching (see chapter D.2) which increases clearly upon stretching. However, the 77% stretched film of Pani/DDoESSA has almost a twice smaller value of parameter A=0.42. That would indicate that the maximum orientation effect is achieved upon final stage of stretching process. In opposite even 170% stretched film of Pani/DB3ESSA has an anisotropy parameter A of only 0.43 much smaller than the best results obtained for DDoESSA.

Table D.4.2

Sample	Stretching ratio %	Anisotropy parameter A
Pani/DDoESSA	77	0.42
	100	0.79
Pani/DB3ESSA	170	0.43

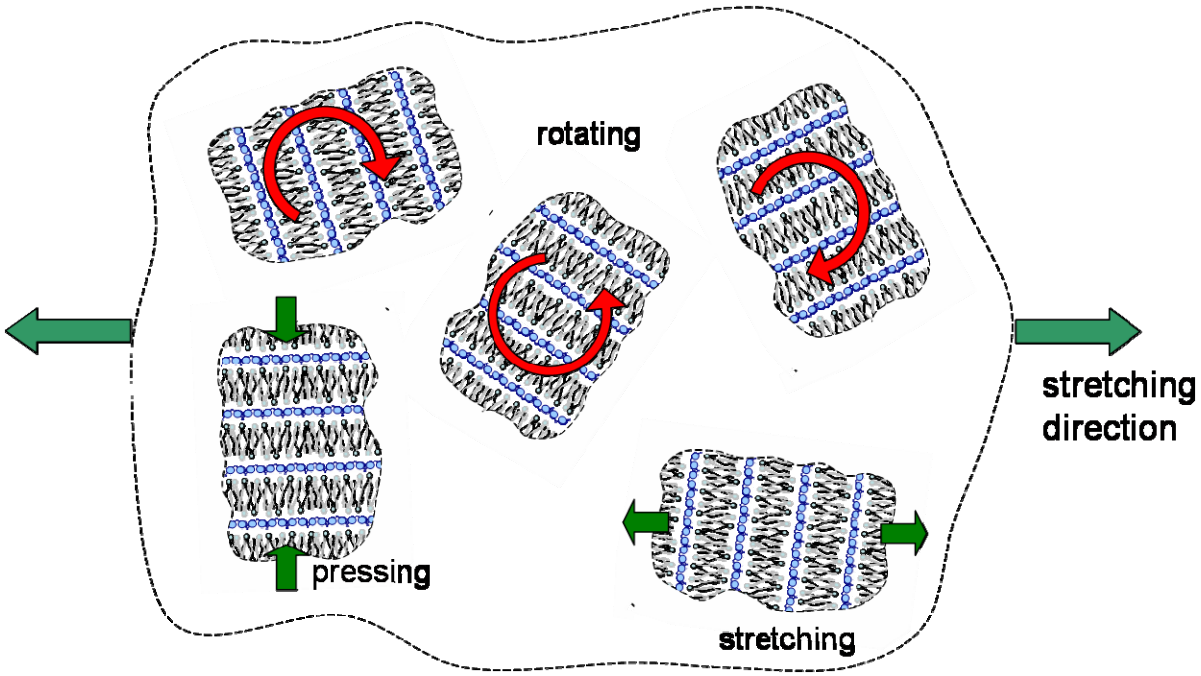

Fig. D.4.8 The various internal forces and moments possibly involved in the stretching process. View normal to the film plane.

The small angle maximum appearing on 2D patterns, accordingly to our model corresponds to long period lamellar distance between polyaniline chains stacks separated by dopant counterions. Generally, it is indisputably true that in stretched films the majority of long polymeric chains should prefer to be oriented along the stretching direction. In our case, the stacks of polyaniline chains stay perpendicular to the stacking direction of lamellae. As a consequence, after stretching we obtain the film with a real quasi-one dimensional in plane lamellar ordering (We should remember still about orientation imperfections within the film). Indication of pseudo hexagonal orientation exhibited by DDoESSA system disappears turning into a lamellar one. The lamellae are oriented in their majority perpendicular to the stretching

direction. The possibility to change the orientation of originally randomly oriented crystallites in the unstretched film depends strongly on their orientation with respect to stretching direction. The crystallites nearly oriented to the preferred orientation need less energy than the others. The crystallites oriented along the stretching direction are difficult to orient since they must be rotated around the axis normal to the film plane of an angle close to 90 degrees. That is why stretched films exhibit still no perfect 100% orientation. The various internal forces and moments possibly involved in the stretching process are shown in Fig.(D.4.8). In general interplay of internal forces lead rotational moments that change the orientation of crystallites. But considering the crystallites oriented along and perpendicular to the stretching direction, upon stretching they are mainly stretched and pressured respectively. That would suggest some changes in inter-lamellar distances upon stretching. Indeed, on WAXS profiles in transmission slight changes in the inter-lamellar distance, especially in DDoESSA system are observed. The series of 1D profiles obtained by integration of 2D SAXS patterns were made. The integration of the patterns carried out with respect to the stretching direction allows performing detailed studies of the evolution of the small angle peak position. The analysis of the SAXS profile perpendicular to the stretching direction gives similar results to those obtained from WAXS in transmission but less pronounced (see Fig.D.4.9). In the opposite direction, analysis of the SAXS profile along the stretching direction reveals a shift of the maxima to smaller q values that indicates an increase of the inter-lamellar distance (Fig (D.4.10)) as we may expect by analysing internal forces upon stretching process (Fig.(D.4.8)). The comparison of the SAXS profiles with opposite orientation of q vectors of 77 and 100% stretched DDoESSA system is presented on Fig.(D.4.11). The same comparison for Pani/DB3ESSA film is presented on Fig.(D.4.12).

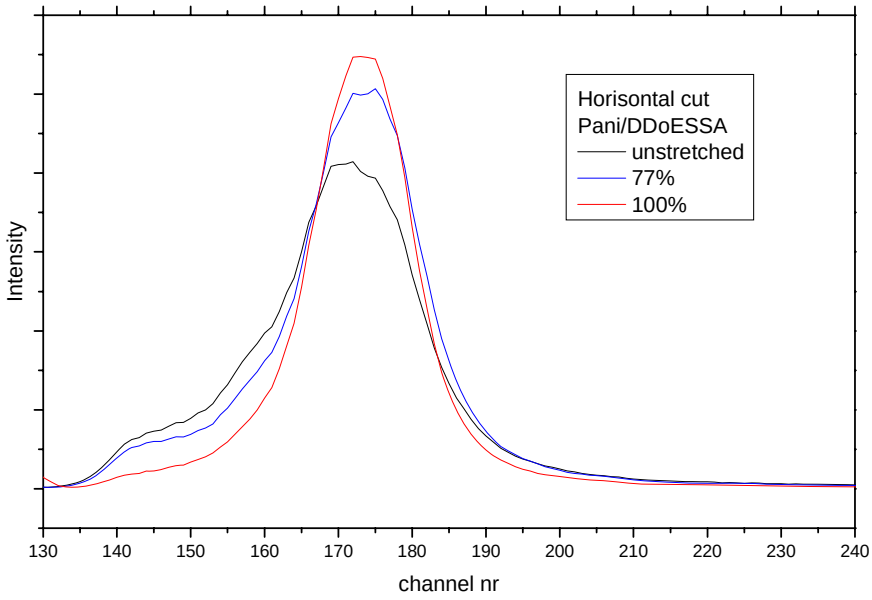

Fig.D.4.9 SAXS profiles perpendicular to the stretching direction (horizontal integration)

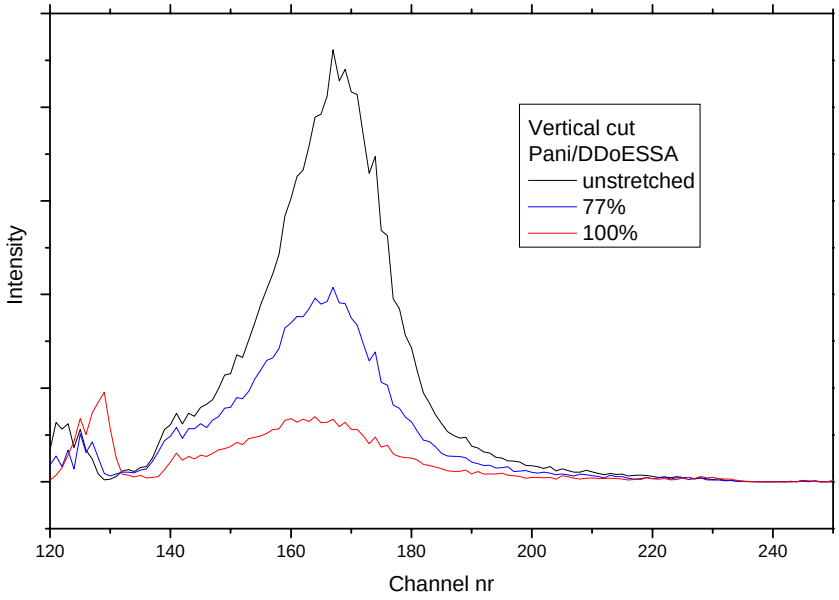

Fig.D.4.10 SAXS profiles along the stretching direction (vertical integration)

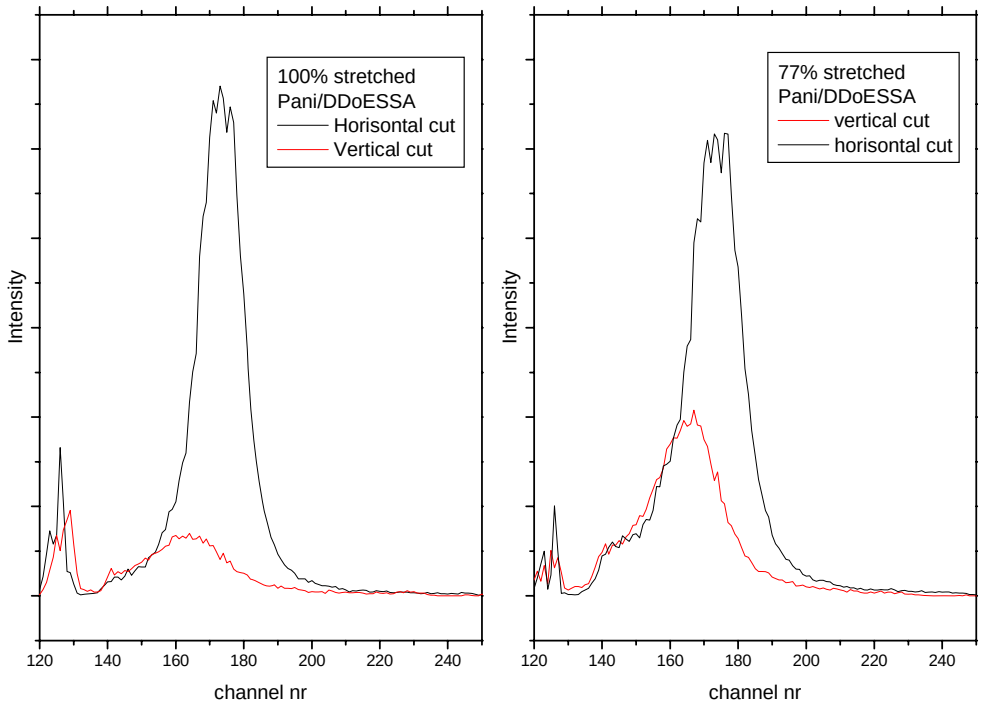

Fig.D.4.11 Comparison of the SAXS profiles obtained by integration in opposite directions for different stretching ratio of Pani/DDoESSA

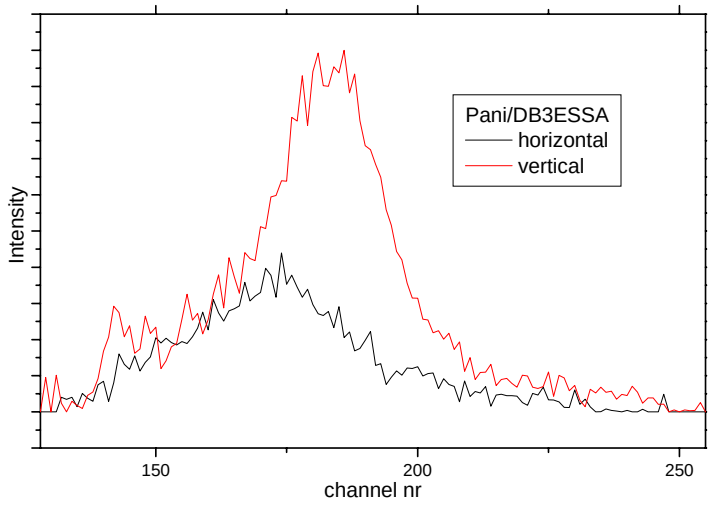

Fig.D.4.12 Comparison of the SAXS profiles obtained by integration in opposite directions for 170% stretched Pani/DB3ESSA

Discussion

The observation of real changes of interlamellar stacking distances after stretching (decrease or increase in perpendicular or parallel to stretching direction respectively) leads to the assumption that the stacking of the system is really soft like foam. Relatively rigid layers of stacked polyaniline chains are separated by soft counterions medium. It will be confirmed in next chapters by dynamics studies. In such a system the potential energy as a function of the distance between stacks of polyaniline do not change rapidly in a relatively wide range allowing wide distribution of inter-lamellar distances depending on the soft counterion tails configuration (degree of inter-digitation, density of packing). The potential energy well is broad and flat at the bottom instead of classical harmonic or Morse approximation. Wide distribution of possible inter-lamellar distances leads to paracrystallinity in the system. By pressing or stretching the crystallites we introduce some additional energy to the system that allows smooth changes in the inter-lamellar distance by moving it closer to the left or right wall (side) of the energy well. We should notice that this modification of lamellar distances likely changes the local density in the system, since mostly one dimension is changing. Polyaniline chains are not significantly elongated except maybe in PANI-DDoESSA for which stretching the film has the consequence to suppress the pseudo-six fold symmetry proving that the chain defects are cured upon elongation. In any case, no change in chain stacking distance is observed. In addition a decrease of the paracrystalline character of the distortion is expected. Indeed we observe the decrease of FWHM and change of the shape (see Fig.(D.4.2)) of dominating first maximum and indication of higher order maxima in DDoESSA system (see Fig.(D.4.1)). That would indicate an increase of the coherence length due to the decrease of paracrystalline character of the distortions or an increase of average crystallite sizes. In addition to all the previous considerations, it is worth to remark that the shifts of the peak can also be due to changes of the paracrystalline disorder itself in the system. Indeed, according to the paracrystalline theory, positions of diffraction peaks by paracrystals are not really periodic. Peaks shift to lower q compared to those theoretically expected by the average lattice constant. The shift increases with increasing degree of disorder [88]. That is consistent with the results of structure minimisation where smaller lamellar distances than predicted from classical Bragg equation are systematically observed. The same simulated lamellar distances used in computation of Caillé structure factor which takes into account the paracrystalline disorder are giving good agreement with scattering experiments. (see chapter D.3)

D.5 Dynamics

D.5.1 Elastic scans

A good way to obtain an overall view of the dynamics under interest is to record and inspect carefully the evolution of the intensity of incoherent elastic scattering of neutrons as a function of the temperature.

Elastic neutron scattering in so-called fixed energy window measurements have been performed on first generation: Pani/DB3EPSA, and second generation: Pani/DDoESSA systems on the backscattering spectrometers IN10 and IN13 (respective energy resolutions (characteristic times) : 1μeV(10^{-9}s) and 8 μeV(10^{-10}s)). In these experiments only the neutrons which are elastically scattered by the sample are recorded in the detectors. The scattered intensity is proportional to the elastic intensity multiplied by the so-called Debye Waller factor $e^{-Q<u^2>/3}$ due to the brownian motion of protons. $<u^2>$ is the mean square displacement of protons and increases with the temperature. When the logarithm of the intensity is plotted as a function of temperature without any other contribution a straight line is obtained. As soon as the contribution of another type of motion becomes comparable to the energy resolution available on the spectrometer the measured elastic intensity decreases and the curve shows an inflexion point [89]. The obtained results for only one value of the momentum transfer are displayed in the figure D.5.1.

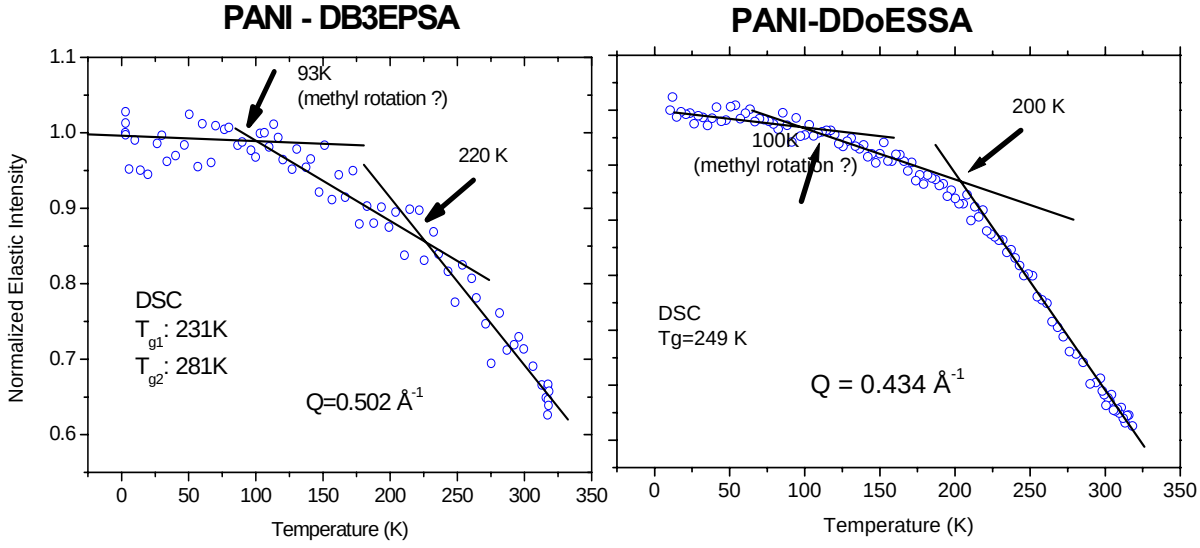

Fig. D.5.1 Elastic scans

At very low temperatures, the curve linearly decreases in intensity due to the contribution of the Debye Waller factor. Around 100K a first movement is observed, which can be attributed to the methyl groups rotation. More importantly, around 200(220)K another inflexion point, denoting the appearance of another movement is observed. This contribution can be assigned to the motion of alkyl chains of the counter-ions [90]. On the Fig.(D.5.2) is reported the variation of the electrical conductivity of the film measured at zero-frequency (DC conductivity). It can be remarked that in the same temperature range the dynamical transition and an insulator-metal transition are occurring, as well as the glass transitions Tg or Tg_1. In other words, by comparing results from all these techniques, we can follow simultaneously the stiffening of the lattice and the electronic localization.

The Fig. (D.5.2) presents the experimental elastic scan another way. Indeed, it is always possible to write the dependence of the elastic intensity as a function of the temperature as follows:

$$I(T) = I(0)\exp(-Q^2 < u(T)^2 >) \qquad \text{(D.5.1)}$$

In the previous expression $< u(T)^2 >$ is the mean square displacement of the scattering nuclei. It is straightforward to obtain the variation of this last quantity as a function of the temperature once that of the elastic intensity has been experimentally measured.

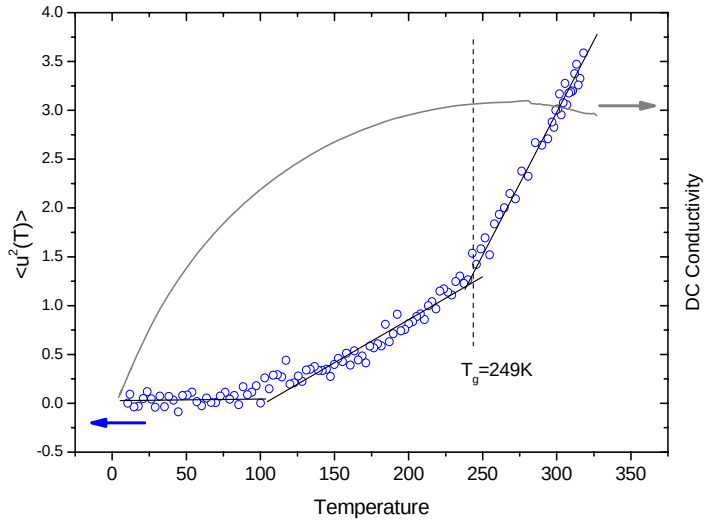

Fig. D.5.2 <u^2> representation of the elastic scan with a comparison with the DC conductivity curve

D.5.2 EISF analysis in various time ranges

0.1 to 50 ps time range

The first step in the analysis of incoherent quasi-elastic data is the extraction of the experimental values of the Elastic incoherent structure factor EISF. The EISF was evaluated from the fraction of so determined elastic intensity over the total integrated intensity within the quasi-elastic region, after the refined inelastic background had been subtracted. We estimated the error on the EISF values of the order of 1%. Values for Pani/DEHEPSA, Pani/DPEPSA and Pani/DB3EPSA are presented in figure D.5.3 at several temperatures. Important features can be noticed by a direct inspection.

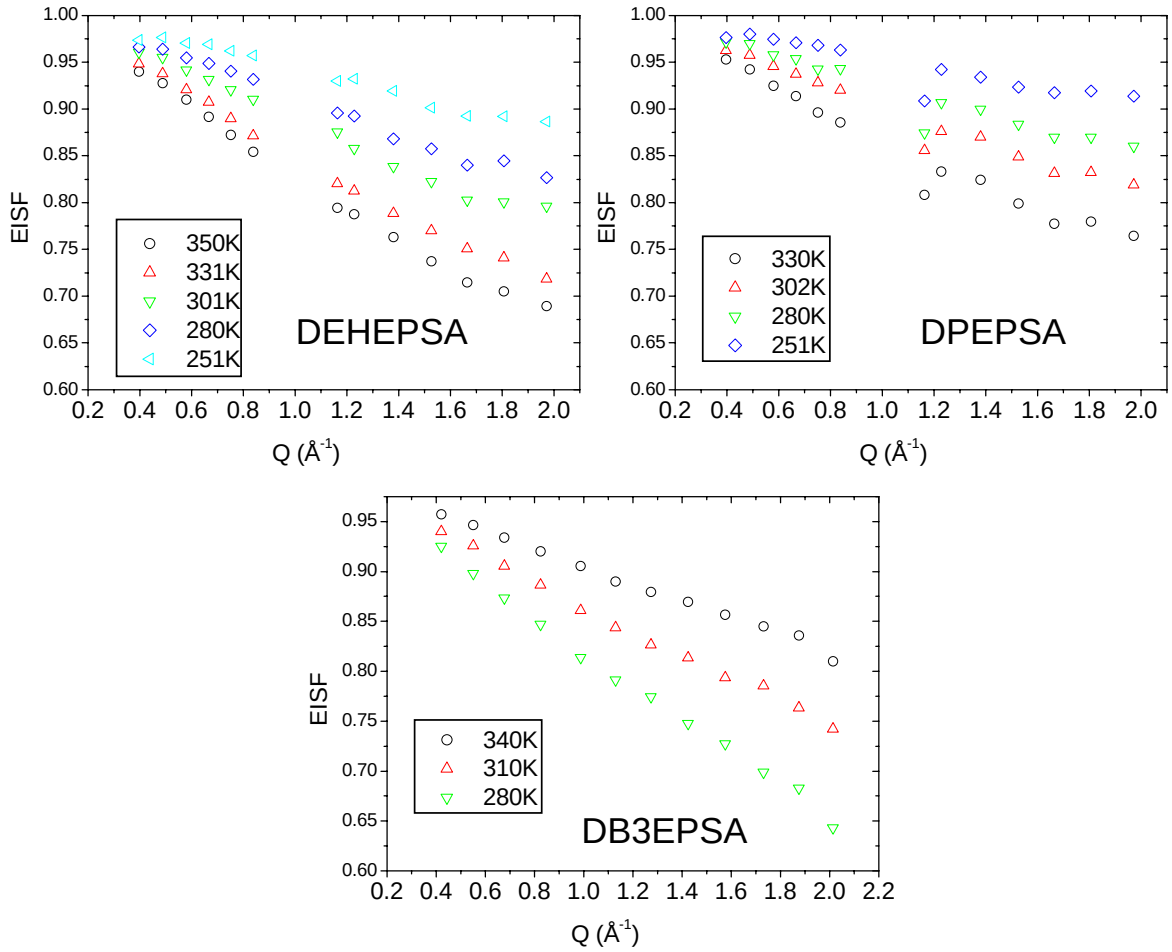

Fig. D.5.3 Elastic incoherent structure factor for various first generation dopants as a function of the temperature

For all the compounds, EISF values are strongly temperature dependent. Fig. D.5.3 shows that for a momentum transfer $Q = 2$ Å^{-1}, the amount of purely elastic scattering in the spectrum obtained with Pani/DEHEPSA increases from 0.72 to 0.89 when the temperature is decreased from 331 to 251 K. Similarly with Pani/DPEPSA (DB3EPSA) an increase of the EISF from 0.76 (0.63) to 0.91 (0.96) is observed at the same value of Q over the 251 – 330 K (280-340K) temperature range. That is an immediate indication of a continuous variation of the range of space accessible to the scatterers when the temperature is changed. Consequently, any model attempting to describe the chain dynamics must account for other displacements than motions which would be well defined geometrically like methyl rotations or reorientations of parts of the chain about chemical bonds.

Another important point concerns the difference between the EISF values obtained with the various compounds. At any temperature the values for Pani/DB3EPSA and Pani/DEHEPSA lie definitively below the corresponding results for Pani/DPEPSA. These observations are in themselves an experimental confirmation about the assignment of the quasi-elastic broadening to the dynamics to the alkyl chains of the counter-ions. That difference between Pani/DEHEPSA and Pani/DPEPSA can be attributed to the presence of a lateral ethyl group on the ending chains of DEHEPSA with respect to DPEPSA which tends to make the atomic packing less dense. Moreover there is one more CH_2 group on the main chain of DEHEPSA which make it more flexible. Similar observations were made in the past with a series of copper alkanoates [91] [92]. Similarly, DB3EPSA consists of much longer tails with oxygen situated along the chains which make it more flexible than both DEHEPSA and DPEPSA.

Model of local diffusion of protons in spheres

We tried to better characterize the chain displacements. Actually the motion of a particular hydrogen atom attached to a carbon of the alkyl tail results from the deformations of the tail skeleton, providing that the latter is flexible. Trying to envisage all possible configurations of each chain is quite hopeless, and would involve too many parameters. So a simple model was used. The motions of each proton along the chain were considered as displacements restricted into a small volume. The latter was approximated as a sphere and the model proposed by Volino and Dianoux [93] was used. Actually, many considerations led us

to envisage that model. Among them we shall mention the observation that the width of the quasi-elastic broadening was nearly constant as a function of the momentum transfer. Another hypothesis was envisaged where the counter-ion chains behave as rigid oscillating objects. Such a description was used in the case of liquid crystals or for chains attached to a substrate. However the presence of a diffuse signal in the x-ray scattering patterns suggest that the chains are unlikely well packed (see chapter D.2), especially above the dynamical transition and that they are able to adopt different conformations.

The mathematical form of the corresponding scattering law, $S(Q,\omega)$ is rather complicated even if only the sphere radius, R is involved. But the EISF is simply given by:

$$EISF(Q) = \left[\frac{3 j_1(QR_m)}{QR_m} \right]^2 \qquad \text{(D.5.2)}$$

in which $j_1(QR_m)$ is the first order spherical Bessel function. In our case a larger mobility was suspected for the atoms located near the chain end. So the values of the radii of the spheres were distributed along the alkyl chain. In the same time, steric effects required to introduce a limiting value for the radius as a function of the distance from the origin situated on the first carbon of the alkyl chain. Also considering the conclusions of Carpentier *et al* [92] we had to take into account a larger rigidity of the chains near their origin. The radii distribution was chosen to be given by the incomplete gamma function whose shape can evolve significantly to follow the previous prescriptions. Depending on the sample under study, six, ten or twelve sites were considered each weighted by a coefficient proportional to the number of protons attached to it. The numbering of the atoms is indicated in Fig.(D.5.4). In order to minimize the number of parameters, no particular dynamics was considered for the ending methyl groups. Following the conclusions of a previous study with camphor sulfonic acid [5], the model assumed the polymer chains to be immobile (on the instrument time-scale). Similarly, the displacements of hydrogen atoms on the benzyl group were considered small enough to be neglected.

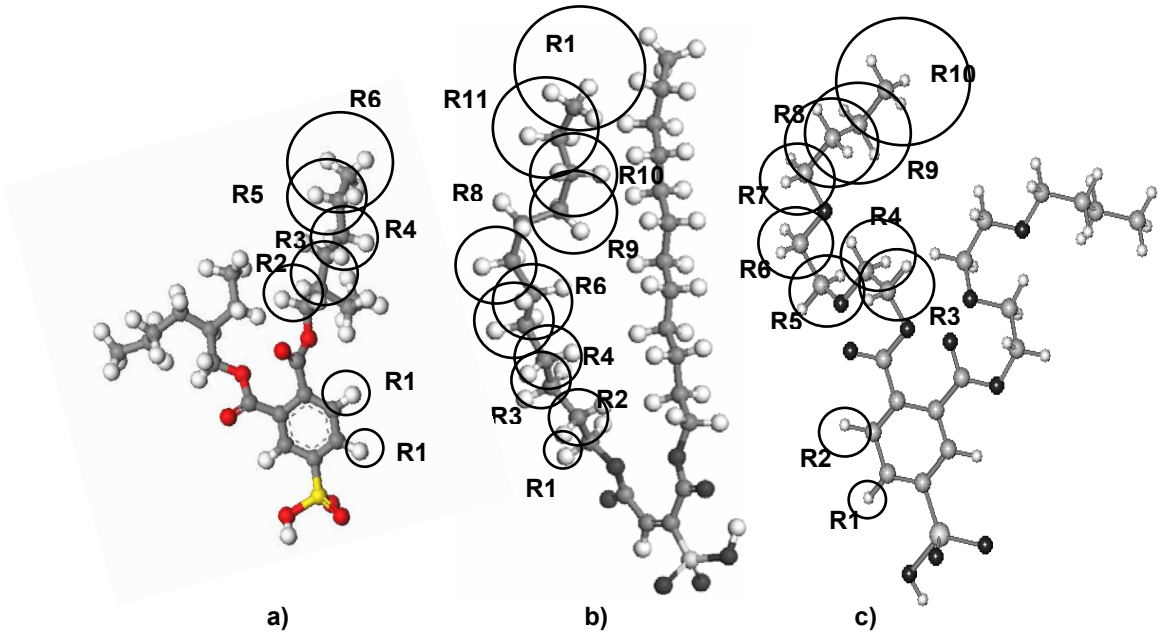

Fig. D.5.4 Chemical formulae of a) DEHEPSA b) DB3EPSA and c) DDoESSA. The labels of the sketched spheres correspond to those reported in figure D.5.6.

All the spectra recorded at the same temperature over the whole Q range were refined simultaneously, using only three relevant parameters. Two of them were used for the distribution function. The first one, R_∞, was giving a superior limit of the radii, the second one, a, the shape of the gamma function $\Gamma(a, x)$ (see Fig (D.5.5)), and the third one, s, the step interval for sampling values. Then the different radii were given by the expression:

$$R_m = R_\infty.\Gamma(a, ms) \qquad \text{(D.5.3)}$$

Where:

$$\Gamma(a,x) = \int_0^x t^{a-1} e^{-t} dt \qquad \text{(D.5.4)}$$

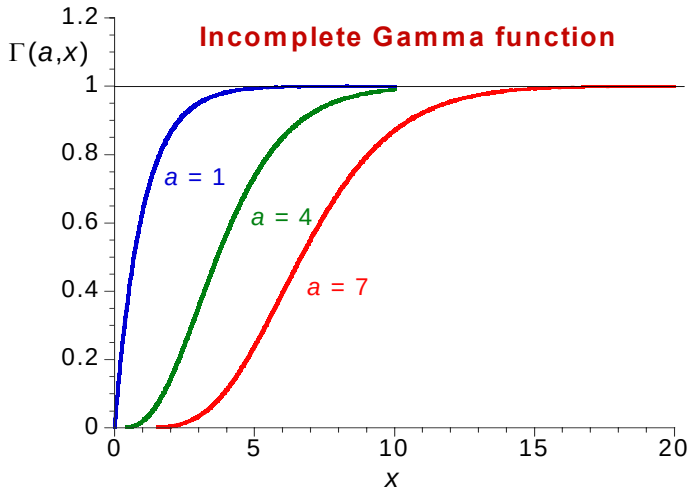

Fig. D.5.5 Different shapes of incomplete Γ function for various values of parameter a

The fitted EISFs for Pani/DEHEPSA Pani/DB3EPSA and Pani/DDoESSA are reported in the Fig. (D.5.6) for all the temperatures. In spite of its crudeness our sphere model is able to reproduce the part of elastic intensity even if slight discrepancies are observed in the low Q range. The different radii of the spheres explored by the hydrogen atoms can be easily evaluated from the fit parameters. These values are reported in the same figure , as a function of the position of the considered carbon along the chain together with the shape of the corresponding gamma function. Clearly the fit is not perfect, and the experimental spectra are not perfectly reproduced in the wings of the elastic peak, especially at large Q values and for the highest temperatures of measurement. However considering the restricted number of parameters in use the agreement can be considered as satisfactory.

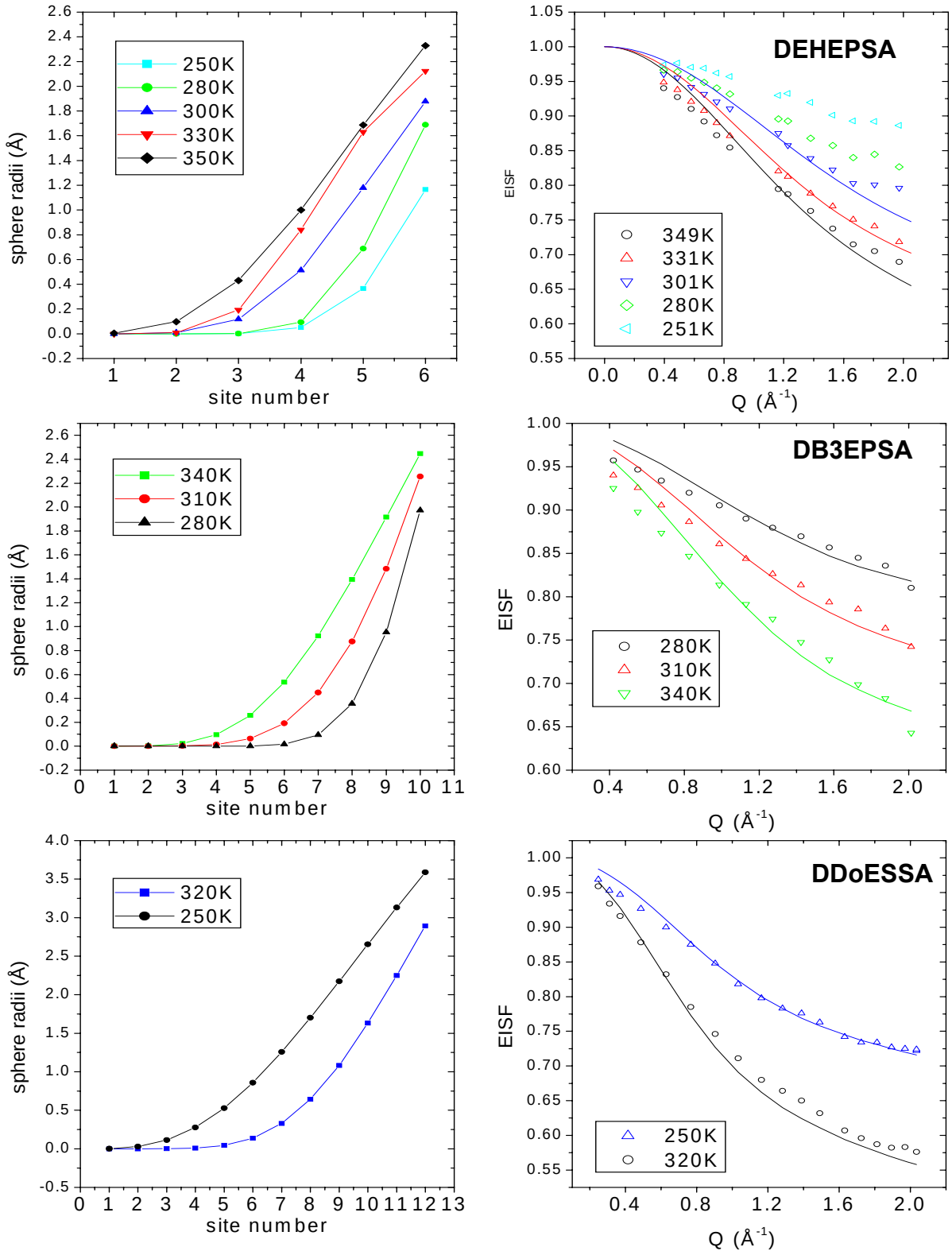

Fig. D.5.6 The radii of spheres (left) extracted EISF fitting (right) as a function of temperature for various dopants

We are aware that our description is a crude approximation of the counter-ions dynamics. Especially we did not include the methyl rotors contributions in order to reduce the number of parameters. Also, in the case of the DEHEPSA counter-ion, a similar dynamics was attributed to all hydrogen atoms numbered 3, whatever they belong to a methyl or a CH_2 group. Considering the values of the radii, the ending lateral CH_3 group is likely more mobile than the CH_2 group imbedded in the chain. Also, we did not consider the eventuality that the aliphatic chains of the counter-ions undergo conformational changes about their different C-C bonds. Such reorientations would induce large displacements of the protons linked to the carbon skeleton, which would contribute to decrease the EISF in the low Q region. These motions are likely to occur on a slower time-scale than the local displacements of the hydrogen along the chains. Taking them into account would require the introduction of a second characteristic time which would certainly improve the fit in the wings of the elastic peak, but which would noticeably increase the intricacy of the model.

In the Fig. (D.5.6), it can be seen that the protons which are lying closer to the heads of counter-ions are not mobile while those situated at the ends of tails are exploring a large surrounding space. With both compounds, below T = 331 K the hydrogen atoms linked to the carbons numbered 1 and 2 are immobile. That confirms our starting hypothesis according to which the hydrogen atoms of the benzyl groups were blocked. Noticeable displacements appear at the level of carbon 3 and their amplitudes increase with temperature. Considering carbons lying closer to the end of tails, a larger region of space seems also to be explored with DDoESSA than with DB3EPSA and with DEHEPSA, for a same temperature. A striking correspondence can be observed between the values obtained for carbon 4 and 5 of DPEPSA with those for carbon 5 and 6 of DEHEPSA. Such a behavior let us think that confinement effects are particularly important in the dynamics of these systems. The presence of an ethyl group strongly hinders the displacements of the first carbons on the DEHEPSA chain. In the same time, the similarity pointed out for ending carbons of both compounds suggests that the chain motions depend on its flexibility.

0.1 ps to 1 ns time range

The Fig. (D.5.7) shows as an example, the EISF recorded for Pani/DDoESSA at 300K with the four different spectrometers. The experimental EISF's appear to have very close values whatever the spectrometer *i.e.* whatever the energy resolution of the experiment ! This feature was obtained for all the temperatures. Such a result could be interpreted by assuming

that in these different time windows different localized motions are observed. In our opinion, this interpretation can be ruled out because in a previous work carried out on PANI doped with camphor sulphonic acid [5], it has been shown that in the whole time range (10^{-13} to 10^{-9} s) the PANI chains dynamics is only elastic in character. This fact has been established by comparing the results obtained on full hydrogenated samples and on partially deuterated PANI chains. An alternative explanation which is, in our opinion much more likely, may consider that the characteristic times of the dynamics involved in these systems are very broadly distributed. In other words, hydrogen atoms of the counter-ions and especially those being on the flexible tails are experiencing motions with similar geometry but at very different time scales. In such a case, it appears that the only analysis of the EISF is limited since as illustrated by the figure D.5.7, whatever the considered time range the Q variation does not change too much. In some extent we are dealing with a system whose dynamics might be characterized as a "fractal" one. In order to try to better understand this puzzling situation, we decided to investigate the intermediate scattering function to obtain a more contrasted view of the dynamics as a function of the time.

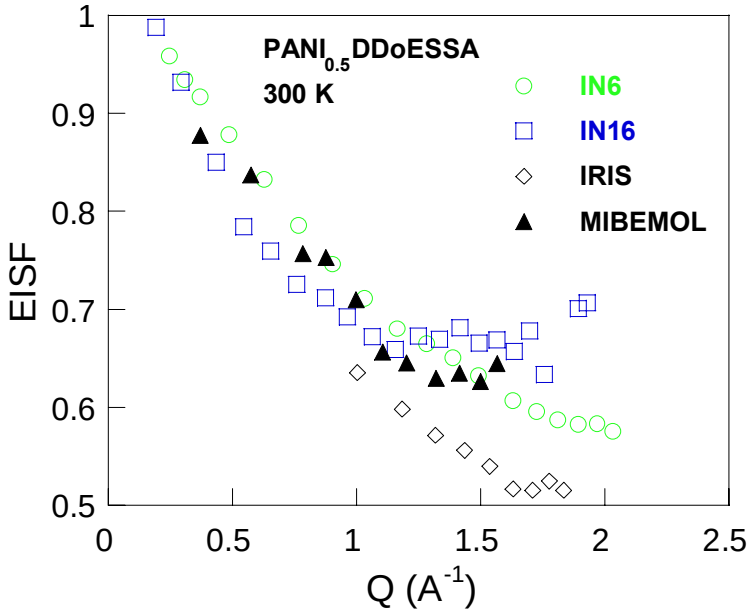

Fig. D.5.7: Experimental EISFof Pani/DDoESSA extracted at 300K on the four spectrometers.

D.5.3 Analysis of intermediate scattering function *I(q,t)*

Analysis of the intermediate scattering function

As already mentioned, in order to obtain the intermediate scattering function, the Fourier Transform of the incoherent scattering functions has to be carried out. It should be noted that in this operation, the calculated intermediate scattering function is automatically normalized to one at $t = 0$. In order to reduce as much as possible the random character of the amplitude correction of these functions when connecting them to each other in the different time windows, we started by doing such a transformation to the very low temperature spectra for which the scattering can be considered as purely elastic in character. The relaxation function obtained was then considered as the reference to which all the other functions obtained at higher temperatures have to be renormalized. Moreover, concerning the data obtained on time-of-flight spectrometers, they were systematically corrected in order to recalculate them as if they were obtained at constant **Q** as is the case with the backscattering spectrometers.

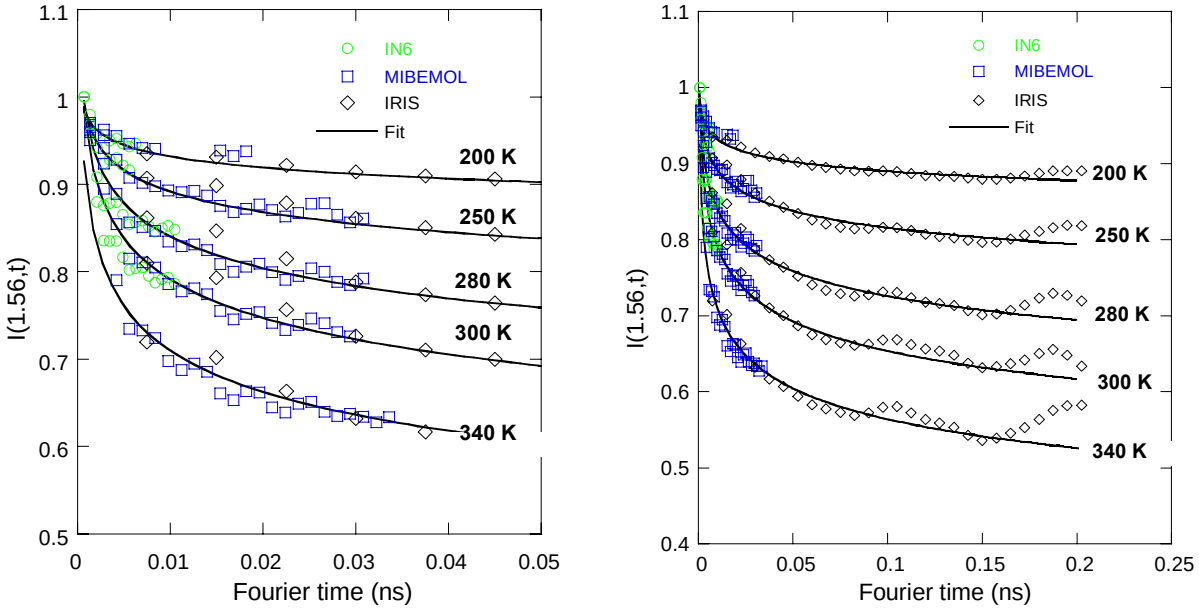

Fig. D.5.8 Intermediate scattering function for Pani/DB3EPSA at <Q> = 1.56 Å^{-1} as deduced from measurements performed on three different spectrometers shown in the short times range (left) and the whole time range (right).

The results obtained for the two samples at one value of Q (common to the four spectrometers within an error smaller than the **Q** resolution) and different temperatures are shown in the figures (D.5.8) and (D.5.9). The full lines shown in these figures are the results of a fitting procedure involving a simple time power law as detailed in the table D.5.1. In that table are also reported the evolution of the fitting parameters as a function of the temperature. Other attempts to fit these data by using stretched exponential functions as usually encountered for glass forming polymers [94] have not been successful. These attempts gave both unphysical values of parameters and very poor quality fits. It is well known that in complex systems the relaxation function may often obey such power laws with an exponent whose value lies between 0 and 1 [95][96][97]. For such systems different authors have shown that a convenient way to account for the relaxation function is to use a mathematical approach based on fractional calculus [98]. In particular, Schiessel and Blumen [99] have shown that for short polymers below entanglement point such an analysis can apply quite well. Even more generally, considering complex systems in which a large population of interacting units exist within a quite crowded environment, often due to a certain degree of confinement, the global behavior of the relaxation functions are similar to that of our systems. This has been recently proposed in a study of dynamics of proteins [100]. In our case, short chains are in strong interaction with "molecular walls" made of the layers of stacked PANI chains. Thus, our measurements show that the hydrogen atoms can not experience long range diffusion and are compelled to be in strong inter-relation with their nearest neighbors. Such a structural situation is very reminiscent of those evoked in [99] for example. At this stage, we can not go beyond such a qualitative discussion. Some work is still necessary in order to establish to what extent the above mentioned approach can be applied to our problem or at least to be able to connect our numerical results to more precise physical concepts.

Table D.5.1

Fitting function $I(Q_0,t,T) = I_0(1+\xi.T) * t^{-\alpha(1+\beta.T)}$				
	I_0	ξ (K^{-1})	α	β (K^{-1})
PANI/DB3EPSA	1.485	-0.0021	0.104	$-5.8.10^{-4}$
PANI/DDoESSA	1.684	-0.0027	0.323	$-5.2.10^{-3}$

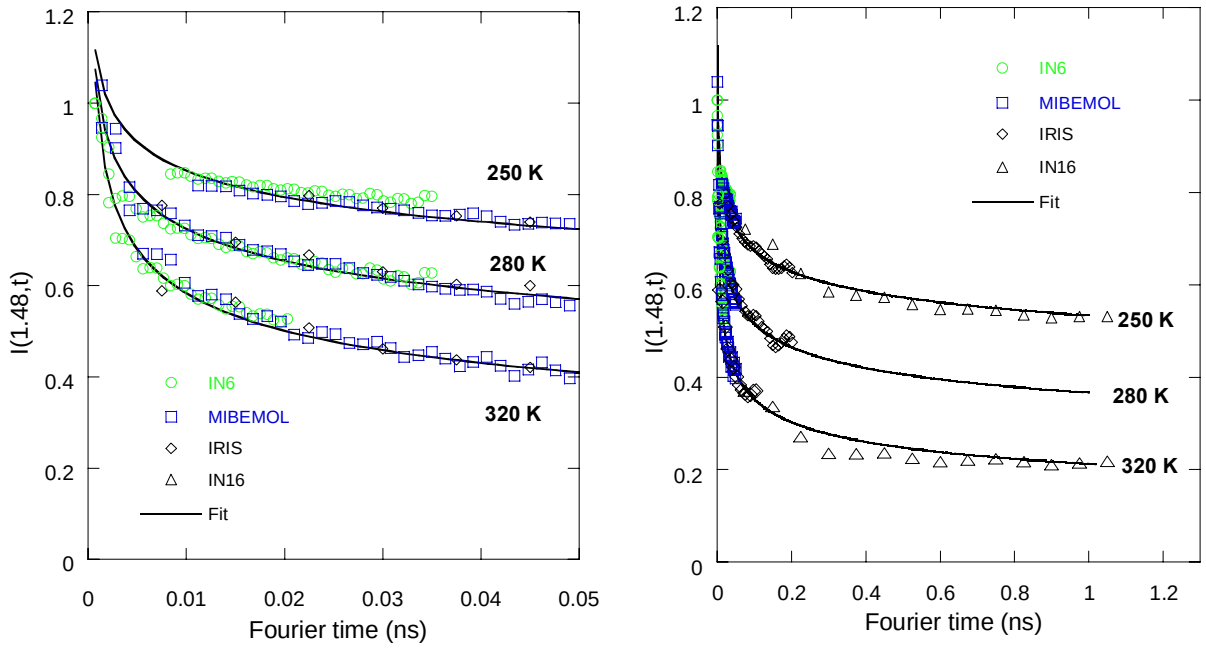

Fig. D.5.9 Intermediate scattering function for $PANI_{0.5}$DDoESSA at <Q> = 1.48 $Å^{-1}$ as deduced from measurements performed on four different spectrometers, shown in the short times range (left) and the whole time range (right).

Conclusion

We have shown that the dynamics in these "plastdoped" poly(aniline)s is characterized by a distribution of the relaxation rates over four orders of magnitude. Such a dynamical heterogeneity of these systems is not surprising considering they are constituted of short glass forming polymers. However, due to the special arrangement in which these short flexible chains are organized as bi-layers confined softly between rigid PANI stacks, these systems exhibit dynamics which is reminiscent of those of other complex systems. These systems are better described as networks of more or less inter-connected elementary units whose general dynamical behavior can be satisfactorily accounted for by using models based on a fractional calculus approach. At this point, it is however difficult to extract a clear microscopic physical picture of the system. Finally, it is still worth noting that in spite of a definite simplified character, the model we proposed for describing the geometry of the local diffusion of protons is still useful for the purpose of comparing all the systems of a same family. The study of these long plastdopants has however revealed the temporal complexity underlying their dynamics. Precisely for these systems, this understanding is additional crucial reason acting in

favor of a possible connection between the counter-ions dynamics and the electronic properties of the polymer [6].

D.6 Simulations

In this part, we are concerned with different aspects of protons dynamics in plast-doped polyaniline systems. Of course, it was impossible to do the elaborated simulations for every plast-dopants systems in the given available time, so we decided to choose the system with DB3EPSA doped polyaniline. Indeed, as it was described in chapter D.5 the whole family of plast-doped polyanilines exhibit similar dynamics and Pani/DB3EPSA represents well this dynamics. The availability of experimental data for Pani/DB3EPSA from the spectrometers with different energy/time resolutions was also important. The molecular dynamics simulations were performed to reproduce QENS spectra and to study in details molecular trajectories. In our QENS experiments we mainly see incoherent neutron scattering (due to scattering cross sections see chapter C.3.1) which contains information about local dynamics of individual particles. Since we were not interesting in any interference effects (as it was in MD simulation used in structural study chapter D.3) between particles we made experiments with different sizes of the periodic simulation box, and this way optimized the simulation real time.

D.6.1 Results obtained with "small" simulation box. Short time scale

The simulations performed with "small" periodic box were carried mainly to study dynamics of protons in Pani/DB3EPSA in relatively short time scale up to 20ps. This time range corresponds to time resolution available on IN6 spectrometer. The accurate computations require much longer simulation times than studied time range. So we decided to record the molecular dynamics trajectories of 250 ps length with 0.1 ps time step (see details in chapter C.4.5). The so called "small" simulation box contains four independent polyaniline chains with four aniline units connected with its mirrors across periodic boundaries into polymeric chains and eight DB3EPSA counter-ions. That was enough to have sufficient thermodynamic equilibrium during used simulation times. The use of smaller periodic boxes in our case leads to an artificial energy fluctuations upon molecular motion and overall motions can not be treated as a statistical average. Of course, by increasing the sizes of simulation box we improve the statistics, but the simulations become much more time consuming. That was quite important since we had to perform the simulations in range of temperatures using "slow" complex force field (See chapter C.4). The use of "small"

simulation box allows as performing complete studies in full range of temperatures used in experiments. The typical total energy profile during the simulation is presented in Fig.(D.6.1)

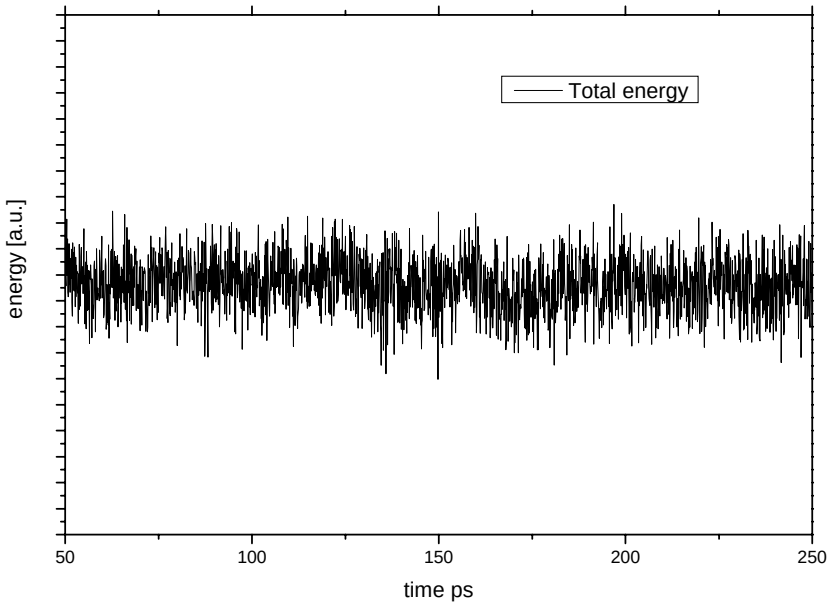

Fig. D.6.1 Typical profile of the total energy as a function of the simulation time.

EISF simulations in short time scale 0~20ps

Similar to classical analysis of neutron scattering data from QENS experiment we did first the EISF analysis. The EISF profiles as a function of momentum transfer Q were computed directly from molecular dynamics trajectories as it was described in chapter (C.4.5). The results of simulations of Elastic incoherent scattering function EISF as a function of temperature are presented in Fig.(D.6.2) as solid lines. In the same figure experimental results from IN6 and the fit to analytical model of local diffusion of protons in spheres is presented as points and dashed lines respectively. Complete discussion of the experimental results and the description of the diffusion in spheres model used for fitting are described in chapter D.5. Simulated EISF after necessary Debye-Waller corrections (see chapter C.4.5) are in good agreement with experimental results in the whole Q range and for all the temperatures. That would indicate the overall geometry of molecular motion in simulation is very similar to the geometry of motion observed on IN6 spectrometer time scale. That is an

important result, but such a global analysis even with perfect agreement can not give any additional proves for analytical model of local diffusion of protons in spheres applied in chapter D.5. However, since we have an access to the atomic trajectories of all the protons recorded from the MD simulations we can easily follow the individual protons or specific groups of protons motions. This type of analysis of atomic trajectories will be presented and discussed in next chapters.

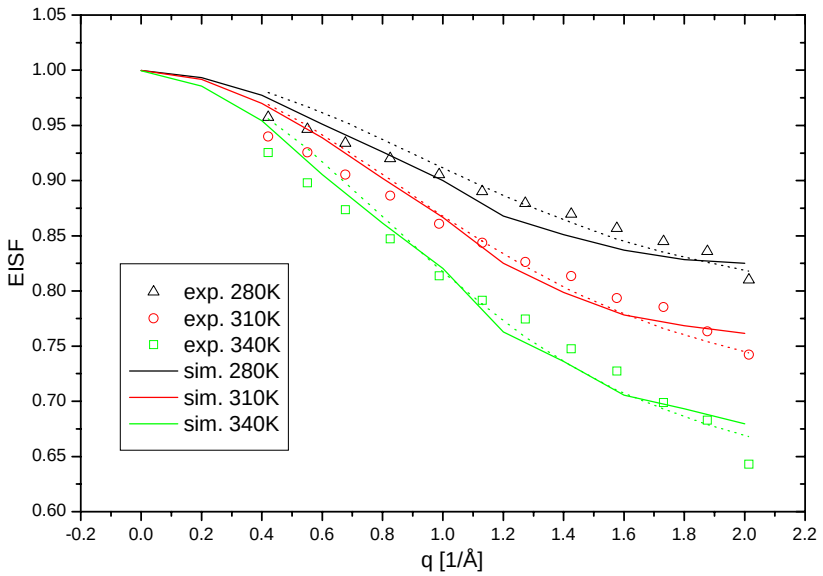

Fig D.6.2 EISF results. Dots: experimental, full lines: simulations and broken lines: analytical model of limited diffusion in spheres

Results of computation of Intermediate scattering function I(Q,t)

The intermediate scattering function I(Q,t) is also a very useful incoherent neutron scattering function. I(Q,t) which intrinsically contains more information than EISF. I(Q,t) is the relaxation function and contains the full information of the time scale and geometry of atomic motions. In fact, EISF is only a limit of I(q,t) when t goes to infinity (see chapter C.3). I(Q,t) may be directly computed from simulated molecular dynamics trajectories as it was shown in chapter C.4.5. But, unfortunately it is much more complicated to extract it from experimental results available from time-of-flight or backscattering spectrometers. An easier way is to follow opposite direction and compute dynamic structure factor S(Q,ω) from I(Q,t). For this reason we decided to compare the simulated S(Q,ω) with IN6 (short time scale) experimental data for the range of temperatures. The simulated intermediate scattering

function I(Q,t) as a function of the momentum transfer Q at 310K is presented in Fig.(D.6.3). The simulated I(Q,t) profiles exhibit very fast decay of the intensity at very short Fourier times due to vibrational contributions. Then much slower decrease of the intensity due to slower diffusive motion of protons. Because of the small number of long Fourier times available, and so imperfection in time-space average, the error of computation of I(Q,t) increase rapidly for longer Fourier times. We avoid this problem by using trajectory files much longer (~10 times) than used Fourier time range. The time range accessible from the IN6 spectrometer is indicated as a vertical line; only this part of I(Q,t) up to 20 ps was used for S(Q,ω) computation. The quality of I(Q,t) computation may be also improved by increasing the number of coordinates sets (bigger simulation box) used for space averaging, as it will be presented in next paragraphs dedicated to longer time scale I(Q,t) simulations.

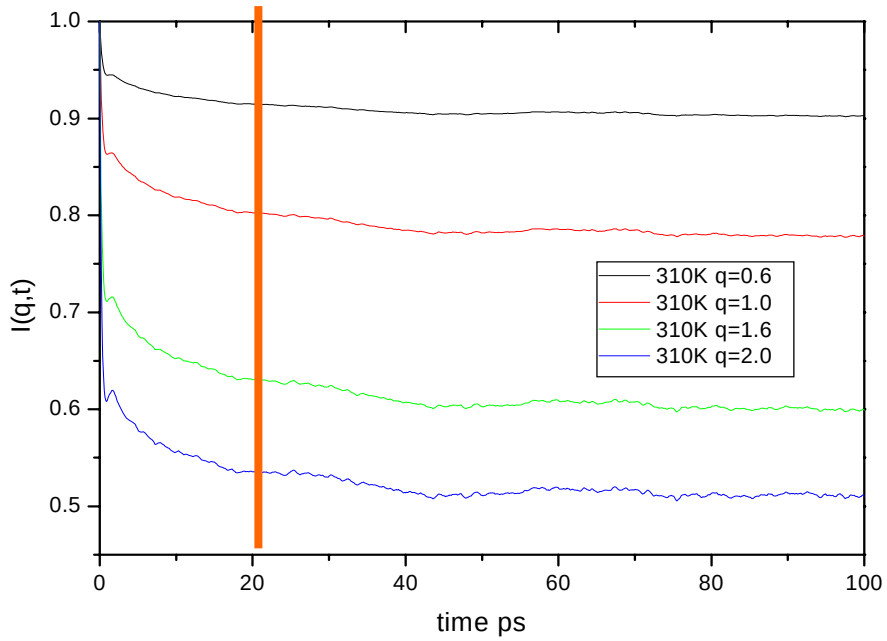

Fig. D.6.3 Simulated I(Q,t) as a function of momentum transfer Q. Vertical line represents the maximum time accessible on IN6 spectrometer.

Simulation of the dynamics structure factor S(q,ω)

The simulated Dynamics structure factor S(Q,ω) is strictly related to the experiments performed on IN6 spectrometer, since we used resolution function of IN6 spectrometer upon

the S(Q,ω) computation procedure described in C.4.5. The comparison of simulated S(Q,ω) with experimental results in whole range of simulated momentum transfer and temperature are presented in the Fig.(D.6.4). The resolution function and constant background extracted separately for each momentum transfer value from low temperature experimental data are shown as a grey area. The agreement of simulated S(q,ω) with experimental data is good especially for higher momentum transfers, however it should be note that the time scale probed in this analysis is not too broad only up to ~20 ps.

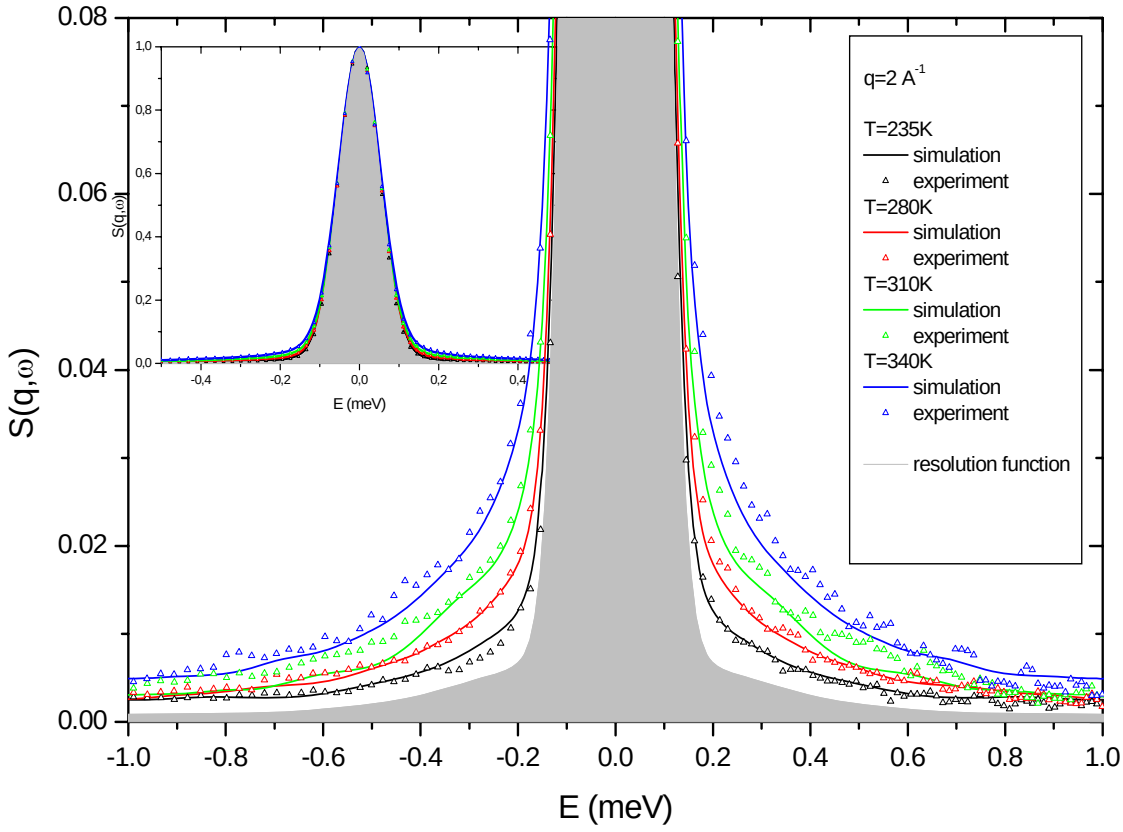

Fig. D.6.4 Comparison of simulated S(q,ω) with experimental results from IN6 spectrometer as a function of temperature. Whole shape of elastic peak is shown in insert.

D.6.2 Analysis of molecular dynamic trajectories. Local diffusion of protons and methyl group rotations

Mean square displacements. Simulations and the analytical model of local diffusion of protons.

Simulations have the advantage of allowing a systematic analysis of the mean square displacements of the different atoms constituting the system and thus of giving access to microscopic details which can not be revealed by a classical analytical treatment of the data. In figure D.6.5 the results of such an analysis concerning the trajectories of atoms lying on the flexible tails of counter-ions are shown. The results shown in figures D.6.5 and D.6.6 confirm the validity of the model of limited diffusion in spheres, previously proposed for interpreting EISF experimental results obtained on IN6 and presented in the previous chapter. The simulations give a similar distribution of displacements of atoms as a function of their position on the molecules. The characteristic lengths of these local diffusive motions also show good agreement between simulations and the analytical model.

The MD simulations confirm another important point. Since our study of PANI doped with camphor sulfonic acid [5], we have always assumed that in the picosecond time range, the PANI chains could be considered as immobile since their dynamics do not enter the experimental time window. This fact was proved experimentally by using partially deuterated PANI chains [5]. With plast-doped PANI's we could not check this point because partially deuterated PANI is not easily prepared. Here the simulations clearly validate this assumption, revealing that in this time range, the atoms belonging to PANI chains are indeed immobile. Similarly, the fact that the benzene ring at the head of the doping molecule is also immobile demonstrates the stiffness of the system in this particular region and thus the strength of the ionic interaction.

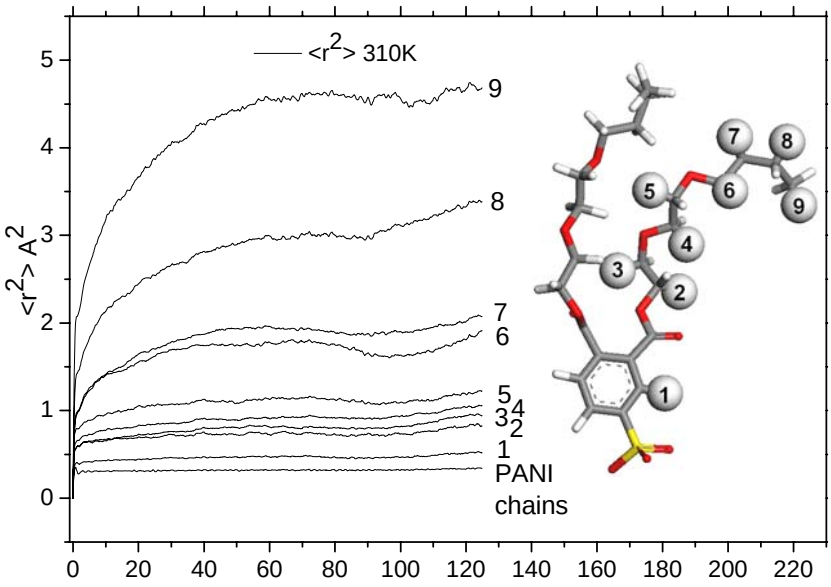

Fig. D.6.5 Mean square displacement of protons belonging to different equivalent sites in PANI chains and dopant counterions

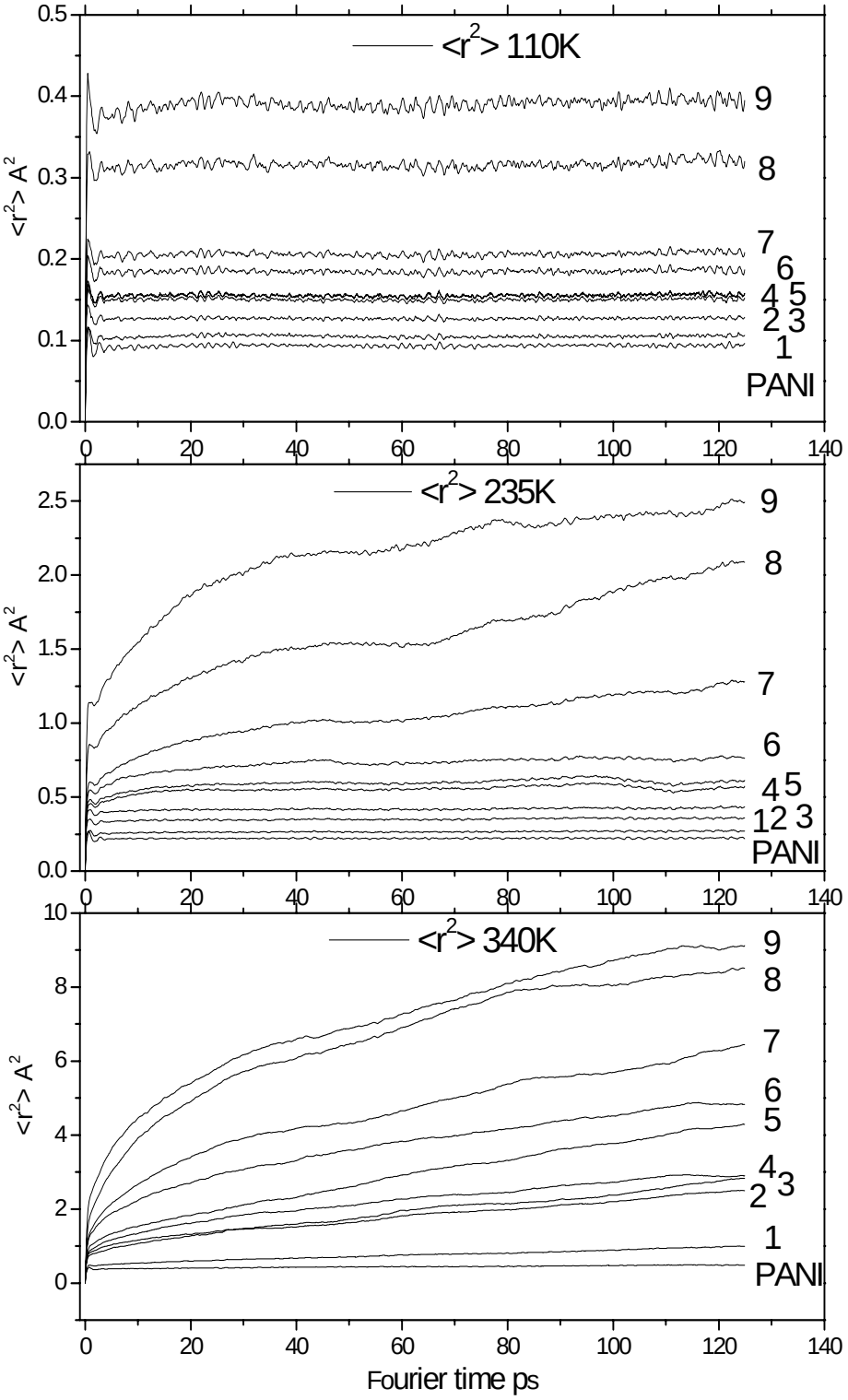

D.6.6 Mean square displacement of protons belonging to different equivalent sites in PANI chains and dopant counterions as simulated for four different temperatures. The crossover from below to above the dynamical transition around 200K is here clearly evidenced.

Methyl group rotation

The analysis of angular trajectories of methyl group's rotations around C-C bounds as illustrated on Fig.(D.6.7) reveal three equivalent jump sites separated by 120degrees. Angular trajectory of one methyl group with characteristic three site jumps separated by stochastic times is presented on Fig.(D.6.8).

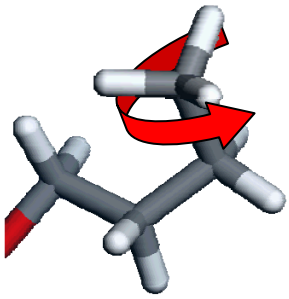

Fig. D.6.7 Methyl group rotation around C-C bound

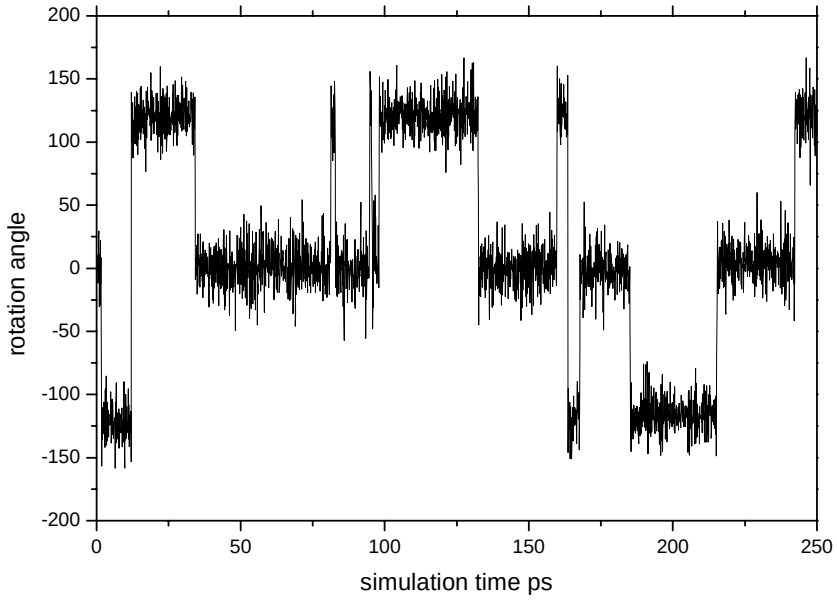

Fig. D.6.8 Angular trajectory of arbitrary chosen methyl group

The distribution of times between successive methyl group reorientations for all methyl groups in the simulation box is presented as a histogram in Fig.(D.6.9). To estimate the

average correlation time for all methyl group reorientations we applied the rotation rate distribution model (RRDM) which is based on log-Gaussian distribution of correlation time τ .

$$dP(\tau) = \frac{1}{\sqrt{2\pi\sigma^2}} \exp\left[\frac{1}{2\sigma^2} \ln^2\left(\frac{\tau_m}{\tau}\right)\right] \qquad \text{(D.6.1)}$$

Where τ_m is the most probable correlation time and σ^2 is the the variance of the distribution. This asymmetric distribution is a result of the exponential dependence of the correlation time on the activation energy (Arrhenius law) and the Gaussian energy barrier Fig.(D.6.10)[101]. The best $dP(\tau)$ fit at 310K is shown as a red line. In the fitting procedure we assumed that all the methyl groups are dynamically equivalent (with only one correlation time). That allowed us to estimate the correlation time for methyl group reorientation $\tau_m \approx 7\,ps$ which is comparable to typical experimental results obtained for the methyl groups containing systems [57].

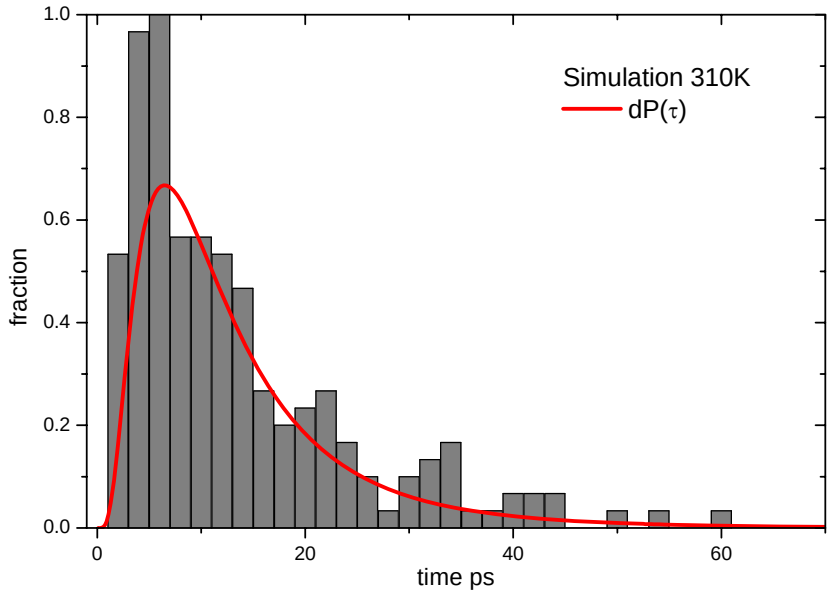

Fig.D.6.9 Distribution of times between successive methyl group 120 degree reorientation computed from angular trajectories of all CH_3 groups in the simulation box. Red line represents the log-Gaussian fit used for estimation of correlation time.

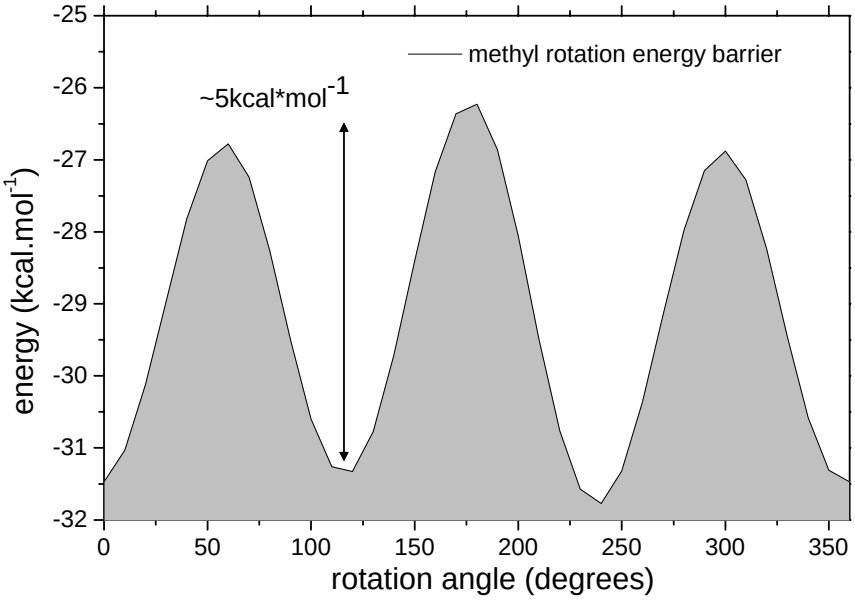

Fig. D.6.10 Methyl group rotation energy barrier

D.6.3 Vibrational density of states. (vDOS)

The simulated low energy vibrational densities of states vDOS were computed from MD trajectories using velocity autocorrelation function as described in chapter C.4.5. The simulated vDOS were compared with so called inelastic scattering function P(α,β) obtained in experiments carried out on IN6 spectrometer. These two functions vDOS and P(α,β) contain very similar information on vibrational modes in the system, however it should be note that they are not completely equivalent due to the following reasons:

1. The experimental intensities are not accurate, since P(α,β) must be extrapolate to α=0 to have real vDOS, see chapter C.4.5
2. The contribution due to multiphonon scattering is still present in P(α,β) function. It appears as a continuous background whose intensity increases as a function of the energy.
3. The experimental resolution of IN6 spectrometer and so the energy resolution of the experimental vDOS decrease rapidly for large energy transfers (*i.e.* from 80μeV at $\hbar\omega$=0meV to 2.5meV at $\hbar\omega$=12meV). In contrast, the energy resolution of simulated vDOS is constant ~2meV.

For the reasons described above, the comparison of experimental and simulated vDOS (inelastic scattering) is not as quantitative as it is in the case of quasi-elastic scattering. However, the qualitative studies of the simulated vibrational density of states allow separating various modes characteristic for vibrational motions of protons belonging to different molecules and intramolecular sites. In addition comparison with experimental data is a good way to check the validity of the force field used for atomic interactions.

The total vibrational density of states vDOS where all the protons in the simulated system were taken into account is compared with the experimental $P(\alpha,\beta)$ as obtained on IN6 in Fig.(D.6.11a). In addition simulated vDOS spectra have been computed for groups of protons belonging to different equivalent sites along dopant counterions tails and on polyaniline chains. The vibrational density of states of protons from methyl groups (CH_3), (CH_2) and polyaniline chains are collected in the figure (D.6.11b).

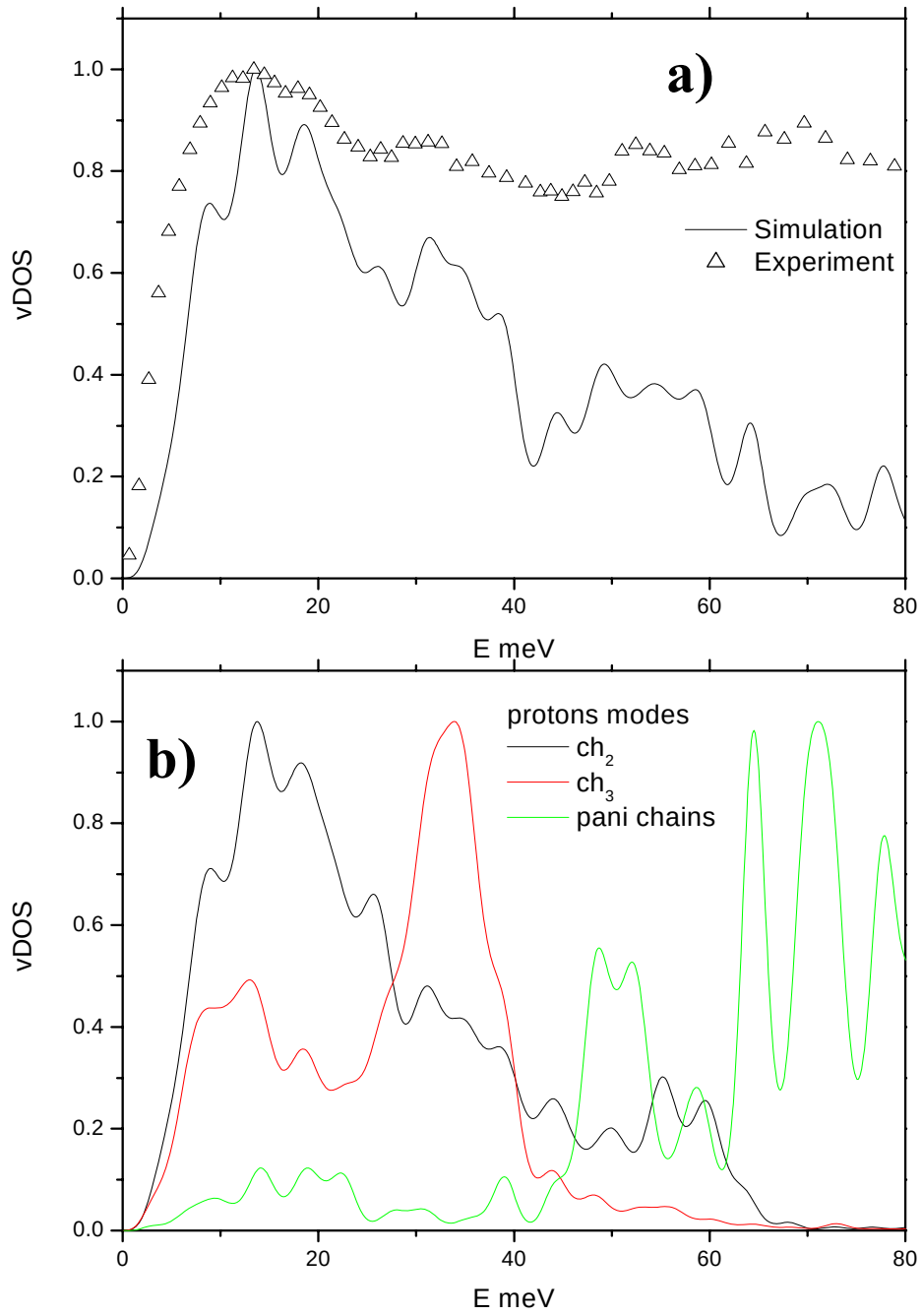

Fig. D.6.11 a) Total simulated and experimental (IN6) vibrational densities of states vDOS b) Simulated vDOS for selected groups of protons.

Counterion protons vibrations

First of all it must be note that almost 4/5 of protons in PANI/DB3EPSA system are born by DB3EPSA counterions. The majority of counterions protons belong to CH_2 groups along the alkoxy tails. Only six protons are situated on two CH_3 groups and three protons are

connected to benzene ring in each dopant molecule. For this reason vibrational modes of CH_2 groups protons are strongly dominating the total vDOS. CH_2 modes are broadly distributed over a 60meV energy interval what is characteristic of highly disordered systems (see Fig.(D.6.11a)). A closer inspection of vibrational modes of CH_2 groups shows slight shifts to lower energy of the most intense modes as a function of the position of CH_2 group along the dopant tails (see Fig.(D.6.12)). That would indicate the dominance of low energy (~15meV) modes (or coupling to more global motion of the chain) for groups closer to the end of the tails. Various possible vibrational motions of protons in CH_2 groups are shown in Fig. (D.6.11b). Low energy modes of CH_3 groups are dominated by the characteristic librational modes at ~30meV (Fig. (D.6.11b)). This is well known from literature [102]. The modes that correspond to methyl group torsions are also visible in experimental spectra, but this is not very well pronounced due to the small amount of methyl groups in the whole system (only ~10% of all protons). The other modes of methyl groups vibrations are centered at the very similar energies like the CH_2 group vibration modes with the maximum intensity at very low energy ~10-12meV.

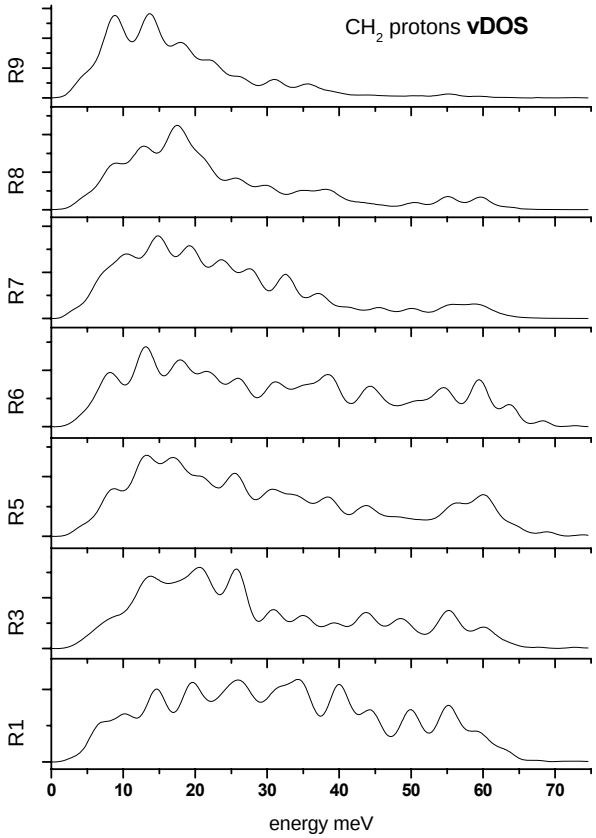

Fig. D.6.12 vDOS of CH_2 groups as a function of their position along the counterion tails (numbering from fig. D.6.5)

Polyaniline chain vibrations

The simulated polyaniline protons vibrational density of states is shown with a green solid line in Fig.(D.7.11b) and compared with the experimental results obtained for undoped polyaniline in EB form in Fig.(D.6.14). Higher energy vibrational modes centered around 50 meV and 67meV can be assigned to in-plane ring deformations and C-N-C bond deformations (in agreement with Raman data [103]). The vibrational modes centered in low energy range from ~7 to ~21 correspond to out-of-plane vibrations of phenyl rings of PANI chains [104] (see Fig.(D.6.13)). It can be note that intensities of out-of plane vibration modes are much smaller compare to in-plane vibrations. Such an effect may be associated with close packing of phenyl rings in stacks of polyaniline chains in simulated PANI/DB3EPSA structure. Out-of-plane vibrations are suppressed by phenyl ring overlapping.

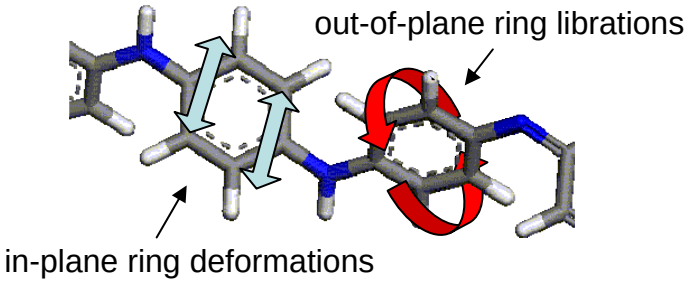

Fig. D.6.13 Illustration of PANI chain in-plane and out-of-plane vibrations

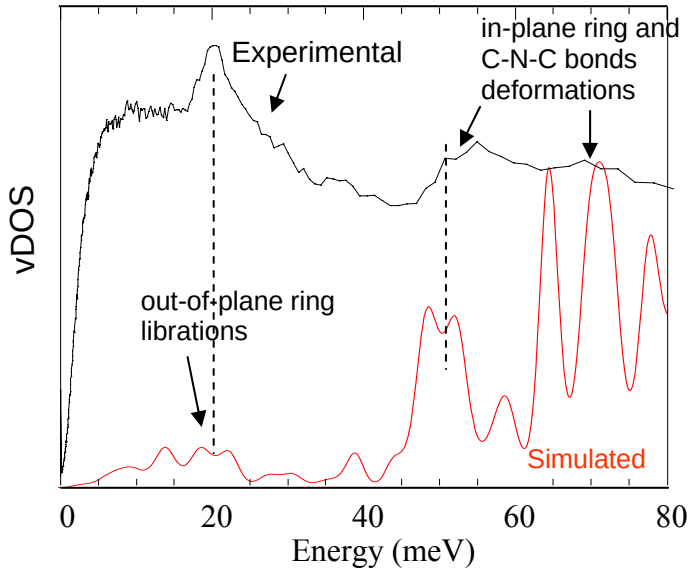

Fig. D.6.14 Comparison of experimental vDOS of undoped PANI (black line) with simulated for PANI chains.

D.6.4 Results obtained with "big" simulation box. Longer time scale

As it was already mentioned above we may improve the accuracy and statistics of computed intermediate scattering function I(q,t) by increasing the simulation time or the number of particles for space average by also increasing the simulation box size. The "small" simulation box contains only 8 independent counter-ions. Simulated I(q,t) profiles obtained with such a "small" periodic box are in good agreement (in shape) with experimental results, but only for short times range up to 50 ps (IN6 and MIBEMOL experiments time scale). For longer times we can see some artificial fluctuations due to poor statistics. For more accurate studies in long characteristic times comparable with the IRIS spectrometer time resolution ~200 ps we decided to perform the simulation using so called "big" simulation box. This simulation were much more time consuming, so we were restricted only to one simulation temperature ~300K. In addition some smooth simplifications of potential energy expression (force field) were done. (See chapter C.4.4 for all details)

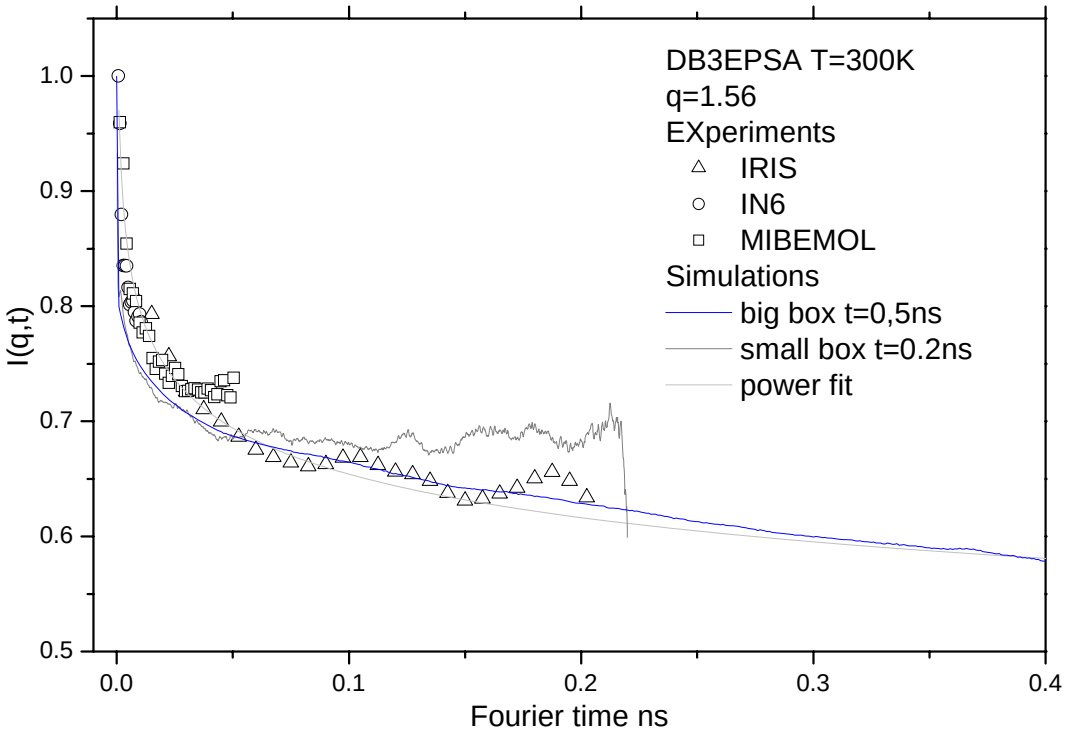

Fig. D.6.15 Comparison of experimental intermediate scattering functions and simulated curves obtained with "small" and "big" simulation boxes.

In Figure (D.6.15), the calculated and measured *I(Q,t)* are compared. The longer simulation allows *I(Q,t)* to be extended to 0.5 ns, that is half of the length of the MD simulation. *I(Q,t)* from the smaller, shorter MD run is calculated over the whole MD run and points in the second half of the time domain suffer from increasingly poor statistics. However, it can already be seen that around 100 ps, the bigger simulation gives significantly better agreement with the data and, therefore, a reliable description of the system out to longer Fourier times.

Mean square displacements of different atoms on the flexible tails were extracted in order to investigate the time distribution of the dynamics of the system. Considering all the atoms of the same counter-ion and calculating the average mean square displacement per counter-ion enabled the time-dependent behaviors among counter-ions to be compared. Figures (D.6.16) and (D.6.17) clearly reveal the distribution of average characteristic times of the overall dynamics of the counter-ions. It should be note that this inter-molecular time distribution was

not taken into account in the analytical model used in references [98] and [99]. Finally, as for the shorter simulations in the smaller box, the longer simulations confirm the way that intra-tail protons dynamics is distributed as it is shown by the Fig.(D.6.18).

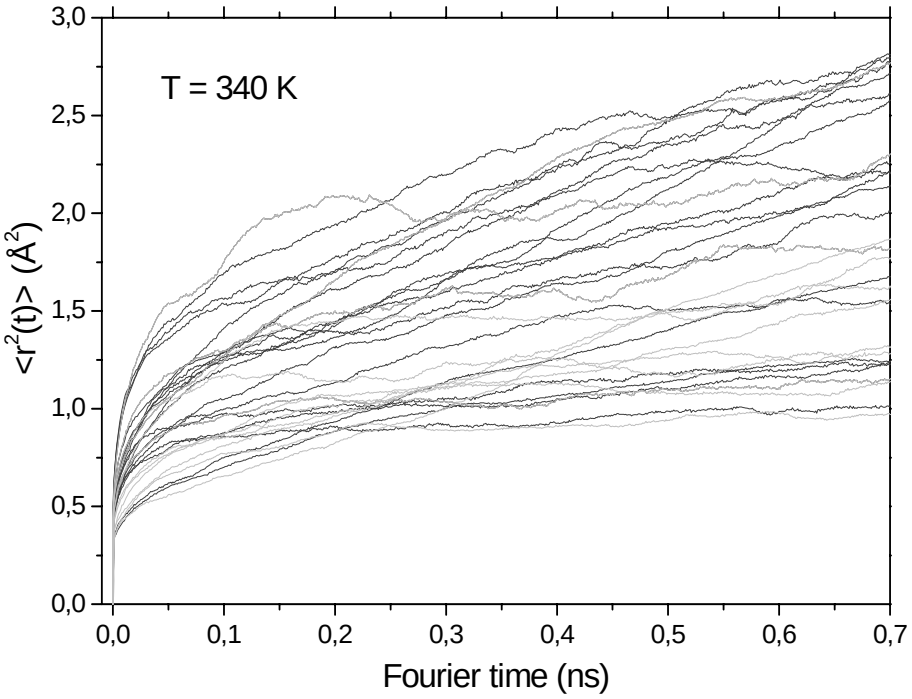

Fig. D.6.16 Mean values of the mean square displacements of all the atoms belonging to a same counter-ion and comparison between all the counter-ions.

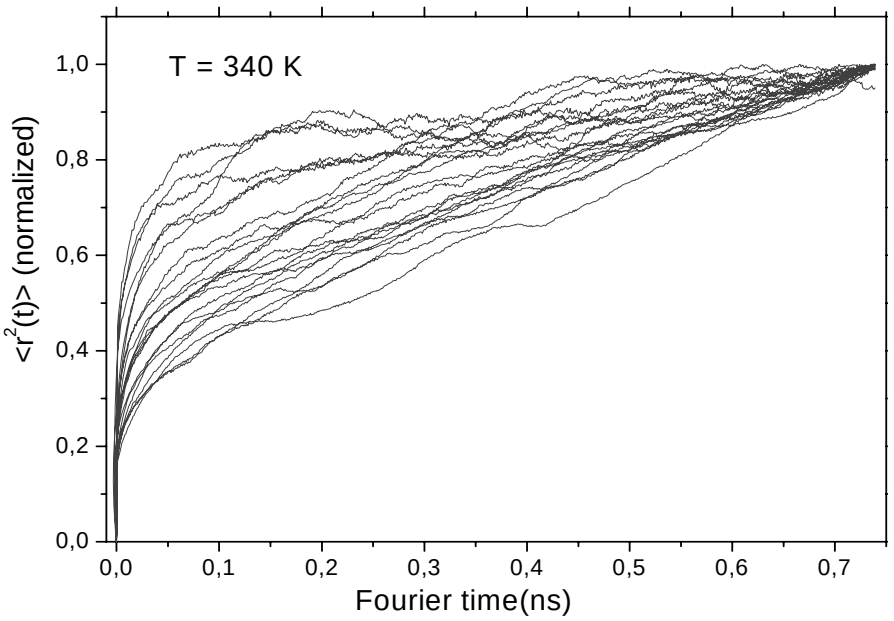

Fig. D.6.17 Mean square displacements for various counter-ions. The value for the longest time is normalized to one in order to make clear differences in relaxation times of different counter-ions.

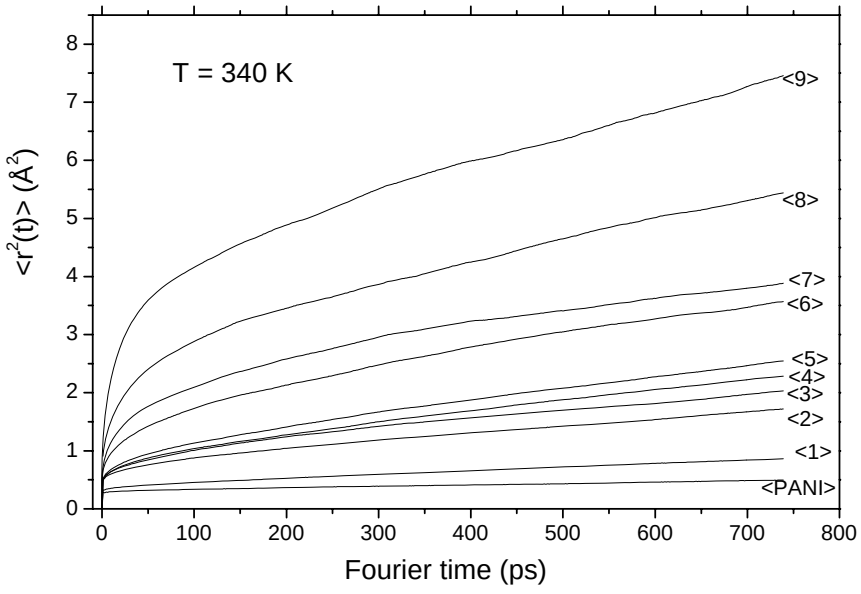

Fig. D.6.18 Average mean square displacements of protons lying on equivalent sites along counter-ions tails, counter-ions heads and pani chains.

Conclusions

We have used MD simulations to reproduce the structure and dynamics of highly conducting compound poly(aniline). A force field based MD approach, coupled with a careful treatment of partial charges, enables a realistic layered structure determined from X-ray diffraction measurements to be stabilized. The simulated dynamics give good agreement in the 10^{-12}-10^{-13}s time range by using only a small simulation box and a total simulation time of 250 ps. These simulations cover a wide temperature range and validate the analytical model of limited diffusion of protons, used to analyse the QENS data. Longer simulations in a bigger simulation box allow the agreement between simulated and experimental intermediate scattering functions to be improved over the longer time frame 10^{-10}- 10^{-13}s. The larger scale simulations clearly reveal the heterogeneity in the time evolution of the tail motion, whereas the analytical model included intra-molecular but not inter-molecular dynamical disorder.

The comparison of the simulated vibrational densities of states (vDOS) with experimental results justified the quality of the force field parameterization. In addition simulations of vDOS for polyaniline chains in the system reveal the influence of polyaniline phenyl ring stacking on suppressing of out of plan ring vibrations.

General conclusions, summary

This thesis is concerned with the structural and dynamics studies of new family of plast-doped conducting polyaniline compounds. The topic has been studied on the wide front, using classical techniques like: Wide angle and small angle X-ray scattering (WAXS) and (SAXS), Quasi-elastic neutron scattering (QENS) combined with molecular dynamics simulations (MD).

First part of this thesis is aimed at collecting and analyzing X-ray diffraction and Small Angle X-ray scattering data on series of the samples conducting films of polyaniline doped with various dicarboxylic acid diesters. The data have been analyzed in terms of crystallographic structure, degree of crystallinity, structural anisotropy of films, changing of texture under stretching. First inspection of WAXS data allowed us to propose the model of lamellar like supramolecular organization consisting of layers of stacked polyaniline chains separated by bi-layers of the dopant counter-ions with more or less inter-digitating tails. This model is valid for all the family of compounds. The validity of such a supramolecular organization has been justified by computer modeling of the structure by a lattice energy minimization. In addition computer modeling and molecular dynamics simulations bring out the crucial role of strong ionic interaction between charged polyaniline layers and dopant counter-ions for the stability of the lamellar supramolecular structure.

An introduction of a model for the statistical fluctuation in the multilamellar like structure based on a classical scattering formula with the paracrystalline structure factor and the form factor computed from electronic density distribution determined from molecular dynamic simulations was essential for estimation of the structural parameters characterizing the distorted lamellar stacking in the system like: the numbers of coherently scattered layers, lamellar repeat distances and others. It was shown that applying of molecular dynamics simulations may be useful for the construction of physically realistic models.

The comparison of X-ray scattering patterns of obtained in transmission and reflection geometry gave interesting information of self-assembling of the free standing thin films. The in-plane out-of plane anisotropy of the film was explained by the preference of the crystallites to be oriented with respect to the film surface. The influence of the length of dopant tails on such a self-assembling was also discussed.

Another important point was to study of the evolution of structural anisotropy in the polyaniline films upon stretching. The careful inspection of the structural parameter evolution

like: lamellar stacking distances and mechanisms of crystallites reorientation upon stretching allow as proving the paracrystalline character of lamellar stacking in the system and associate it with the softness of counterions medium.

The last part of the thesis was dedicated to the studies of the dynamics in plast-doped polyaniline systems. First, the "classical" analyses of quasi-elastic neutron scattering (QENS) data were performed. The proposed models of the dynamics and experimental scattering functions were examined and compared with results obtained from molecular dynamics simulations (MD).

The elastic neutron scattering in so-called fixed energy window experiments performed both and first and second generation plast-doped polyaniline system evidenced the same, previously reported for PANI/CSA system, correlation between dynamic transition and the electrical metal-insulator transition. These results motivated us to do the systematic studies of quasi-elastic neutron scattering in various temperatures. The QENS experiments were carried out using several spectrometers with different energy resolutions to study the dynamics of molecular motion in a broad range of time scales.

The detailed analysis of elastic incoherent structure factor EISF which gives the overall view of the geometry of molecular motion at a given time scale of the spectrometer, allow us proposing the analytical model of local diffusion of protons in spheres. The parameters of models used for fitting the theoretical EISF to experimental results give the important information of the range of motion of the hydrogen atoms belonging to the different sites of the counter-ions tails.

The comparison of the experimental EISF obtained using spectrometers with different energy resolution led us to the assumption that the hydrogen atoms of counter-ions are experiencing motions with similar geometry but at very different time scales. The analysis of intermediate scattering function I(Q,t) gave more contrasted view of the dynamics as a function of the time. Connection of I(Q,t) profiles extracted from different spectrometers shows the dynamics characteristic for the complex systems. Such a shape relaxation function can be rendered to the model motions of the flexible counter-ions chains confined between rigid PANI stacks.

The molecular dynamics simulations (MD) are complementary tool for incoherent QENS experiments, since they probe the same time scale. The sets of MD simulations in all experimental temperatures were performed for PANI/DB3EPSA system. First of all, MD simulations justified proposed supra-molecular structures and reveal the role of PANI - counterion head group ionic interaction for its stability. The computations of elastic

incoherent structure factor EISF and Dynamics Structure factor S(Q,ω) from molecular dynamics trajectories are in good agreement with the experimental ones. Detailed analysis of molecular dynamic trajectories give additional proves for proposed analytical models of local dynamics of protons.

General conclusion

It was shown that combination of the structural and dynamics studies with molecular dynamics MD simulations is a good way to obtain the overall view conducting polyaniline based compounds including an information about the characteristic times and geometry of molecular motions in the system, and degree of static and dynamic disorder. With this information it can be interesting to try to connect these results with other contributions, to develop theoretical models for charge transport in polymers explaining better the electronic properties of these systems. From this point of view, this work may be treated as a good starting point for further studies of electrical conductivity in polymers and finally give a rise of understanding electronic transport in conducting polymers.

List of figures

Fig. D.6.11 a) Total simulated and experimental (IN6) vibrational densities of states vDOS
b) Simulated vDOS for selected groups of protons.

Fig. D.6.12 vDOS of CH_2 groups as a function of their position along the counterion tails (numbering from fig. D.6.5)

Fig. D.6.13 Illustration of PANI chain in-plane and out-of-plane vibrations

Fig. D.6.14 Comparison of experimental vDOS of undoped PANI (black line) with simulated for PANI chains.

Fig.D.6.15 Comparison of experimental intermediate scattering functions and simulated curves obtained with “small” and “big” simulation boxes

Fig. D.6.16 Mean values of the mean square displacements of all the atoms belonging to a same counter-ion and comparison between all the counter-ions.

Fig. D.6.17 Mean square displacements for various counter-ions. The value for the longest time is normalized to one in order to make clear differences in relaxation times of different counter-ions.

Fig. D.6.18 Average mean square displacements of protons lying on equivalent sites along counter-ions tails, counter-ions heads and pani chains.

List of publications

1. *Force Field based Molecular Dynamics Simulations in Highly Conducting Compounds of Poly(aniline). A comparison with quasi-elastic neutron scattering study.*//Chem.Phys. In press*,* M. SNIECHOWSKI, D. DJURADO, M. BÉE, M.K. JOHNSON, M.A. GONZALEZ, P. RANNOU, B. DUFOUR, W. LUZNY

2. *Counter-ions dynamics in highly plastic and conducting compounds of poly(aniline). A quasi-elastic neutron scattering study*,//Phys,Chem.Chem.Phys. 7:1039 2005 D.DJURADO, M. BÉE, M. SNIECHOWSKI, S. HOWELLS, P. RANNOU, A. PRON , J.P. TRAVERS AND W. LUZNY

3. *Structure and dynamics of plast-doped conducting polyaniline compounds,* // Fibres \& Textiles in Eastern Europe. In press, M. ŚNIECHOWSKI, W. ŁUŻNY, D. DJURADO, B. DUFOUR, P. RANNOU, A. PROŃ, M. BEE, M. JOHNSON AND M. GONZALES

4. *Direct analysis of lamellar structure in polyaniline protonated with plasticizing dopants,*// Synthetic Metals. *143:355 2004*, M. SNIECHOWSKI , D. DJURADO , B. DUFOUR , P. RANNOU , A. PRON AND W. LUZNY

5. *Structural properties of emeraldine base and the role of water contents: X-ray diffraction and computer modelling study* / W. ŁUŻNY, M. ŚNIECHOWSKI, J. LASKA // Synthetic Metals. --- 2002 vol. 126 s. 27--35. --- Bibliogr. s. 35

6. *The role of water content for the emeraldine base structure* / Wojciech ŁUŻNY, Maciej ŚNIECHOWSKI // Fibres \& Textiles in Eastern Europe. --- 2003 vol. 11 no. 5 s. 75--79. --- Bibliogr. s. 79, Abstr.

Conferences

1. *Molecular dynamics in metallic and highly plastic compounds of polyaniline. A study using quasi-elastic neutron scattering measurements and molecular dynamics simulations* M. SNIECHOWSKI, D. DJURADO, M. BÉE, M.K. JOHNSON, M.A. GONZALEZ, P. RANNOU, B. DUFOUR, Adam PRON, Jean Pierre TTRAVERS, Neutrons and Numerical methods 2, M2M2 14-18 September 2004, Institut Laue-Langevin, Grenoble, France

2. *Counter-ions dynamics in highly plastic and conducting compounds of polyaniline. A quasi-elastic neutron scattering study*. D. DJURADO, M. BÉE, M. SNIECHOWSKI, S. HOWELLS, P. RANNOU, A. PRON, J.P. TRAWERS, The 7th International conference on Quasi-Elastic Neutron Scattering QENS04, 1-4 September 2004, Arcachon, France

3. *Analyse de la structure lamellaire desordonee de composes conducteurs 'plastdopes' de la polyaniline* /M. SNIECHOWSKI, D.DJURADO, B. DUFOR , P.RANNOU, A. PRON and W. LUZNY JPC03 10emes Journees polymeres conducteurs. 15-19 septembre 2003 Durdan France

4. *XRD and SAXS study of the structural properties of plast-doped conducting polyaniline compounds* / M. ŚNIECHOWSKI, D. Djurado [et al.], W. ŁUŻNY // W: XLV [Czterdzieste piąte] Konserwatorium Krystalograficzne = 45th Polish Crystallographic Meeting : Wrocław, 26--27 czerwca 2003. --- [S. l. : s. n., 2003]. --- S. 213. --- Bibliogr. s. 213

5. *Struktura nadcząsteczkowa i właściwości elektryczne polianiliny plastyfikowanej diestrami kwasu fosforowego* --- [Ultramolecular structure and electrical properties of polyaniline plasticized with phosphoric acid diesters] / M. ŚNIECHOWSKI, W. ŁUŻNY, J. LASKA // W: Kryształy molekularne 2002 : ogólnopolska konferencja : Konstancin--Jeziorna 17--21 września 2002. --- [Warszawa : Instytut Fizyki Polskiej Akademii Nauk, 2002]. --- S. 194--195. --- Bibliogr. s. 195, Abstr.

6. *Role of water contents for the structural properties of polyaniline* / M. ŚNIECHOWSKI, W. ŁUŻNY // W: XIPS'2001 : the fifth international conference on X-Ray Investigations of Polymer Structure : the satellite conference of the 20-th European Crystallographic Meeting : 5--8 December 2001 Bielsko-Biała : programme. --- [S. l. : s. n., 2001]. --- S. P 22

7. *Role of water contents for the structural properties of polyaniline* / M. ŚNIECHOWSKI, W. ŁUŻNY // W: TME'01 : Towards Molecular Electronics : 25--30 June 2001 Śrem (Poland) : international conference : abstracts / A. Mickiewicz University at Poznań. Faculty of Chemistry. Organic Semiconductor Laboratory. --- [Poznań : A. Mickiewicz University, 2001]. --- S. P6

8. *Effect of preparation conditions on the structural properties of emeraldine base* / J. LASKA, W. ŁUŻNY, J. WIDLARZ, M. ŚNIECHOWSKI // W: World polymer congress : IUPAC MACRO 2000 : 38th Macromolecular IUPAC symposium : Warsaw 9--14 July 2000 : book of abstracts. Vol. 2. --- [Warsaw : Warsaw University of Technology, 2000]. --- S. 866. --- Bibliogr. s. 866

References:

[1] For a review see for example Materials Today Sept. 2004, pp 21-45.

[2] A.J.Heeger, S. Kivelson, J.R. Schrieffer, W.P. Su, Rev. Mod. Phys. 60(1988)781.

[3] R.S. Kohlman, A. Zibold, D.B. Tanner, G.G. Ihas, T. Ishiguro, Y.G. Min, A.G. Mac Diarmid, A.J.Epstein, Phys. Rev. Letters 78(1997)3915.

[4] P.E. Parris, V.M. Kenkre, D.H. Dunlap, Phys. Rev Letters 87(2001)126601.

[5] D. Djurado, J. Combet, M. Bée, P. Rannou, B. Dufour, A. Pron, J. P. Travers, Phys. Rev. B. 65(2002)184202.

[6] D. Djurado, M. Bée, J. Combet, B. Dufour, P. Rannou, A. Pron, J.P. Travers, ILL Annual Report 2000 -(2001) - Scientific Highlights pp 62 -63.

[7] Nobel Lectures *Review of Modern Physics*, **73** (2001) 681 –718

[8] M.D. McGhee, E.K. Miller, D. Moses and A.J. Heeger in *"Advances in Synthetic metals, Twenty Years of Progress in Science and Technology"*, edited by P. Bernier, S. Lefrant and G. Bidan, Elsevier Science, 1999, pp 98 – 205.

[9] L.E.Alexander, X-Ray Diffraction Methods in Polymer Science, Wiley-Interscience, New York 1969.

[10] For comprehensive reviews see *The Handbook of Conducting Polymers, 2nd Ed*, T.A. Skotheim, R.L. Elsenbaumer and J.R. Reynolds, eds., (Mercel-Dekker, New York, Basel, Hong Kong, 1997).

[11] W.R. Salaneck, D. T. Clark, and E.J. Samuelsen (eds.) Science and Applications of Conducting Polymers, Adam Hilger, Bristol, 1991.

[12] E. M. Genies, A. Boyle, M. Lapkowski, C. Tsintavis, Synth. Met. 36(1990)139.

[13] T. Yamamoto, K. Sanechika, Chem. Ind. 1(1982)301.

[14] D. Djurado, J.Ma, N. Theophilou, J.E. Fischer, Synth. Met. 30(1989)395.

[15] A. J. Heeger, J. R. Schrieffer, W.-P. Su, Rev. Mod. Phys. 40(1988)3439.

[16] G. Leising, O. Leitner, H. Kahlert, Mol. Cryst. Lig. Cryst. 117 (1985)67.

[17] Y. B. Moon, M. J. Winokur, A. J. Heeger, J. Barker, D. C. Bott, Macromolecules 20 (1987)2457

[18] D. Begin, F. Saldi, M. LeLaurain, D. Billaud, Solid State Commun. 76(1990)591..

[19] R. H. Baughman, S. L. Hsu, G. P. Pez, A. J. Signorelli, J. Chem. Phys. 68(1978).5405.

[20] D. Chen, M. J. Winokur, M. A. Masse, F. E. Karasz, Polymer 33(1992)3116.

[21] J. P. Pouget, M. E. Jozefowicz, A. J. Epstein, X. Tang, A. G. MacDiarmid, Macromolecules 24(1991)779.

[22] J. P. Pouget, M. E. Jozefowicz, A. J. Epstein, J. G. Masters, A. Ray, A. G. MacDiarmid, Macromolecules 24(1991)5863.

[23] J. E. Fischer, X. Tang, E. M. Scherr, V. B. Cajipe, A. G. MacDiarmid, Macromolecules 27(1994)5094.

[24] W. Łużny, M. Śniechowski, J. Laska, Synth. Met. 126(2002)27.

[25] L. W. Shacklette and J. E. Toth, Phys. Rev. B 32(1985)5892.

[26] F. Saldi, J. Ghanbaja, D. Begin, M. LeLaurain, D. Billaud, C.R. Acad. Sci. 309(1989)671.

[27] D. Djurado, J. E. Fischer, P. A. Heiney, J. Ma, Phys. Rev. B 41(1990)2971.

[28] D. Djurado, J. E. Fischer, P. A. Heiney, J. Ma, N. Coustel, P. Bernier, Synth. Met. 34 (1990)683.

[29] N. S. Murthy, L. W. Shacklette, R. H. Baughman, Phys. Rev. B 40(1989)12550.

[30] M. J. Winokur, Y. B. Moon, A. J. Heeger, J. Barker, D. C., Bott, H. Shirakawa, Phys. Rev. Lett. 35(1987)2329.

[31] R. H. Baughman, N. S. Murthy, G. G. Miller, L. W. Shacklette, J. Chem. Phys. 79 (1983)1065.

[32] N. S. Murthy, G. G. Miller, R. H. Baughman, J. Chem. Phys. 89(1988)2523.

[33] M. J. Winokur, J. Maron, Y. Cao, A. J. Heeger, Phys. Rev. B 45(1992)9656.

[34] A. Biswas, K. Deutscher, J. Blackwell, G. Wegner, Proc. Am. Chem. Soc., Polym. Preprints 33(1)(1992)286.

[35] T. J. Prosa, M. J. Winokur, J. Moulton, P. Smith, A. J. Heeger, Macromolecules 25(1992)4364.

[36] Y. Cao, P. Smith, A. J. Heeger, Synth. Met. 48(1992)91.

[37] M.J. Winokur, Hailan Guo and R.B.Kaner Synth.Met 119 (2001) 403-404

[38] *Sigmar Roth, David Carroll, One-Dimensional metals Wiley-VCH Verlag GmbH& Co.KGaA 2004*

[39] J. Tsakumoto, A. Takahashi, K. Kawasaki, Jpn. J. App. Phys.29(1990)125.

[40] H. Naarmann, N. Theophilou, Synt. Met. 22 (1987)1.

[41] H. Shirakawa, Y.-X. Zhang, T.Okuda, K. Sakamaki, and K. Akagi, Synth. Met. 65(1994)93.

[42] J.-C. Chiang, A.G MacDiarmid, Synth. Met. 13(1983)193.

[43] A.J. Epstein, H. Rommelmann, R. Bieglow, H.W. Gibson, D.M. Hoffman, D.B. Tanner, Phys. Rev. Lett. 50(1983)1866.

[44] A.J. Epstein, H. Rommelmann,, M. Abakowitz, H.W. Gibson, Phys. Rev. Lett. 47(1981)1549.

[45] A.J. Epstein, H. Rommelmann,, H.W. Gibson, Phys. Rev. B . 31(1985)2502.

[46] V.N. Prigodin, A.J. Epstein, Synth. Met. 125(2002)43.

[47] V.N. Prigodin, A.J. Epstein, Physica B 338(2003) 310.

[48] A. G. MacDiarmid, Angew. Chem. Int. Ed., 40(2001)2581.

[49] A. Proń, P. Rannou, Prog. Polym. Sci. 27(2002)135.

[50] P. N. Adams, P. Devasagayam, S. J. Pomfret, L. Abell, A. Monkman, J. Phys. Condens. Matter 10(1998)8293.

[51] R.K.Paul, C.K.S.Pillai, Synth.Met. 114(2000)27.

[52] H.S.O.Chan, S.C. Nag, P.K. Ho, Macromolecules 27(1994)2159.

[53] J. Laska , A. Pron, S. Lefrant, J. of Polym. Science, Part A, .Polym. Chem. 33(1995)1437.

[54] B. Dufour, P. Rannou, D. Djurado, H. Janeczek, M. Zagorska, A. de Geyer, J.P. Travers, A. Pron, Chem. Mater. 15(2003)1587.

[55] Olinga T., Fraisse J., Dufresne A., Travers J.P., Pron A., Macromolecules 33(2000)2107.

[56] All information can be found on http://www.esrf.fr.

[57] P. A. Egelstaff, *Thermal Neutron Scattering* (Academic, New York, 1971).

[58] S. W. Lovesey, *Theory of Neutron Scattering from Condensed Matter* (Clarendon Press, Oxford, 1984)

[59] G. L. Squires, *Introduction to the Theory of Thermal Neutron Scattering* (Cambridge University Press, Cambridge, 1978)

[60] G. Kostorz, *Neutron Scattering in Material Science* (Academic, New York, 1978)

[61] T. Springer, *Quasielastic Neutron Scattering for the Investigation of Diffusive Motions in Solids and Liquids; SpringerTracts in Modern Physics* (Springer, Berlin 1972)

[62] M. Bée, *Quasielastic Neutron Scattering: Principles and Applications in Solid State Chemistry, Biology and Materials Science* (Adam & Hilger, Bristol, 1988)

[63] All information can be found on http://www.ill.fr

[64] W.S. Howells, M.T.F. Telling, Guide-IRIS Data Analysis (Rutherford Appleton Laboratory, UK (2000)) pp72-77.

[65] Cerius Doc. http://www.accelrys.com

[66] H.J.C. Berendsen, J.P.M. Postma, W.F. van Gunsteren, A. DiNola, J.R. Haak, J. Chem. Phys. 81(1984)3684.

[67] H. Sun, J. Phys. Chem. 102(1998)7338.

[68] http://www.ch.embnet.org/MD_tutorial

[69] A.K. Rappé, W.A. Goddard, J. Phys. Chem. 95(1995)3358.

[70] G.R. Kneller, V. Keiner, M. Kneller, M. Schiller, Comp. Phys. Comm. 9(1995)191.

[71] M.E. Josefowicz, R. Laversanne, H.S. Javadi, A. Epstein, J.P. Pouget, X. Tang, A.G. MacDiarmid, Phys. Rev. B 39 (1989) 12958

[72] W. Luzny, E.J. Samuelsen, D. Djurado, Y.F. Nicolau, Synth. Met. 90 (1997) 19

[73] W. Wernet, M. Monkenbusch, G. Wegner, Makromol. Chem. Rapid Commun. 5 (1984) 157.

[74] K. Levon, K.H. Ho, W.Y. Zheng, J. Laakso, T. Karna, T. Taka, J.E. Österholm, Polymer 36 (1995) 2733

[75] O. Ikkala, M. Knaapila, J. Ruokolainen, M. Torkkeli, R. Serima, K. Jokela, L. Horsburgh, A. Monkman, G. ten Brinke, Adv. Mater. 11 (1999) 1206

[76] O. Ikkala, J. Ruokolainen, G. ten Brinke, M. Torkkeli, R. Serima, Macromolecules 28 (1995) 7088

[77] W.Y. Zheng, R.H. Wang, K. Levon, Z.Y. Rong, T. Taka,, W. Pan, Macromol. Chem. Phys. 196 (1995) 2443

[78] R. Stepanyan, A. Subbttin, M. Knaapila, O. Ikkala, G. ten Brinke, Macromolecules 36 (2003)3758.

[79] B. Grévin, P. Rannou, R. Payerne, A. Pron, J.P. Travers, Adv. Materials, 15 (2003) 881.

[80] B. Grévin, P. Rannou, R. Payerne, A. Pron, J.P. Travers, J. Chem. Phys. 118 (2003)

[81] R. Hosemann, S.N Bagchi, *Direct analysis of Diffraction by Matter*, North-Holland, Amsterdam (1962).

[82] R. Zhang, R.M. Suter, J.F. Nagle, Phys. Rev. E 50(1994)5047.

[83] A. Guinier, *X-Ray Diffraction*, Freeman and Co., San Francisco (1963)

[84] A. Caillé, C.R. séances Acad. Sci. Ser. B 274(1972)891.

[85] Y. Lyatskaya, Y. Liu, S. Tristram-Nagle, J. Katsaras, J.F. Nagle, Phys. Rev. E 63(2000)011907.

[86] G. Pabst, M. Rappolt, H. Amenitsch, P. Laggner, Phys. Rev. E 62(2000)4000.

[87] D.W. Breiby, PhD Thesis, Norges Teknisk Naturvitenskapelige Universitet Trondheim (Norway) (December 2002 – number 145)

[88] X.-Q Mu, Acta Cryst. Sect. A, 54(1998)606.

[89] B. Frick, A. Magerl, Y. Blanc, R. Rebesco, Physica B 234-236(1990)1177.

[90] M. Bée, D. Djurado, J. Combet, M.A. Gonzalez, P. Rannou, B. Dufour, D. Marque, Applied Physics A.74[Suppl.](2002) S402.

[91] A.M. Giroud-Godquin, P. Maldivi, J.C. Marchon, M. Bée, L. Carpentier, Mol. Phys. 68(1989)1353.

[92] L. Carpentier, M. Bée, A.M. Giroud-Godquin, P. Maldivi, J.C. Marchon, Mol. Phys. 68(1989)1367.

[93] F. Volino, A.J. Dianoux, Mol. Phys. 41(1980)271.

[94] J. Colmenero, A. Arbe, F. Alvarez, A. Narros, D. Richter, M. Monkenbusch, B. Farago, Pramana J. Phys. 63(2004)25.

[95] J.B. Bates, Y.T. Chu, Solid State Ionics 28-30(1988)1388.

[96] H. Scher, E.W. Montroll, Phys. Rev.B 12(1975)2455.

[97] E. Kjartansson, J. Geophys. Res. 84(1979)4737.

[98] H. Schiessel, C. Friedich, A. Blumen, *Applications of fractional calculus in physics*, World Scientific 2000, chap. VII, pp 331.

[99] H. Schiessel, A. Blumen, Macromolecules, 28(1995)4013.

[100] G.R. Kneller, K. Hinsen, J. Chem. Phys.121(2004)10278.

[101] A.Chaid, A.Alegria, and J.Colmenero. Macromolecules, 27(1994)3282.

[102] Nhan Duc Morelon, PhD Thesis, Université Joseph Fourier, 19 janvier 1999, Grenoble France.

[103] I. Harada, Y. Furakawa, F.Ueda, Synth.Met. 29(1989)303.

[104] J.L. Sauvajol, D.Djurado, A.J. Dianoux, J.E. Fischer, E.M. Scherr, A.G. MacDiarmid, Phys. Rev. B 47(1993)4959.